Decimetric-resolution elastic characterisation of the shallow subseabed using pre-stack waveform inversion

Giuseppe Provenzano

School of Ocean and Earth Science

University of Southampton

A thesis submitted for the degree of

Doctor of Philosophy

February 2018

To my beloved grandfathers
Pino and Giorgio.

University of Southampton

Abstract

Faculty of Engineering, Science and Mathematics
School of Ocean and Earth Science

Doctor of Philosophy

Decimetric-resolution elastic characterisation of the shallow subseabed using pre-stack waveform inversion

by Giuseppe Provenzano

Currently, engineering-scale shallow sediment characterisation relies heavily on core analysis and cone-penetrometer tests. Unlike reservoir-scale exploration, little quantitative information is derived from seismic reflection data, leaving largely unexploited their intrinsic value as a remote characterisation tool. In this work, we develop seismic modelling and inversion techniques custom-built for limited-offset, limited-bandwidth, ultra-high-frequency (UHF, 0.2-4.0 kHz) seismic reflection data, to obtain a robust decimetric-resolution elastic model of the top 50 m below the seabed. Dedicated signal processing procedures are devised in order to account for the specific bandwidth and acquisition characteristics of UHF data, with the accuracy and the efficiency necessary for pre-stack waveform inversion. A deterministic pre-stack waveform inversion strategy is presented and tested on both complex synthetic and real data. Robustness to noise and sensitivity to the multi-parameter elastic model are tested in relation to the acquisition geometry and the range of physical properties. An original stochastic inversion strategy based on a genetic algorithm is developed in order to improve the robustness to inaccurate starting models. Complex synthetic tests show that this outperforms a conventionally parametrised genetic algorithm, and a real case study demonstrates that this is capable of characterising remotely decimetre-thick shallow weak layers. By using limited a-priori information and minimal data pre-processing, an excellent agreement with the geotechnical ground truth is attained. The deposition of submarine slopes with realistic permeability layerings is simulated, and time-lapse multi-channel UHF seismic data are computed to detect the development of localised excess pore pressure anomalies. The results show that seismic data are sensitive to destabilising excess pore pressure levels with a decimetric resolution. Provided that adequate signal-to-noise ratio data are available, these can be quantitatively interpreted to constrain the in-situ effective stress conditions, and therefore better characterise the stability of a slope. This work demonstrates that the inversion of UHF seismic data has the potential to become an important practical tool for submarine ground model building in spatially heterogeneous areas, reducing the reliance on expensive and time-consuming coring campaigns.

Contents

List of Figures

List of Tables

Acknowledgements

First, I would like to thank my supervisors Mark Vardy, Tim Henstock and Antonis Zervos for the continuous support and invaluable scientific advice. It has been a pleasure working with you, from the very beginning, when I immediately felt welcome as a part of the research group, till the last days of writing up. Needless to say, a great part of this work is primarily the result of stimulating and fruitful scientific discussions among all of us. I would also like to thank John Davis for his support during the eventful cruise in Canada, Hector Marin Moreno for the interesting discussions about geomechanics while the James Cook was cradled by the North Sea swell, and Tim Minshull for the precious advise and encouragement. I look forward to working with you again in the future.

A special thank goes to my better half, Arianna, who shared with me the highs and lows of the past three years, with love and sense of humour. Simply looking at you reminds me how lucky I am, regardless anything else. A particularly important mention to my family, who was always close to me despite the geographical distance, and gave me the love and encouragement I needed, despite the obscure subject of my thesis. I would also like to thank the people that most contributed to making my three years in Southampton memorable: the postgraduate group at NOCS and the italian Erasmus community of the year 2014/2015, with special mention to the 2015 road trip in Scotland, which I will never forget. Finally, I want to express my gratitude towards the countless cafes and libraries that hosted my erratic writing up around Europe, with special mention to Howbery Park in Wallingford and the Public Library of Reading.

Declaration of Authorship

I, **Giuseppe Provenzano**, declare that this thesis and the work presented in it are my own and has been generated by me as the result of my own original research.

Decimetric-resolution elastic characterisation of the shallow subseabed using pre-stack waveform inversion

I confirm that:

1. This work was done wholly or mainly while in candidature for a research degree at this University;
2. Where any part of this thesis has previously been submitted for a degree or any other qualification at this University or any other institution, this has been clearly stated;
3. Where I have consulted the published work of others, this is always clearly attributed;
4. Where I have quoted from the work of others, the source is always given. With the exception of such quotations, this thesis is entirely my own work;
5. I have acknowledged all main sources of help;
6. Where the thesis is based on work done by myself jointly with others, I have made clear exactly what was done by others and what I have contributed myself;
7. Either none of this work has been published before submission, or parts of this work have been published as:

   Provenzano G., Vardy M.E. and Henstock T.J. 2017.
   Pre-stack full waveform inversion of ultra-high-frequency marine seismic reflection data. **Geophysical Journal International**, 209, 1593-1611.
   DOI:10.1093/gji/ggx114

Signed:

Dated:

1 Introduction

In this chapter I introduce the reader to the principles of seismic inversion, and discuss its possible application for the detection of mechanical anomalies relevant to shallow geohazard. The thesis structure is presented, including a brief summary of each chapter.

1.1 The seismic inverse problem

Seismic wave propagation induces a transient deformation field in the subsurface, which is a function of the mechanical properties and density of the host material. As seismic waves propagate, reflections are generated at locations where the physical properties relevant to wave propagation change (Aki and Richards, 2002). The architecture, amplitude and phase of the reflections recorded in seismic surveys are therefore dependent on the distribution of such properties in the subsurface. The aim of seismic interpretation is to infer information from the signal about the propagation medium, and thereby obtain a model of the underground geology, under the assumption that variations in texture, lithology and pore-filling fluid have a footprint in the mechanical response to the seismic

stress-field (Sheriff and Geldart, 1995; Mavko et al., 2009).

Seismic inversion is a quantitative approach to the interpretation of seismic data, whereby the state of knowledge about a given parametrisation of the subsurface is iteratively improved by reducing a measure of the distance between a computed seismic dataset and the observations (Tarantola, 2005). Such a quantity is referred to as the *objective* or *misfit* function.

The recorded seismic reflection signal is referred to as a *seismogram* ($\mathbf{S}$), which is a result of the interaction between the source wavelet signature ($\mathbf{w}$) and the impulse response of the subsurface, or Green's function ($\mathbf{G}$) (Aki and Richards, 2002):

$$\mathbf{S}(t, \mathbf{x}_s, \mathbf{x}_r) = \mathbf{w}(t) * \mathbf{G}(t, \mathbf{x}_s, \mathbf{x}_r) \tag{1.1}$$

where $\mathbf{x}_s$ and $\mathbf{x}_r$ are, respectively, the position of the source and the receiver, and $*$ indicates the convolutional operator. The earth's impulse response ($\mathbf{G}$) is, in turn, a function of the physical model ($\mathbf{m}$) through the wave propagator ($\mathbf{F}$), or *forward* operator (Aki and Richards, 2002; Fichtner, 2011):

$$\mathbf{G}(t, \mathbf{x}_s, \mathbf{x}_r) = \mathbf{F}(\mathbf{m}) \tag{1.2}$$

The subsurface model ($\mathbf{m}$) is the unknown of the seismic inverse problem. In the general formulation of an anisotropic visco-elastic medium, it comprises the Hooke's tensor, density and attenuation factors for P and S wavefields (Aki and Richards, 2002; Mavko et al., 2009). Provided that the source wavelet and acquisition geometry are known, a discrete *parametrisation* of the propagation medium, i.e. a discrete subset of model parameters, can in principle be solved for within the chosen physical approximation (Fichtner, 2011).

However, although Eq. 1.1 is linear, the dependency of the Green's function on the model parameters is non-linear (Eq. 1.2), hence no exact *inverse* operator exists to obtain the physical model from the data (Tarantola, 2005), and the solution must be estimated iteratively. The problem is also non-unique, i.e. potentially infinite combinations of parameter values can describe the observed data equally well. Such problems are described as being *ill-posed*.

The seismic inverse problem is primarily ill-posed as a consequence of inherent limitations in the acquisition geometry and source characteristics, namely the limited source-receiver aperture and limited bandwidth. This is also a function

of algorithmic factors, such as the physical parametrisation of the medium and the characteristics of the misfit criterium (e.g., Operto et al., 2013).

1.1.1 Pre-stack and Post-stack data

In multi-channel seismic exploration (MCS), the wavefield reflected at physical discontinuities in the subsurface is recorded at multiple distance from the source of acoustic energy. For marine MCS, the multiple receivers are towed in a submerged streamer behind the source, recording a limited range of offsets as the source-receiver acquisition system moves along a survey line that is typically much longer than the maximum source-receiver offset. As a result, each point of the subsurface is sampled by the wavefield multiple times, at a range of different reflection angles. During processing, this data redundancy is exploited to attenuate the random noise energy by summing the reflections originating at each *common reflection point (CRP)*, after correcting for the reflection kinematics, such as through normal moveout correction or migration imaging. This process is known as *stacking*, and reduces the random noise energy by a factor proportional to $\sqrt{N}$, where N is the number of traces associated to the same reflection point in the subsurface (Sheriff and Geldart, 1995). Seismic data before stacking are referred to as *pre-stack*, whereas the data after stacking are *post-stack* data.

Pre-stack data contain reflections originating at the same point in the subsurface and recorded at several source-receiver offsets. Therefore, in spite of the higher noise energy, not only do such data contain information about the reflection amplitude, but also about the kinematics of the wavefield through the reflection moveout (Sheriff and Geldart, 1995). Furthermore, the angle-dependent reflection coefficient at an discontinuity is dependent on both P-wave and S-wave impedance contrasts (e.g., Koefoed, 1955; Aki and Richards, 2002), because of the physical coupling of compressional and shear waves (*Zoeppritz* equations; Aki and Richards, 2002).

Post-stack data (Sheriff and Geldart, 1995) are theoretically made up by normal incidence reflection traces only, in which a higher signal-to-noise ratio has been obtained at the expense of the sensitivity to the multi-parameter elastic model (Aki and Richards, 2002). As a consequence of the lack of reflection moveout, post-stack seismic data pose very limited independent constraints on the

kinematics of the wavefield, and are only dependent on the high-frequency acoustic impedance distribution, i.e. the product of P-wave velocity and density.

The inversion of post-stack data for the elastic parameters therefore is heavily ill-posed (Tarantola, 2005; Operto et al., 2013), limiting the possible inversion products to an appropriate parametrisation in terms of acoustic impedance within the seismic spatial resolution (Lindset, 1979; Lee et al., 2013; Vardy, 2015). Most often, the post-stack forward model is cast as a convolution between the seismic wavelet and the series of reflection coefficients in the time domain, which is a zero-offset acoustic Green's function. The main assumptions involved in the time-domain convolutional approach are: (1) source and receiver locations coincide, which requires the geology to be horizontally stratified or, if otherwise, that the reflections have been effectively migrated (Sheriff and Geldart, 1995); (2) the observed data are primary reflections, excluding converted waves and internal multiples; (3) the wavelet is stationary, i.e. the system is *Linear and Time Invariant* (Proakis and Manolakis, 2006); (4) a long-wavelength acoustic impedance model is available, to turn the relative impedances into true impedances and map the time-domain solution into a depth-model (Lindset, 1979; Vardy, 2015).

Pre-stack inversion is performed on the multi-offset seismic data, before stacking traces originating at coincident *CRPs*. Thanks to the dependency of the multi-angle reflection wavefield on the elastic medium, this provides valuable constraints on lithology, pore-filling fluid properties, and drilling hazards, and is therefore a standard reservoir characterisation tool in hydrocarbon exploration (Ostrander, 1984; Ruthenford and Williams, 1989; Mallick et al., 2000; Contreras et al., 2014). *Amplitude Versus Offset/Angle (AVO/AVA)* methods infer the elastic properties of the reflectors by fitting the reflection amplitudes to an approximation of the Zoeppritz equations (Ruthenford and Williams, 1989), after the data have been converted from the time-offset domain to the time-reflection angle domain. *Extended elastic impedance (EEI)* methods are equivalent to a series of post-stack inversions applied to *common-offset* gathers (e.g., Mallick et al., 2000), indirectly obtaining an elastic description of the seismic interfaces by interpreting the changes in the estimated reflection coefficient with the reflection angle. Though providing a more complete description of the elastic medium, EEI and AVO/AVA methods share with the post-stack inversion the limitations of a time-domain convolutional process (Igel et al., 1996; Mallick and Dutta, 2002; Mallick and Adhikari, 2015).

Full Waveform Inversion (*FWI*) (Mora, 1980; Tarantola, 1984, 1986) of reflection data, in contrast, obtains a subsurface model by iteratively minimising the difference between the observed and the computed pre-stack waveforms, including the seismogram in its entirety. Unlike AVO/AVA methods, the forward model is the wave equation, which accounts for all the propagation phenomena within the chosen physical approximation. The inversion of the full waveform often outperforms convolutional methods, especially when complex subsurface structures produce layer interference and tuning, or velocity gradients are present that create uncertainties in the offset to angle conversion (Xu et al., 1993; Igel et al., 1996). Furthermore, FWI in principle optimises both the high and low-frequency of the model (Mora, 1980; Jannane, 1989), providing a broadband distribution of the elastic properties in the subsurface (Mallick and Adhikari, 2015), with a vertical resolution in the order of half a wavelength (Virieux and Operto, 2009; Operto et al., 2013). Despite the higher computational effort, thanks to recent advances in the availability of high-performance computing, FWI is now a widespread procedure in reservoir characterisation (Asnaashari et al., 2012; Mallick and Adhikari, 2015; Aleardi and Mazzotti, 2017), as well as in pure seismology (Bozdag et al., 2011; Fichtner, 2011; Morgan et al., 2013) and seismic oceanography (Wood et al., 2008; Dagnino et al., 2017).

By contrast, very little has been published about the full waveform modelling and inversion of high-frequency marine seismic reflection data, and waveform-based interpretation techniques are rarely applied to the remote characterisation of shallow sub-metric targets. State-of-the-art seismic data acquisition and inversion is more commonly orientated towards hydrocarbon (e.g., Mallick and Adhikari, 2015) and complex geological (e.g., Gulick et al., 2013; Morgan et al., 2014) targets, with a metric to decametric resolution, and a target depth in the order of kilometres. In ultra-high-frequency (UHF, 0.2-4.0 kHz) shallow marine data for target sizes in the order of decimetres and depths in the order of metres, specific acquisition designs and source bandwidths need to be taken into account. Also, the range of physical properties' values of shallow sediments influence the sensitivity of the seismic data to the different elastic properties and density, therefore the inverse problem requires appropriate model parametrisations.

In this Thesis, **Chapter 2** addresses specific modelling issues of UHF data. **Chapter 3** demonstrates that it is possible to apply FWI to shallow marine

multi-channel data, accounting for the specific acquisition geometry and data sensitivity.

1.1.2 Deterministic and Stochastic approaches

The most common implementation of the FWI is the iterative update of a starting background model, based on the local gradient and curvature of the objective function (Tarantola, 1984, 1986; Virieux and Operto, 2009; Fichtner, 2011).

Since the objective function has a highly non-linear dependency on the long wavelength of the model, FWI needs a starting solution accurate enough to match the traveltime with an error less than half the wave-period dominating the misfit (Virieux and Operto, 2009; Fichtner, 2011) in order to avoid *cycle skipping* phenomena (e.g., Mei et al., 2014). Several potential solutions to the cycle skipping problem have been proposed. For example, Bunks et al. (1995b) developed the popular multi-scale approach, in which progressively higher frequencies are inverted. Similarly, Warner and Guasch (2014) proposed an *adaptive waveform inversion*, in which an optimum predictive filter is applied at each iteration with the aim to reduce the time shift between the computed and the observed waveform.

Alternatively, the inversion can be tackled with a Bayesian stochastic approach, by sampling the space of possible solutions (*model space*) with a density proportional to the probability posterior to the observation of the experimental data, or *Posterior Probability Density function (PPD)* (Sambridge and Mosegaard, 2002; Sen and Stoffa, 2013). In addition to being less reliant upon the accuracy of the starting solution, stochastic seismic inversion, in principle, allows extra quality control information to be extracted from the PPD (Sambridge, 1999; Tarantola, 2005), in particular the multi-parameter solution uncertainties and crosstalk resulting from the noise content, the limited offset and bandwidth of the data, and the inherent interdependency of coupled parameters.

Stochastic optimisers such as Genetic Algorithm (Goldberg, 1989), Simulated Annealing (Rothman, 1985) and Particle Swarm Optimisation (Kennedy and Eberhart, 1995), implement analogies between numerical optimisation and natural phenomena to bias the search towards the most promising regions of the model space. They represent a compromise between a systematic exploration of the whole model space, and the exploitation of the current state of

information about the model (Sambridge and Mosegaard, 2002). Although the resulting model distributions are not accurate representations of the PPD (Sen and Stoffa, 1996; Sambridge, 1999; Sambridge and Mosegaard, 2002; Aleardi and Mazzotti, 2017), such methodologies are computationally more affordable than a pure Bayesian approach, and more robust to local minima entrapment than a deterministic algorithm (Tarantola, 1984; Sen and Stoffa, 2013; Sambridge and Mosegaard, 2002).

In **Chapter 4**, I show the application of a genetic algorithm-based stochastic methodology to the inversion of pre-stack UHF waveforms.

1.2 Applications of seismic inversion for shallow sediment characterisation

The physical properties distribution of the top 100 meters below seafloor influences a wide range of offshore engineering contexts and environmental hazards: shallow landsliding on low-angle slopes is preconditioned by the presence of submetric thickness sedimentary horizons with specific soil properties, either acting as a glide plane, or inducing localised low effective stress anomalies by controlling pore-fluid migration pathways (L'Heureux et al., 2012; Vardy et al., 2012); the suitability of a carbon capture and storage (*CCS*) site depends on the decimetric to centimetric scale permeability distribution, and the way this is modified by local changes in effective stress (e.g., Cevatoglu et al., 2015); engineering design of stable and resilient offshore structures, and safe hydrocarbon extraction and transport, benefit from a detailed knowledge of the shallow subsurface response to loading (e.g. Campbell, 1984). A quantitative near-seafloor physical model is therefore a necessity, with a view to reducing the anthropic impact on the marine environment (and vice versa), and minimise human and economic losses.

Current methods for the characterisation of shallow marine sediments rely almost exclusively on direct sampling of the sub-seabed, via boreholes, physical measurements on cores (e.g., *Multi Sensor Core Logging, MSCL*), and *Cone Penetrometer Tests* (*CPT*) (Stoker et al., 2009; Vanneste et al., 2015). These provide decimetric to centimetric vertical resolution information about the top 10 meters below seafloor at a specific location. However, achieving a horizontal resolution sufficient to capture the lateral variability of the shallow geology is expensive and

time consuming. Furthermore, soft soils can be deformed during coring, altering the texture and mechanical behaviour of the sample (Vardy et al., 2017).

Unlike basin-scale geological exploration and hydrocarbon prospection, non-invasive geophysical characterisation techniques are largely underused in shallow ground-model building. These are most often limited to seismic reflection sub-bottom profiling and qualitative seismic-to-core calibration (e.g., Vanneste et al., 2015), whereby a qualitative or semi-quantitative interpretation of the reflection amplitude and architecture guides the interpolation between in-situ measurements (Forsberg et al., 2017). This approach is based on the strong assumption of lateral continuity of the seismic reflector over large (100-1000 meters) distances, and relies on the accuracy of the time-to-depth conversion of the seismic data.

Quantitative geophysical interpretation techniques have been long recognised in academia as a tool for the characterisation of shallow sediments (e.g. Schock et al., 1989; Panda et al., 1994; Nauroy et al., 1998; Pinson et al., 2008), and have recently gained popularity (e.g., Dugan and Sheahan, 2012; Vanneste et al., 2012, 2013; Vardy et al., 2017), thanks to the availability of high-performance-computing resources, and as a consequence of the global financial situation, which makes a priority to extract as much information as possible from existing datasets. In particular, seismic methods can provide important constraint on the low-strain mechanics of the propagation medium, and have the potential to cover large areas in a quick and cost-effective way, providing an horizontal resolution otherwise impossible to achieve (Vardy, 2015).

Specifically, ultra-high-frequency multi-channel seismic surveys can provide decimetric-resolution images in shallow marine environments, and a penetration depth in the order of tens-to-hundreds of meters. This has proven to have the potential to identify and quantitatively characterise sedimentary beds acting as preconditioning factor of submarine slides using post-stack seismic inversion (Vardy et al., 2012; Vanneste et al., 2012; Vardy, 2015); reconstruction of the time-dependent acoustic properties of CCS sites from UHF data has been used to detect gas migration pathways (Cevatoglu et al., 2015); while *quality factor* inversion of broadband data (0.2-13.0 kHz) has been used to characterise the grain size distribution of the near-seafloor (Pinson et al., 2008).

However, we do not propose that seismic remote characterisation should *replace* in-situ soil sampling and geotechnical measurements; rather, we suggest

that, thanks to the time-effective acquisition over large areas, and the non-destructive nature, quantitative interpretation of seismic data has the potential to integrate geotechnical and geological data in geohazard assessment, and/or optimise the design of geotechnical data acquisition campaigns (Carlton et al., 2017).

In particular, the use of seismic reflection data for the remote characterisation of shallow sediments, requires that three inherent limitations are taken into account:

1. Spatial resolution: the seismic resolution and sensitivity to the broadband subsurface model depend on the source bandwidth, the acquisition design and the seismic velocities. As a consequence, landslides' glide planes and fluid migration pathways can have sub-seismic dimensions (millimetric to centimetric; Viesca and Rice, 2012). Consolidation trends are difficult to infer from limited offset, limited bandwidth seismic data (Jannane, 1989; Vardy, 2015), and the reconstruction of the full model bandwidth most often requires integration with a-priori geotechnical information.

2. Stress range: seismic wavefield are sensitive to the mechanical properties of the sediments because they produce a deformation field; the energy produced by a controlled source seismic experiment is normally low and therefore sensitive to the elastic part of the mechanical response of the propagation medium (Powrie, 2002; Mavko et al., 2009). This excludes strain-softening effects, or soil activity, which can be a factor in submarine slope instability (Viesca and Rice, 2012; Madhusudhan et al., 2017).

3. Relevant physics: the set of parameters seismic data is sensitive to (elastic moduli and density) is only partially overlapping with the domain of the properties necessary to describe the behaviour of a sediment for geohazard or engineering purposes, e.g., grain size, effective stress, permeability. Permeability, in particular, is only loosely constrained by seismic data (Vardy et al., 2017).

Seismic reflection data are sensitive mostly to geotechnical and geological anomalies affecting the bulk properties of the sediment body as an equivalent propagation medium (Mavko et al., 2009). Among the most relevant for offshore engineer-

ing design and geohazard assessment, seismic data can be useful to characterise the following:

1. Localised anomalies of effective stress induced by permeability heterogeneities at specific stratigraphic horizons (Dugan and Flemings, 2000); such changes in the relative proportion of pore space and soil grain volume have a strong effect on the seismic response of a sediment, especially on P-wave propagation (Vardy et al., 2017).

2. Variations in the compressibility of the fluid phase filling the pore space have a strong effect on the sediment bulk compressibility and density. Therefore partial gas saturation, for example, has a definite signature on the ratio between the P- and S- wave seismic velocities (Ruthenford and Williams, 1989).

3. Variations of lithology can produce detectable seismic layerings (Igel et al., 1996; Mallick and Adhikari, 2015).

UHF seismic data can therefore contribute to identifying areas preconditioned to landsliding, where overpressure build-up is a factor in the in-situ stability conditions (Dugan and Sheahan, 2012; Vanneste et al., 2015; Vardy et al., 2017), detect shallow gas saturation (Vanneste et al., 2013; Morgan et al., 2014), fluid leakage from storage sites (Cevatoglu et al., 2015), and lithological heterogeneity.

As an example, in **Chapter 5**, I show that UHF seismic data are sensitive to the development of weak layers due to shallow excess pore pressure build-up during deposition, and that it is in principle possible to invert those data using the techniques developed in **Chapter 3** and **4**.

1.3 Thesis outline

The work presented in this Thesis attempts to answer the following fundamental questions:

1. Is it feasible to model and invert the full waveform of ultra-high-frequency marine reflection data?

2. Is this robust to the bias of inaccurate a-priori information?

3. Can we detect sub-metric effective stress anomalies in submarine slopes?

1.3.1 Chapter Synopses

Chapter 2 addresses the choice of the forward operator for the full waveform inversion and details the specific techniques developed to account for the specific characteristics of ultra-high-frequency seismic reflection data. Part of this chapter has been published as an appendix to (author list reflective of relative contributions): *Provenzano G., Vardy M.E. and Henstock T.J. 2017. Pre-stack full waveform inversion of ultra-high-frequency marine seismic reflection data. Geophysical Journal International 209, 1593-1611.*

Chapter 3 presents a deterministic pre-stack inversion approach for the characterisation of the elastic properties of the shallow subsurface with a decimetric resolution. Robustness to noise and sensitivity issues are discussed in relation to the chosen parametrisation. A real case study is presented where the elastic FWI results are compared with the geotechnical ground-truth. This chapter has been published as (author list reflective of relative contributions): *Provenzano G., Vardy M.E. and Henstock T.J. 2017. Pre-stack full waveform inversion of ultra-high-frequency marine seismic reflection data. Geophysical Journal International 209, 1593-1611.*

Chapter 4 explores the potential of the Genetic Algorithm as a stochastic optimiser robust to local minima entrapment, and as a tool for the estimation of solution confidence intervals. An original exploration strategy has been developed and combined with a specific choice of objective function. It is finally shown that genetic algorithm-based FWI of UHF data is able to identify and characterise a decimetre-thick weak layer in a real case study, and detect its partial gas saturation. This chapter has been submitted to *Geophysical Journal International* for publication (author list is reflective of relative contributions): *Provenzano G., Vardy M.E. and Henstock T.J. 2018. Decimetric-resolution stochastic inversion of shallow marine seismic reflection data; dedicated strategy and application to a geohazard case study. Submitted to Geophysical Journal International.*

Chapter 5 presents a set of synthetic consolidating slope models producing complex overpressure profiles during deposition as a consequence of permeability heterogeneities. Time-lapse multi-channel seismic data are generated to test the sen-

sitivity to potentially destabilising under-compaction anomalies. The computed seismic data present similar characteristics to the ones which seismic inversion has been applied to in the previous chapters, and we discuss the potential application of seismic inversion as a means to identify shallow excess pore pressure anomalies. This part of the work uses, and adapts to the heterogeneous case, a mathematical formulation developed by A. Zervos for homogeneous infinite slopes with moving sediment/water boundary. This chapter is in preparation for submission to *Quarterly Journal of Engineering Geology and Hydrogeology.*

2

Modelling of near-surface marine seismic reflection data

This chapter addresses the accurate and efficient simulation of the ultra-high-frequency (UHF,$0.2 - 4.0kHz$) marine seismic reflection wavefield, necessary for the quantitative interpretation of the field data. The main topics covered are:

- The choice of a one-dimensional elastic isotropic forward modelling engine.
- The simulation of the source antennas and receiver arrays directivity.
- The data-driven reconstruction of the offset-varying receiver depth and its efficient simulation in the $f - \kappa$ domain, integrating the one-dimensional solver (published in short form as an appendix to Provenzano G., Vardy M.E. and Henstock T.J. 2017. Pre-stack full waveform inversion of ultra-high-frequency marine seismic reflection data. **Geophysical Journal International**, 209, 1593-1611. DOI:10.1093/gji/ggx114)

2.1 Choice of the forward model for stratified elastic media

An appropriate approximation of the wave equation is the core of any seismic inversion algorithm, and needs to represent the relevant physics of the problem within an acceptable computing cost.

Unlike traveltime tomography, full waveform inversion (FWI) simulates wave propagation in its entirety (Virieux and Operto, 2009), within the subset of discrete physical properties chosen to represent the medium. Once a physical model has been chosen for the subsurface, a numerical solution can be obtained by discretising the partial derivative equation in finite difference, or, alternatively, discretising the propagation medium into finite elements (Fichtner, 2011).

FWI is often performed using the acoustic approximation, to obtain a detailed three-dimensional P-wave velocity model of complex subsurface structures (e.g. Tarantola, 1984; Virieux and Operto, 2009; Fichtner, 2011; Morgan et al., 2013). However, the acoustic approximation neglects an important part of the physics of the wave propagation in heterogeneous media, even if only P-waves are recorded (Aki and Richards, 2002).

The amplitude and phase of the reflections recorded at different incidence angles also depend on the shear properties contrast between layers (Koefoed, 1955; Ostrander, 1984; Aki and Richards, 2002); variations in the P-S converted energy affect P-wave amplitudes (Aki and Richards, 2002), and P-to-S-to-P converted waves can be observed at wide reflection angles (Kormendi and Dietrich, 1991); independent high-frequency changes of density and P-wave velocity at constant acoustic impedance, to which traveltimes are invariant (Jannane, 1989), can produce changes in the reflected amplitude (Mallick and Adhikari, 2015; Silverton et al., 2015; Provenzano et al., 2017). Due to the strong link with the effective stress conditions of the sediments (Mallick and Dutta, 2002; Dugan and Sheahan, 2012; Vanneste et al., 2015; Vardy et al., 2017), pore-fluid saturation (Ruthenford and Williams, 1989; Provenzano et al., 2016) and lithological changes (Igel et al., 1996; Mallick and Adhikari, 2015), the aforementioned wavefield characteristics are key to geohazard-orientated seismic exploration.

Therefore, the acoustic medium approximation does not fit the purpose of seismic inversion for geohazard analysis; on the other hand, although fully visco-

elastic and anisotropic modelling provides the most complete representation of the seismic wave propagation, its computational cost makes this approach hardly affordable for the most commonly available high-performance computing solutions. A compromise is thus necessary between an appropriate representation of the physics of the problem, and a sustainable computing cost (Mallick and Adhikari, 2015).

The approximation we choose to make is that of an isotropic, elastic medium that can be realistically approximated as horizontally stratified in the range of the imaging aperture (Virieux and Operto, 2009). In UHF seismic, this would be in the order of tens of m. Despite an inherent loss of horizontal resolution, such assumption can be considered acceptable in shallow and weakly tectonised sediments.

A one-dimensional approximation permits to use homogeneous-layer solutions belonging to the class of reflectivity or wavenumber integration methods (e.g. Fuchs and Müller, 1971; Mallick and Frazer, 1987; Schmidt and Jensen, 1985; Schmidt and Tango, 1986.), which are significantly faster than finite difference or finite element solutions (Aki and Richards, 2002; Shearer, 2009; Fichtner, 2011).

2.1.1 An outline of the homogeneous-layer formulation

In the homogeneous-layer formulation, the subsurface is parametrised as a stack of horizontal elements, defined by a set of two independent elastic parameters and density. Within each layer, an analytical solution of the wave equation is computed for each frequency-horizontal slowness pair ($f - s_x$), and matrix methods are used to propagate the solution to adjacent layers. Boundary conditions of continuity of displacements and tractions must be satisfied at each interface, and the obtained frequency-slowness spectrum is integrated to yield the time-offset domain seismogram (e.g. Shearer, 2009).

Here I briefly summarise the fundamental equations for the propagation of a frequency-slowness pair through an arbitrary number of homogeneous layers. For simplicity, only the transversal horizontal particle motion is considered, following the derivation of Shearer (2009). A complete mathematical formulation for the three-dimensional particle motion can be found in Fuchs and Müller (1971) and Aki and Richards (2002).

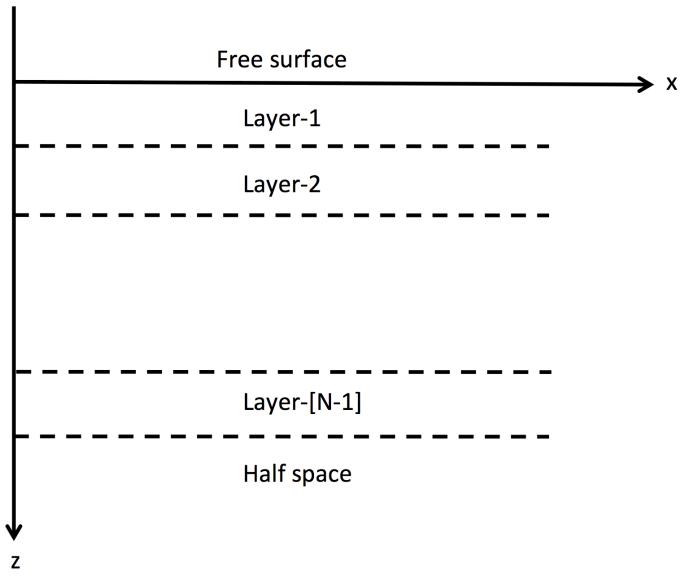

Figure 2.1: **A homogeneous layer medium model**. Adapted from Mallick and Frazer (1987)

I define u_y the displacement field at depth z_i produced by upgoing and downgoing monochromatic plane waves propagating in the xz half space in Fig. 2.1, with fixed frequency f and horizontal slowness s_x.

$$u_y = A_d e^{(-j2\pi f(t-s_x x))} e^{j2\pi f s_z z_i} + A_u e^{(-j2\pi f(t-s_x x))} e^{-j2\pi f s_z z_i} \tag{2.1}$$

where A_d is the amplitude of the downgoing wave and A_u is the one of the upgoing wave. The associated stress component acting on the surface normal to the *z-axis* is: $\tau_{yz} = \mu \frac{\partial u_y}{\partial z}$. Therefore, we have:

$$\tau_{yz} = \mu j2\pi f s_z A_d e^{(-j2\pi f(t-s_x x))} e^{j2\pi f s_z z_i} - \mu j2\pi f s_z A_u e^{(-j2\pi f(t-s_x x))} e^{-j2\pi f s_z z_i} \tag{2.2}$$

Those quantities can be conveniently arranged in a stress-displacement vector, where we decompose the depth dependent part from the term representing the horizontal propagation:

$$\mathbf{H}(z_i) = \begin{bmatrix} u_y \\ \tau_{yz} \end{bmatrix} = \begin{bmatrix} e^{j2\pi f s_z z_i} & e^{-j2\pi f s_z z_i} \\ \mu j2\pi f s_z e^{j2\pi f s_z z_i} & -\mu j2\pi f s_z e^{-j2\pi f s_z z_i} \end{bmatrix} \begin{bmatrix} A_d \\ A_u \end{bmatrix} e^{-j2\pi f(t-s_x x)} \tag{2.3}$$

We can express Eq. 2.3 in a more compact form:

$$\mathbf{H}(z_i) = \mathbf{F}_i \mathbf{a}_i e^{-j2\pi f(t - s_x x)} \tag{2.4}$$

where $\mathbf{F}$ is the matrix containing the depth dependent layer properties (*layer matrix*) and $\mathbf{a}$ is the vector of upgoing and downgoing amplitudes.

Within the same layer, we now propagate the solution between two arbitrary depths, z_i to z_q. By defining $\mathbf{f}(z_i) = \mathbf{F}_i \mathbf{a}_i$, the amplitude vector is:

$$\mathbf{a}_i = \mathbf{F}_i^{-1} \mathbf{f}(z_i) \tag{2.5}$$

In a purely elastic medium the amplitudes of the plane waves are constant within the same layer, which allows $\mathbf{f}(z_q)$ to be expressed as:

$$\mathbf{f}(z_q) = \mathbf{F}_q \mathbf{F}_i^{-1} \mathbf{f}(z_i) \tag{2.6}$$

Eq. 2.6 propagates the stress-displacement vector between two arbitrary depths in a homogeneous medium. Therefore it can be used to propagate the wavefield between the top and the bottom of the layer. For layer 1:

$$\mathbf{f}(z_{b1}) = \mathbf{F}_{b1} \mathbf{F}_{t1}^{-1} \mathbf{f}(z_{t1}) \tag{2.7}$$

where t and b respectively refer to top and bottom of the layer. $\mathbf{P}_1 = \mathbf{F}_{b1} \mathbf{F}_{t1}^{-1}$ is the *propagator matrix* of layer 1.

Once the wavefront encounters an interface, the solution will be propagated to the following layer. Continuity of the stress-displacement vector (Eq. 2.3) and kinematic continuity along the interface prescribe:

$$\mathbf{f}(z_{b1}) = \mathbf{f}(z_{t2}) \tag{2.8}$$

where the numbers indicate the layer index. Thereby:

$$\mathbf{F}_{b1} \mathbf{a}_1 = \mathbf{F}_{t2} \mathbf{a}_2 \longrightarrow \mathbf{a}_2 = \mathbf{F}_{t2}^{-1} \mathbf{F}_{b1} \mathbf{a}_1 \tag{2.9}$$

which solves for the unknown wave amplitude after the wavefront has crossed the interface between layers 1 and 2.

We can now propagate the solution of the wave equation through an arbitrary number of layers. Eq. 2.6, by virtue of the continuity conditions expressed in

Eq. 2.8, effectively propagates the stress-displacement vector from layer k to layer $k+1$. It therefore follows that:

$$\mathbf{f}(z_{top2}) = \mathbf{P}_1\mathbf{f}(z_{top1}) \rightarrow \mathbf{f}(z_{top3}) = \mathbf{P}_2\mathbf{P}_1\mathbf{f}(z_{top1}) \tag{2.10}$$

and, for a generic depth within layer N:

$$\mathbf{f}(z_N) = \prod_{k=1}^{N-1} \mathbf{P}_k\mathbf{f}(z_1) \tag{2.11}$$

These equations describe the propagation of horizontally polarised S-waves (SH) through a layered medium. The propagator matrix approach applies also to the P-SV propagation system (i.e. P-wave and S-wave polarised in the propagation plane), where the stress-displacement vector ($\mathbf{H}$) in Eq. 2.3 contains the in-plane components of displacement and traction for which continuity must be solved at each interface:

$$\mathbf{H}(z_i) = \begin{bmatrix} u_x \\ u_z \\ \tau_{xz} \\ \tau_{zz} \end{bmatrix} \tag{2.12}$$

As both P- and S- wave contribute to the x and z components of the stress and displacement fields at non-zero incidence angles, it follows that compressional and shear waves are coupled in the xz plane. An exhaustive description of the P-SV propagation system can be found in (Aki and Richards, 2002).

Several examples of different numerical implementations are present among the references provided (e.g Mallick and Frazer, 1987). In this work, we use the implementation of *Ocean Acoustics and Seismic Exploration Synthesis (Oases)*, from Schmidt and Jensen (1985); Schmidt and Tango (1986.). Unlike more traditional methods employing recursively propagator matrixes within each layer, it uses a global matrix approach to solve the wave equation for all the layers simultaneously. This numerical implementation reduces the number of arithmetic operation needed and is thus preferable in computations involving high-frequencies, numerous receivers and high number of layers (Schmidt and Jensen, 1985). The output from the one-dimensional solver is the multi-offset Green's Function of the layered subsurface, which is in a second step convolved with an estimate of the source wavelet.

However, source and receiver arrays, and complex streamer geometries are not efficiently simulated within the wave equation solver; further modelling steps are thus necessary to account for the specific characteristics and geometries of the source-acquisition system in near-surface UHF marine seismic reflection data.

2.2 Simulating source and receiver antennas

UHF seismic sources, such as Boomer and Sparker systems, act as finite-dimension acoustic energy generators (Verbeek and McGee, 1995; Riedel and Theilen, 2001), whose radiation pattern markedly deviates from the ideal isotropic point source impulse response. This is instrumental in reducing the energy of the source ghost, and contributes to attenuating high-frequency horizontally propagating seismic arrivals that can be conducive to spatial aliasing (Sheriff and Geldart, 1995; Proakis and Manolakis, 2006).

The acoustic energy is recorded at different offsets by a multi-channel acquisition system; each channel outputs a seismic trace which results from the stack of signals recorded by a group of closely spaced hydrophone elements. Analogously to a directional acoustic source, the receiver group filters the steeply dipping, high frequency energy of the wavefield, therefore acting as discretised anti-aliasing antenna.

From a signal processing point of view, a receiver group acts exactly as a an array of sources with identical geometry, and both contribute to filtering the spatial frequencies of the wavefront sampled by each channel. For a horizontal array, the *apparent* spatial frequency is the one propagating along the horizontal (x) dimension (Sheriff and Geldart, 1995; Shearer, 2009). We define the quantity horizontal wavenumber as:

$$\kappa_x = 2\pi f sin(\theta)/V_w \tag{2.13}$$

where f is the temporal frequency, V_w is the velocity of the medium and θ is the angle of the wavefront with respect to the horizontal. For brevity, in this section we will hereafter refer to it simply as *wavenumber*.

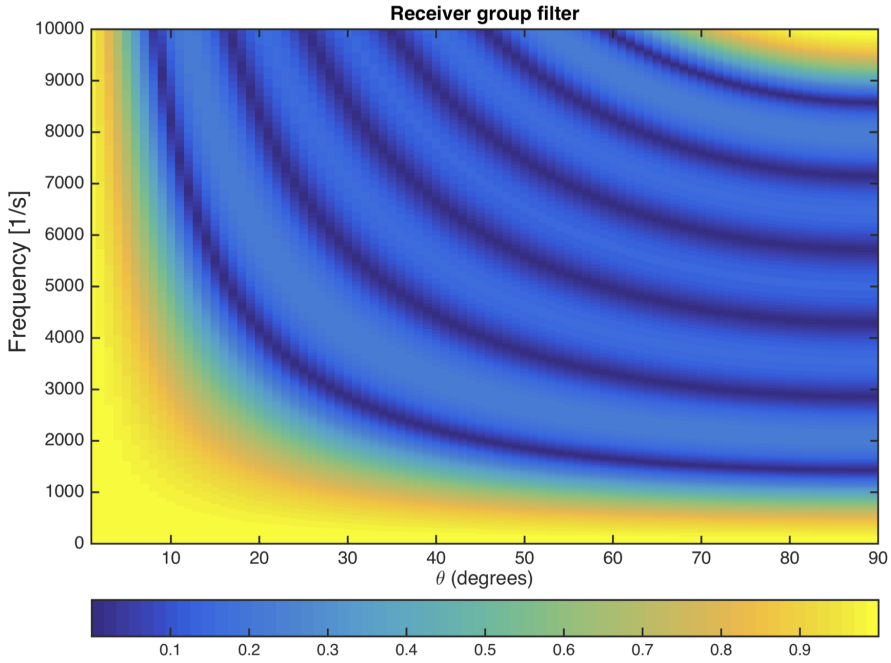

Figure 2.2: **Transfer function of a linear receiver array**. The linear receiver group is made by 7 elements with 0.15 m spacing.

In the following formulation, we focus on the effect of the spatial response of the source and acquisition system, and assume that the temporal frequency source and receiver transfer functions are white. Under this assumption, the seismic trace $\mathbf{R}$ can be compactly expressed in the wavenumber domain as a product of linear filters' impulse responses:

$$\mathbf{R}(\kappa_x) = \mathbf{S}(\kappa_x)\mathbf{C}(\kappa_x)\mathbf{G}(\kappa_x) \tag{2.14}$$

where:

- $\mathbf{G}$ is the wavenumber-transform of the Green's function (Aki and Richards, 2002) of the propagation medium for the source-receiver group couple, output from the wave equation solver.
- $\mathbf{C}$ is the transfer function of the receiver antenna, which can be computed from the known receiver group characteristics.
- $\mathbf{S}$ is the transfer function of the source system, computed from the specific source device geometry.

For a discrete linear array of N receivers (or point sources), with spacing d, the transfer function reads:

$$\mathbf{C}(k) = \frac{sin(N/2 \cdot \kappa_x \cdot d)}{Nsin(1/2 \cdot \kappa_x \cdot d)} \tag{2.15}$$

or, using the equivalence from Eq. 2.13:

$$\mathbf{C}(f, \theta) = \frac{sin\left(N\pi \frac{fsin(\theta)}{V_w} d\right)}{Nsin\left(\pi \frac{fsin(\theta)}{V_w} d\right)} \tag{2.16}$$

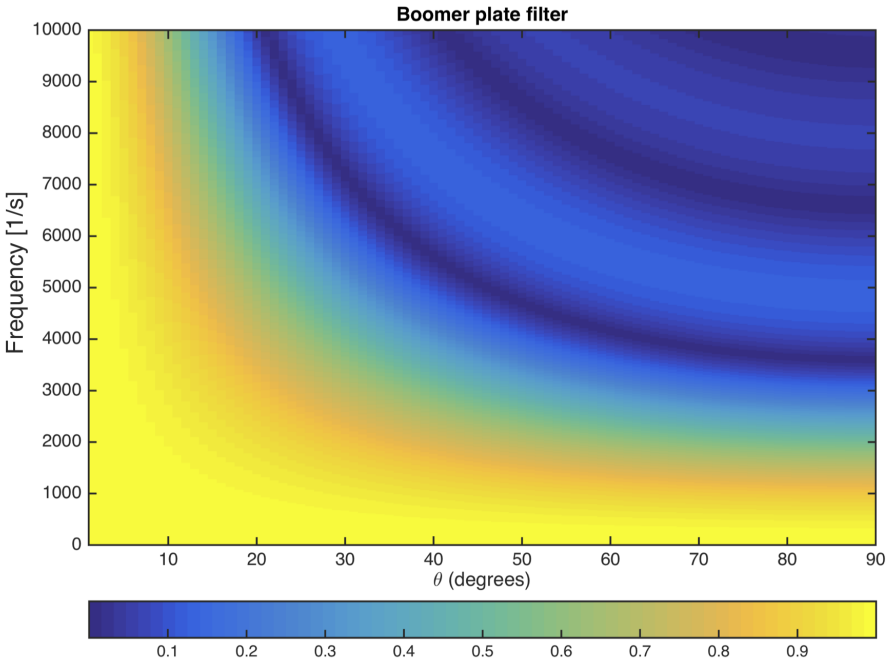

Figure 2.3: **Radiation pattern of a Boomer plate**. Diameter is 0.4 m.

Either of Eqs. 2.15 and 2.16 is sufficient to describe the impulse response of a linear receiver array.

It is worth pointing out the following: (1) for each temporal frequency, a specific antenna radiation/acquisition pattern of the source/receiver group can be computed; (2) for each take-off angle θ, the array acts as a high-cut filter in temporal frequency f; (3) The period of the notches of the transfer function

is inversely proportional to the product $N \cdot \ d$, so that longer receiver groups are more selective wavenumber filters; (4) on the other hand, at a fixed receiver array length, fewer elements (higher d) would determine a shorter period of the wavenumber transform (Proakis and Manolakis, 2006), hence more closely spaced secondary maxima lobes in the receiver group's antenna response.

Fig. 2.2 shows the frequency versus incidence angle response of a receiver group composed on 7 elements with spacing equal to 0.15 m; note that the higher the frequency, the lower the first notch-angle; as a consequence, far offsets (wider reflection angles) reflected arrivals are going to be low-pass filtered compared to the short offsets.

Estimating the directivity of high-resolution sources, on the other hand, requires a correction for the specific size and shape of the device, which is, unlike airgun-arrays (Igel et al., 1996), not exhaustively described by a linear array of point sources. For example, the frequency-angle response of a Boomer system, depends of the diameter of the electro-acoustic plate, as in Riedel and Theilen (2001):

$$\mathbf{S}(f,\theta) = \frac{2J_1\left(\pi \frac{fsin(\theta)}{V_w} D\right)}{\left(\pi \frac{fsin(\theta)}{V_w} D\right)} \tag{2.17}$$

where J_1 is the first-order Bessel function of the first kind and D denotes the plate diameter. In Fig. 2.3 we plot the frequency-angle response of a Boomer plate with diameter of 0.4 m.

The frequency-dependent directivity functions presented in Figs. 2.2 and 2.3 are appropriate the *Applied Acoustics AA330* Boomer and bespoke multi-channel streamer used for UHF MCS surveys at the University of Southampton. Together, these functions have a significant footprint on the amplitude and phase of the reflected wavefield (Igel et al., 1996; Riedel and Theilen, 2001). Therefore, they need to be taken into account within the FWI forward operator, in order for the waveform amplitude and shape to be consistently compared with the field data.

2.3 Reproducing acquisition conditions for shallow marine data

In UHF marine seismic reflection data, receiver depths in the order of a few metres produce receiver ghosts inside the bandwidth of the signal, and sub-metric scale variations of the streamer geometry as a function of offset cause non-negligible changes in the source-acquisition system impulse-response (Pinson, 2009). Significantly sagging streamer geometries are often observed in the marine-lacustrine setting typical of UHF seismic (Pinson, 2009). Furthermore, the sea-surface topography approaches the seismic wavelength of a UHF wavefield, causing the sea-surface reflection coefficient to change significantly across the streamer length.

In this work we chose to explicitly include these factors in the computation of the synthetic seismograms, as opposed to applying deconvolution on the observed data. Although inverse ghost filtering would yield a spectral whitening that can be beneficial to the seismic resolution, it is liable to create artefacts inside the bandwidth of the signal which could severely undermine the inversion performance. However, an explicit full wavefield modelling would require to solve one forward model for each receiver offset-depth couple in the appropriate wavenumber bandwidth. Since the wavenumber ranges necessary to model each offset are largely overlapping, this approach is clearly inefficient and results in a non-affordable computing cost.

We developed an efficient total seismogram modelling method, which requires only the computation of the pure up-going wavefield at one arbitrary receiver depth, and derives the whole gather in the frequency-wavenumber domain using wavefield decomposition (Verschur et al., 1992; Aytun, 1999). For each channel, the prediction of the down-going wavefield and the downward propagation in the plane wave domain are implemented as a linear filter with the estimated receiver depth and sea-surface reflection coefficient; an inverse two-dimensional Fourier transform gives a seismic gather in an expanded offset range from which the trace at the appropriate offset is selected. The final predicted seismogram is then obtained by merging the different offsets.

Compared to a full wavefield modelling approach, the proposed alternative allowed for a reduction of the computing time of one order of magnitude.

2.3.1 Receiver ghost modelling

A recorded seismic reflection pressure wavefield is the convolution between a purely up-going wavefield and the impulse response of the acquisition system as a function of receiver depth, free-surface reflection coefficient and spatial frequency (Aytun, 1999). The total wavefield at depth h in the frequency-wavenumber domain can be obtained from the up-going field $\mathbf{P}_k{}^{-}(h_0)$ as:

$$\mathbf{P}_k(h, r_0) = \mathbf{P}_k{}^{-}(h_0)\mathbf{F}1_k(h, r_0)\mathbf{F}2_k(h, h_0) \tag{2.18}$$

where:

$$\mathbf{F}1_k(h, r_0) = (1 + r_0 e^{(-j2k_z h)}) \tag{2.19}$$

predicts the receiver ghost at depth h as a function of the vertical wavenumber $k_z = \sqrt{k^2 - k_x^2}$, with a free-surface reflection coefficient equal to r_0.

$$\mathbf{F}2(h, h_0) = e^{(jk_z(h-h_0))} \tag{2.20}$$

is the downward propagation operator from h_0 to h accounting for the traveltime difference for each plane-wave component. The time-offset domain seismogram is obtained via two-dimensional Fourier inverse transformation:

$$\mathbf{d}(t, x) = \mathcal{F}^{(-1)}\{\mathbf{P}_k(h, r_0)\} \tag{2.21}$$

In the general case of offset-varying streamer depth and sea-surface reflection coefficient, the complete N-channels seismic gather can be obtained by selecting each trace from the corresponding redundant-offset domain gather and then merging the offsets. A compact mathematical formulation exploits the properties of the two-dimensional *Dirac* delta function:

$$\mathbf{d}_i(t, x) = \mathcal{F}^{(-1)}\{\mathbf{P}_k(h(i), r_0(i))\} \tag{2.22}$$

$$\mathbf{d}(t, x) = \sum_{i=1}^{N} \int_{-\infty}^{+\infty} \int_{-\infty}^{+\infty} \delta(t - \tau, x_i)\mathbf{d}_i(\tau, x_i) d\tau dx \tag{2.23}$$

As opposed to an explicit full wavefield modelling, only the computation of the up-going wavefield at constant depth is required, and the whole gather is obtained by signal manipulation, with significant savings in the computing cost.

In the region of the $f - \kappa$ domain corresponding to non-physically propagating waves (Aki and Richards, 2002), where the horizontal (apparent) wavenumber is

higher than ω/λ, k_z becomes complex-valued, making the complex exponential a diverging function which creates numerical instability. To clarify this point, we can decompose the $f-\kappa$ ghosting filter into a stable (S) and an unstable (U) contribution:

$$\mathbf{F}1_k(z)\mathbf{F}2_k(z,z_0) = S(z,z_0) - U(z,z_0) \tag{2.24}$$

where

$$S = e^{\{[-im(ck_z)][z-z_0]\}}e^{(j(z-z_0)re(ck_z))} \tag{2.25}$$

and

$$U = e^{\{[+im(ck_z)][z+z_0]\}}e^{(-j(z+z_0)re(ck_z))} \tag{2.26}$$

where r_0 is set equal to -1, and we indicated the complex wavenumber as ck_z and its imaginary and real part respectively with im and re. Eq. 2.26 illustrates how the diverging exponential first term of U can create unwanted amplitude effects on the high k_x portion of the $f-\kappa$ spectrum. A simple *butterfly shaped* mask valued one around the evanescent region is sufficient to prevent the inverse filtering from diverging.

To test the capabilities of the method, a simple seismic gather has been simulated over a 1D model consisting of a 50 m deep water layer and an underlying homogeneous elastic half space (Fig 2.4). The model contains a free-surface and the receiver depth is equal to $5m$ and constant throughout the streamer, which consists of 60 receivers 1 m apart with a minimum offset of 13 m. Though the synthetic dataset is simulated as a common shot gather, in the 1D approximation makes it equivalent to a common depth point (CDP) gather with fold equal to 60 (Sheriff and Geldart, 1995). The free-surface reflection coefficient is equal to -1 . The bandwidth of the source ranges from 0.2 to 1.5 kHz. This simple synthetic dataset is used as a benchmark to test the accuracy of the method and will be hereafter referred to as *explicit total wavefield*.

The source depth in the benchmark synthetic data is in the order of a few centimetres, $i.e << \lambda/8$ for the maximum frequency and velocity range of the model. In such a configuration the polarity reversed down-going wavefield interferes with the up-going wavefield with a time delay approximating an infinitesimal *dt*. The effect on the signal is similar to a thin layer impulse response: a wavelet

rotation and linear frequency increase simulating a finite difference first derivative (Widess, 1973). This has been compensated for using the integral of the estimated source signature with satisfactory results in terms of wavelet shape.

Using the same elastic model, a seismic gather has been generated with no free-surface and zero receiver depth (Fig 2.4). The *Ghosting+downward propagation* $f-\kappa$ filter is implemented as from Eq. 2.18, with constant receiver depth throughout the offset range and r_0 equal to -1 . Since the system is linear, the total seismogram including the receiver ghosts can be obtained by multiplying the complex two-dimensional spectrum of the purely up-going wavefield and the $f-\kappa$ impulse response of the filter (Proakis and Manolakis, 2006) (Fig 2.5). The resulting seismic matrix (which we will refer to as *fast total wavefield*) is obtained by back-transformation of the $f-\kappa$ complex spectrum (Fig. 2.6).
Note how the null amplitude loci in the $f-\kappa$ domain have the shape of hyperbolae asymptotic to the water acoustic wave velocity slope, while in the $t-x$ domain the traveltime are correctly reconstructed (Figs. 2.5 and 2.6).

In order for the $f-\kappa$-domain filtering to be accurate and to avoid undesired linear time-offset domain artefacts (Fig. 2.7, panel *a*) an improvement of the wavenumber resolution with respect to the starting seismic data is necessary; this is generally true for near-surface reflection seismic real data, which normally employs a relatively short receiver cable. A trace zero-padding producing a 30% increase of the spectral resolution is applied to the seismic data and effectively removes the non-physical seismic phases in the final seismogram (Fig. 2.7).

It's also apparent from figure 2.7 (panel *a*) how the downward propagation of the wavefield in the plane-wave domain produces anomalous reduction of the reflection amplitudes at longer offset/higher slowness (p). If the choice of padding traces is justified by the need of a higher wavenumber resolution, the correct reconstruction of the signal amplitude throughout the matrix requires a wider slowness bandwidth than the one contained in the down-going zero-depth wavefield, to account for the wider reflection angle of the desired seismogram. The effect of expanding the offset domain of the non-free surface synthetics (and, as a result the range of available slownesses) is shown in figure 2.7, panel b: 8 traces are symmetrically added and a perfect match is attained between the $f-\kappa$-predicted data and the benchmark.

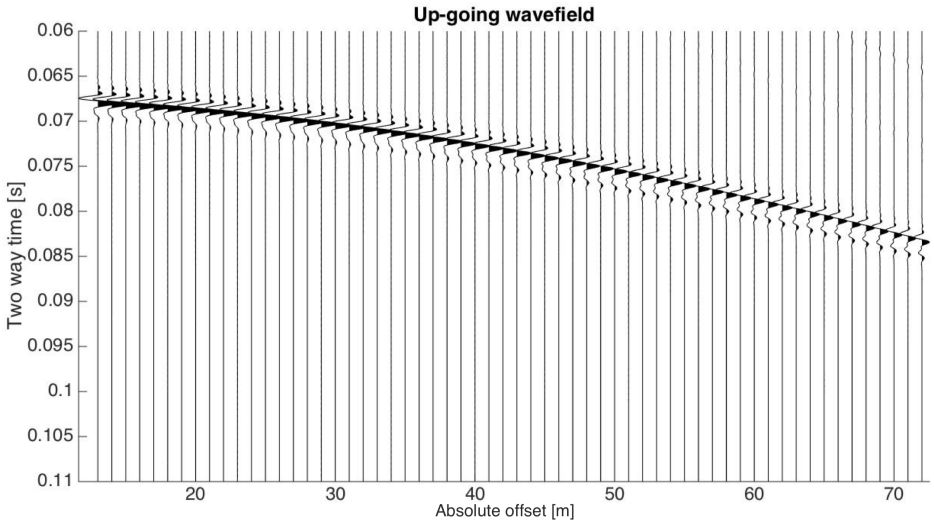

(a)

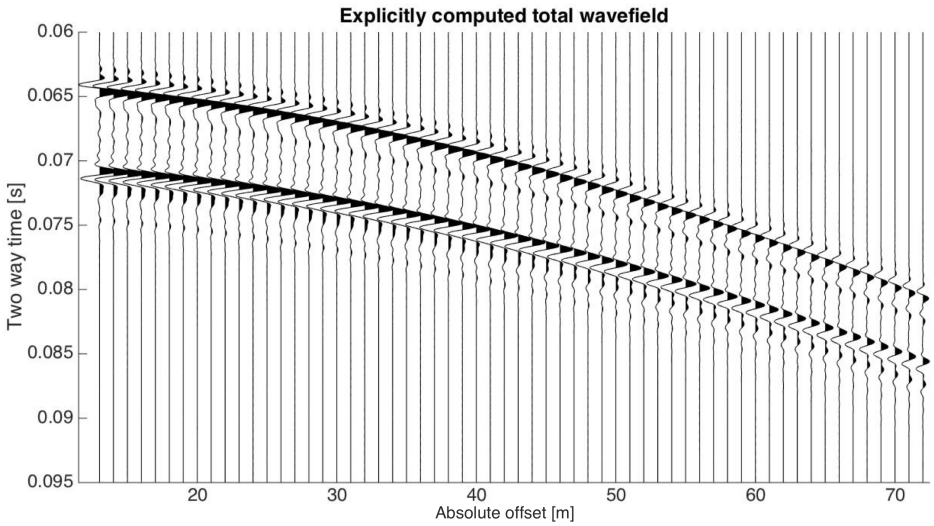

(b)

Figure 2.4: **Synthetic seismograms.** Panel a): Up-going wavefield only. No free surface, zero receiver depth seismogram. Panel b): Total wavefield used as benchmark. Free surface, 5 m receiver depth seismogram.

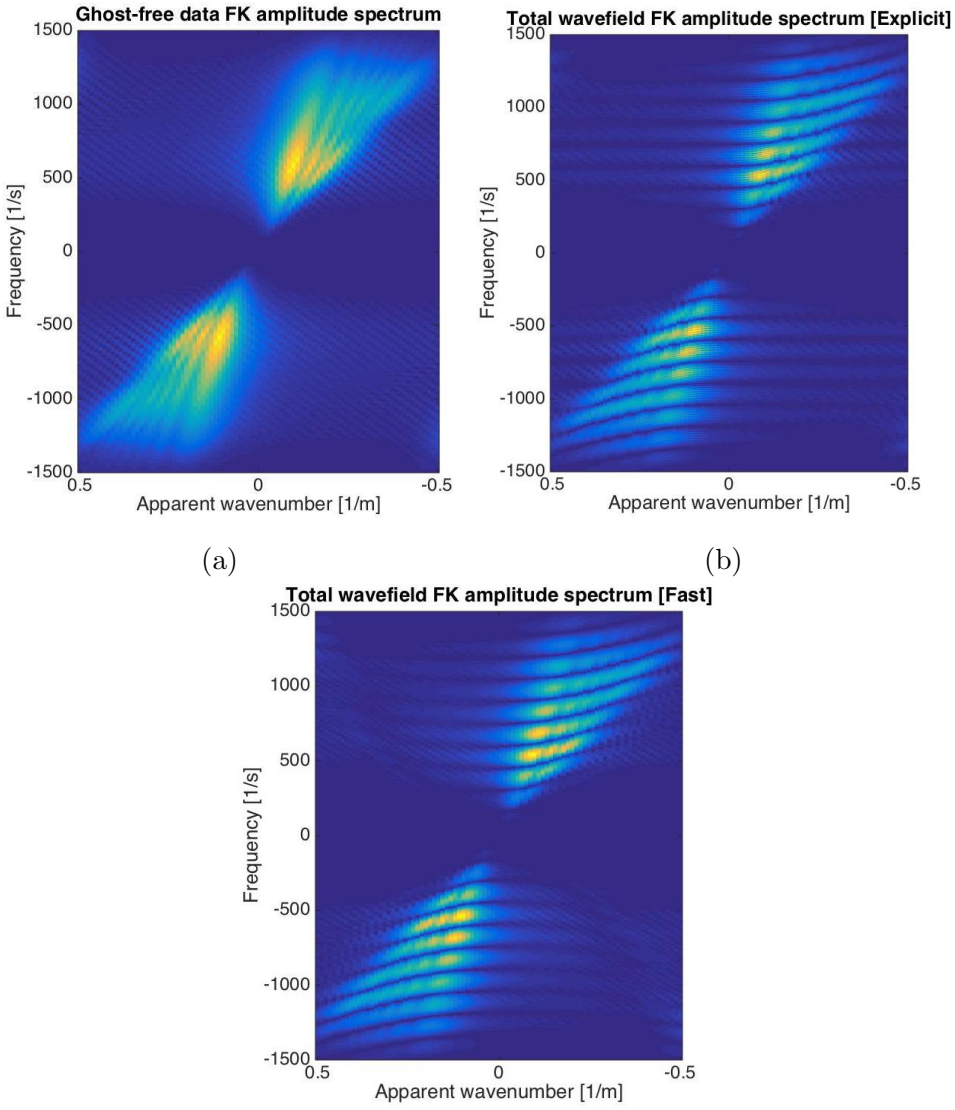

Figure 2.5: **Ghosting in $f-\kappa$ domain.** In panel a) $f-\kappa$ amplitude spectrum of the ghost-free data compared with the total wavefield in panel b. In panel c) the $f-\kappa$ amplitude after the application of the ghosting filter.

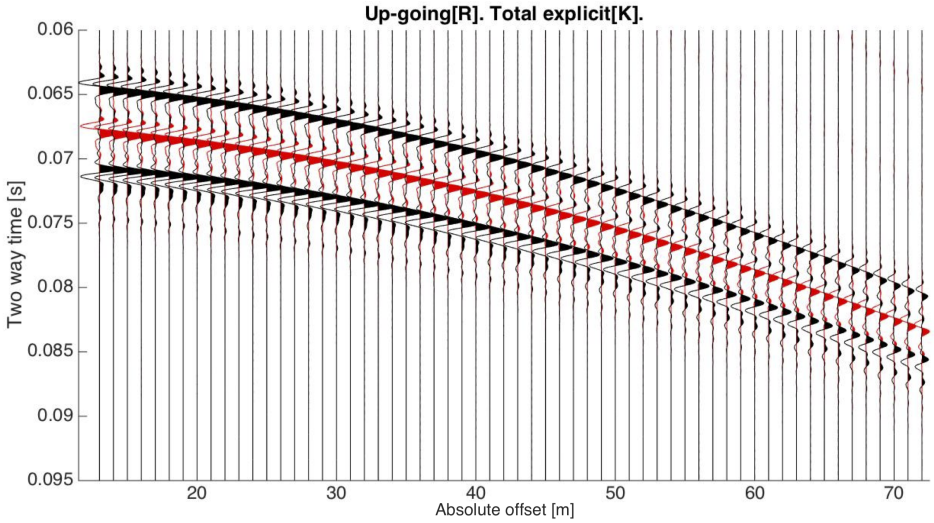

(a)

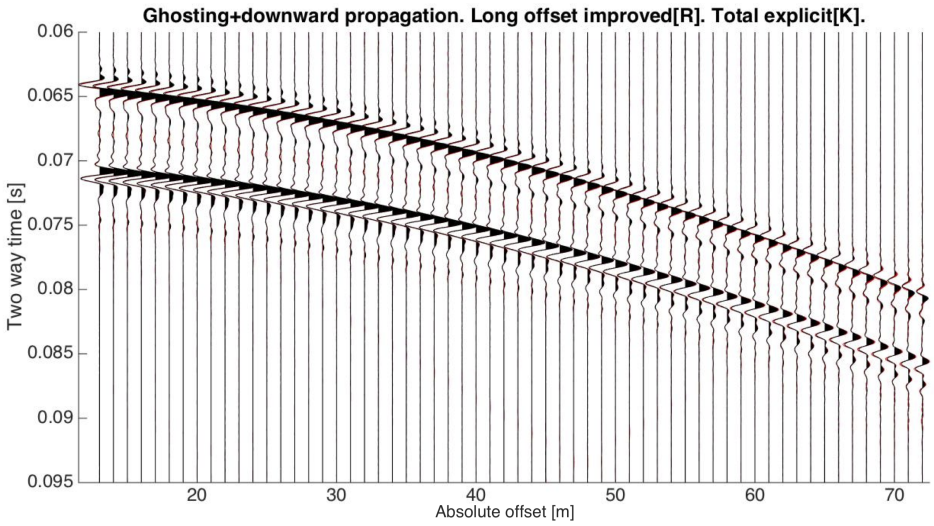

(b)

Figure 2.6: $f - \kappa$ **Ghost prediction.** In panel a) comparison between ghost-free data (red) and the benchmark data from Fig. 2.4b (black). In panel b) the comparison after ghost prediction and traveltime correction in the plane wave domain.

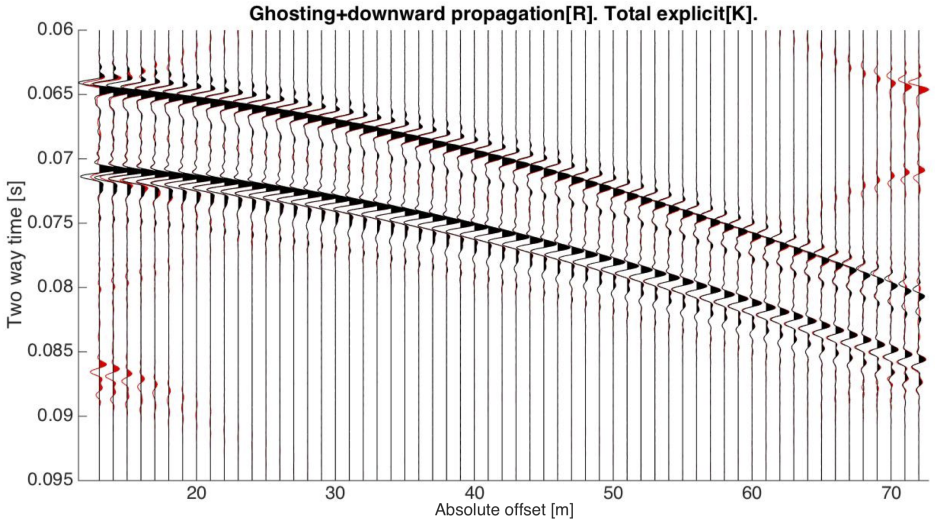

(a)

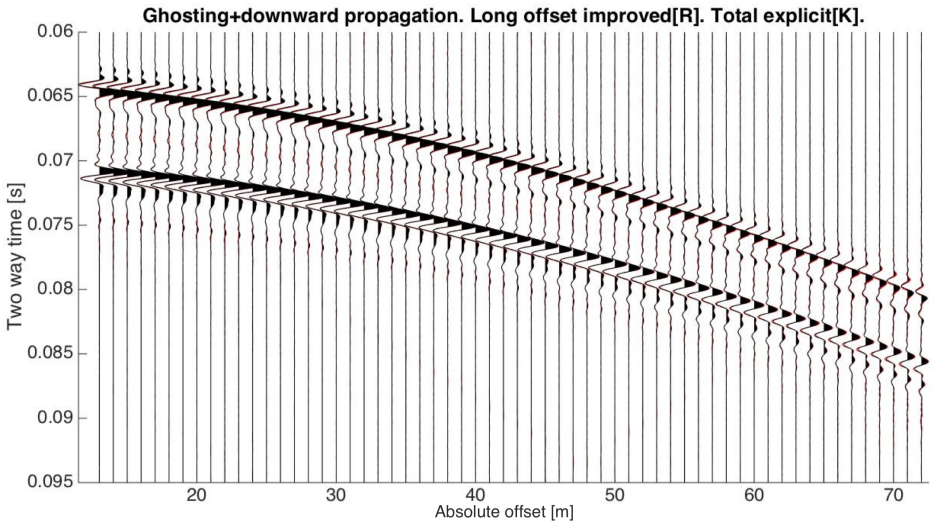

(b)

Figure 2.7: **Effect of spatial domain expansion and trace padding**. In panel a) the result of ghost prediction when no trace-padding is applied. In panel b) a perfect match is obtained with the benchmark data from Fig. 2.4b (black) after trace padding and slowness band increase.

The increased maximum slowness in the final total wavefield can produce aliasing if the spatial sampling rate is not increased accordingly. This is particularly evident when, keeping the streamer length constant, the water depth is reduced. In a test conducted in a 20m water depth model, halving the spatial sampling interval produces dramatic improvements on the quality of the final seismic matrix (Fig 2.8). However, in this shallow water case, the variation of receiver depth from the free-surface to 5 m produces a higher increase of reflection angle, and the spatial domain of the starting seismic data needs to be expanded accordingly. In this case, a perfect match between the predicted and the benchmark data is obtained by doubling the maximum offset of the no-free surface data. This has also the effect of improving the wavenumber resolution, which further enhances the performance of the ghost prediction in the asymptotic region of the reflection hyperbola. The AVO characteristics have been checked against the predicted PP reflection coefficient (Aki and Richards, 2002) and have shown to outperform the explicit modelling, which suffer for the frequency-angle dependency the source ghost, absent in the non-free surface synthetics.

For the sake of completeness, an example of inverse filtering of the ghosted gather to get back to the purely up-going wavefield is here also shown (Aytun, 1999) (Fig. 2.9). Despite the effective receiver ghost removal, artefacts are present in the de-ghosted gather, due to the inherent diverging nature of this inverse filter. Also, such a de-ghosting procedure is not easily applied in the general multi-depth case.

Although this simple constant-depth test does not show any saving in terms of computational time with respect to an explicit modelling (being actually slower), it gives a strong conceptual framework to be aware of when applying the method to a real data. In a realistic application, where the filter parameters vary over the offset domain, the operations outlined in this section need to be performed for each channel, employing accurate estimates of receiver depth and reflection coefficient. The final seismic gather is ultimately generated by selecting the appropriate traces and merging of the different offsets.

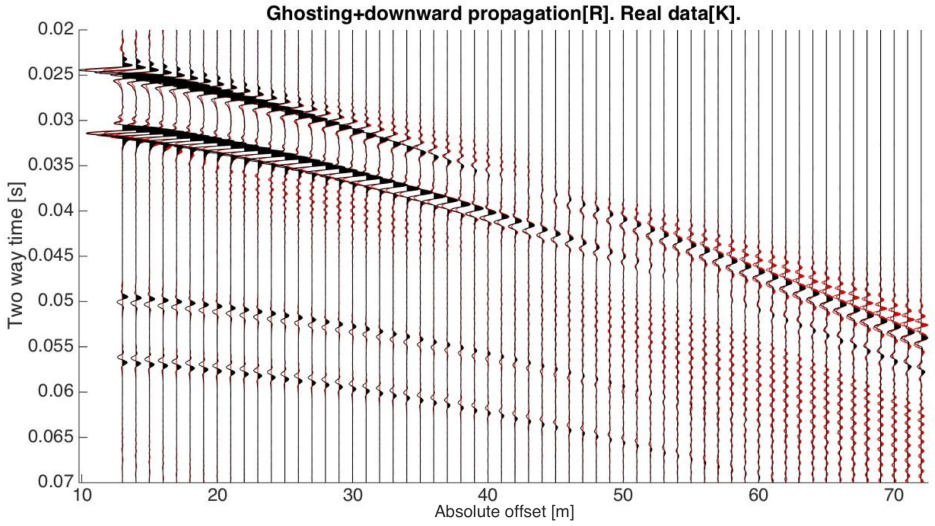

(a)

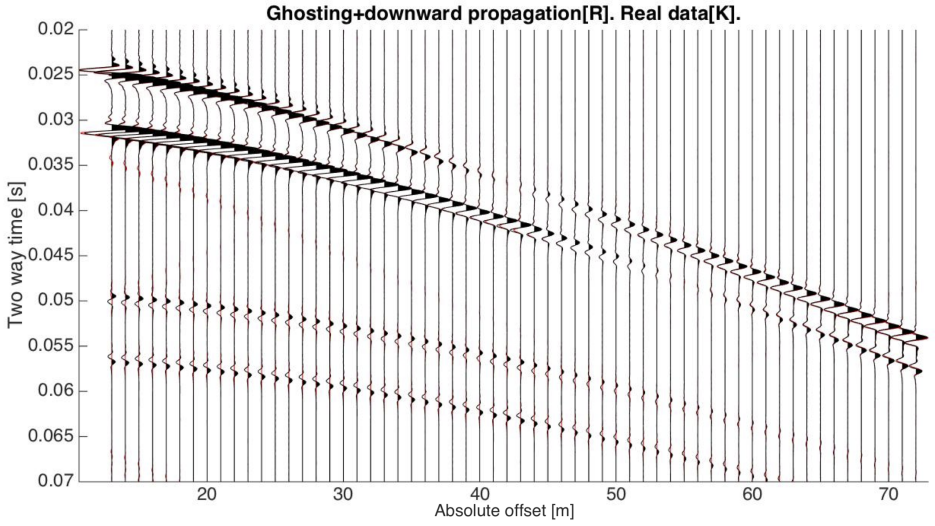

(b)

Figure 2.8: **Wider angle case**. Panel a): No resampling in TX domain. Panel b): the spatial sampling rate of the starting ghost-free matrix is doubled and the aliasing is reduced in the final matrix, even when the data are resampled with a 1 m receiver spacing. Also, the spatial domain has been extended up to twice as many traces as the benchmark seismograms, to make up for the wider reflection angle and improve the wavenumber resolution in the high slowness region.

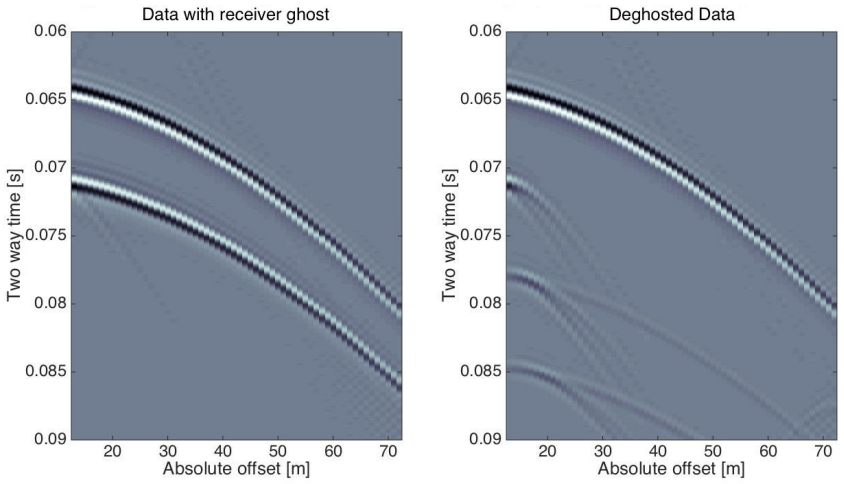

(a)

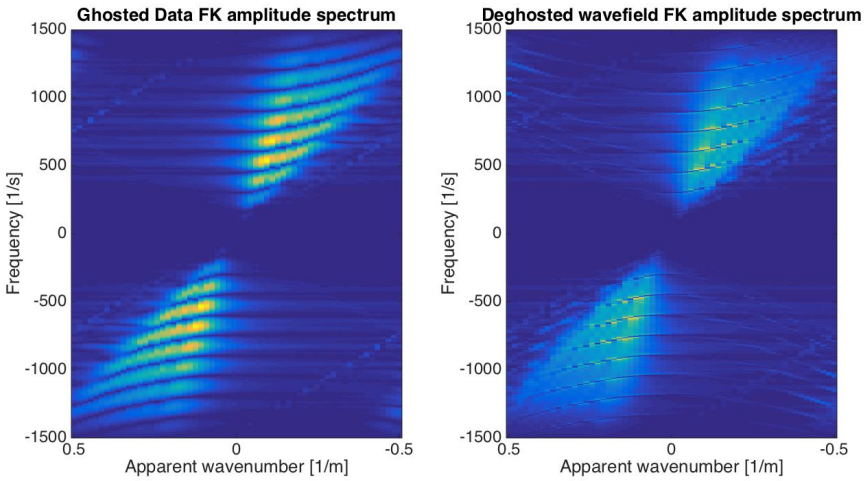

(b)

Figure 2.9: **De-ghosting in fk domain, constant depth**. Panel a) Time domain. Panel b) frequency-wavenumber domain. Note the periodic artefacts in the time domain.

2.3.2 Prediction of receiver depth and sea-surface reflection coefficient

In general, the filter parameters h and r_0 in Eq. 2.18 are not known in advance with the accuracy required by UHF seismic modelling, and need to be estimated from the data. The receiver ghost loci in the frequency-offset $(f-x)$ domain are a function of the receiver depth:

$$fn_{(x_i)} = n\frac{V_w}{2h_{x_i}\cos(\theta(i))} \tag{2.27}$$

where n indicates the order of the harmonic, V_w is the water layer velocity and θ is the reflection angle from the sea-floor, which can be approximated as the ratio between the traveltimes (Pinson, 2009):

$$\theta = (t_0/t_i) \tag{2.28}$$

provided that t_0 corresponds to a near-vertical reflection.

Eq. 2.27 establishes a linear relationship between receiver-ghost null-frequencies and the reciprocal of the receiver depth as a function of offset. The estimation of the offset-dependent receiver depths can be then cast as a linear inverse problem (Aster et al., 2005); provided that more than one harmonic per offset is available, the problem is over-determined and the linear formulation is convenient to derive robust confidence intervals for the solution (Menke, 1989; Aster et al., 2005).

The reflection coefficient for each channel can be conveniently obtained as the solution of a non linear optimisation problem using deterministic algorithms as simple as the bisection method (Burden and Faires, 1985); the optimal $r_0(x_i)$ maximises the normalised cross-correlation value between the predicted trace and the desired trace at the appropriate offset. Although this step is model-based, it only requires an accurate a-priori estimate of the sea-floor depth as the normalised cross-correlation removes the dependency of the results on the accuracy of the sea-floor reflection AVO, while signal tapering around the sea-floor reflected arrival helps to attenuate the bias due to the inaccuracies of the elastic model.

2.3.3 Example application

A seismic super-gather from Finneidfjord, in northern Norway, has been used to test the method on a real dataset where the receiver's ghost is an evident

feature and shows a move out which suggests a varying streamer depth: the receiver ghost is a separate arrival and the time delay between primary and ghost reflection increases with offset (Fig 2.10).

Pre-stack FWI is not feasible on this data, unless we accurately model both primary and ghost traveltime and wavelet shape. To produce a synthetic seismogram comparable to the real data, a far-field measurement of the high-frequency, wide-band source wavelet has been used in conjunction with a 66-layer 1D P-wave velocity and density profile derived by decimating the Multi Sensor Core Logger (MSCL) data from a proximal piston core (Fig 2.11) down to the tuning thickness for the minimum modelled wavelength.

In the real data, because of the of the shallow towing depth and the strong source directivity, the source ghost can be neglected, so only the receiver ghosts have been included in the impulse response of the acquisition system.

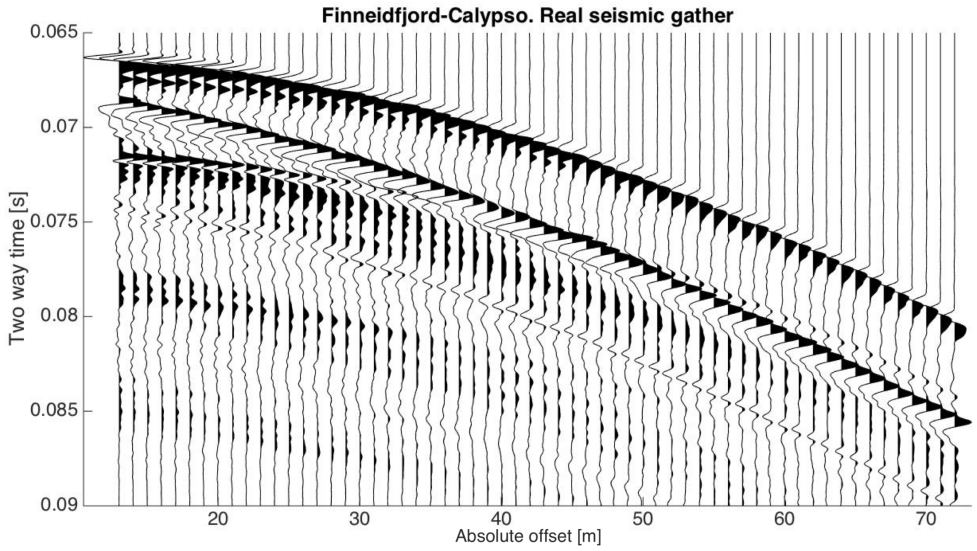

Figure 2.10: **Real data at MSCL core location**. The arrival with the anomalous move out is the receiver ghost. The peculiar traveltime is a consequence of a sagging acquisition geometry in fresh waters, where the buoyancy of the streamer is reduced

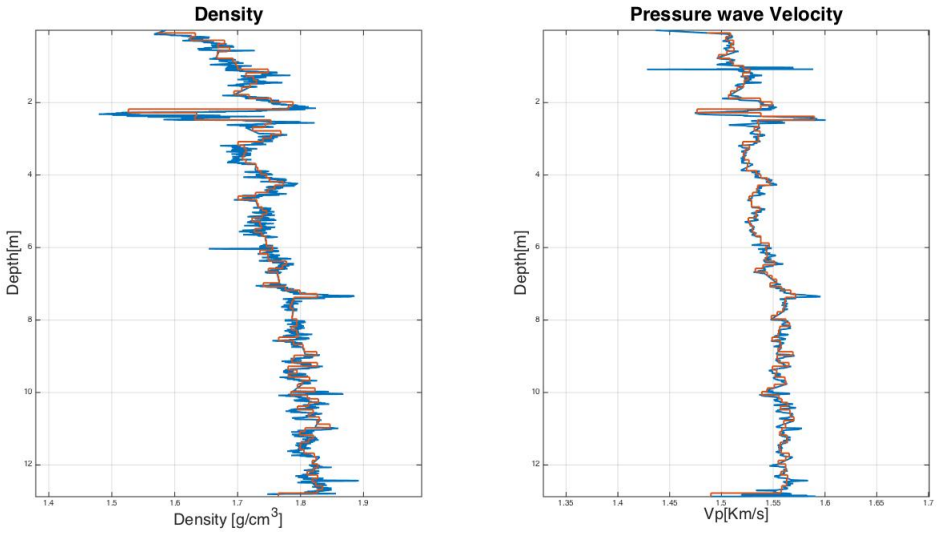

(a)

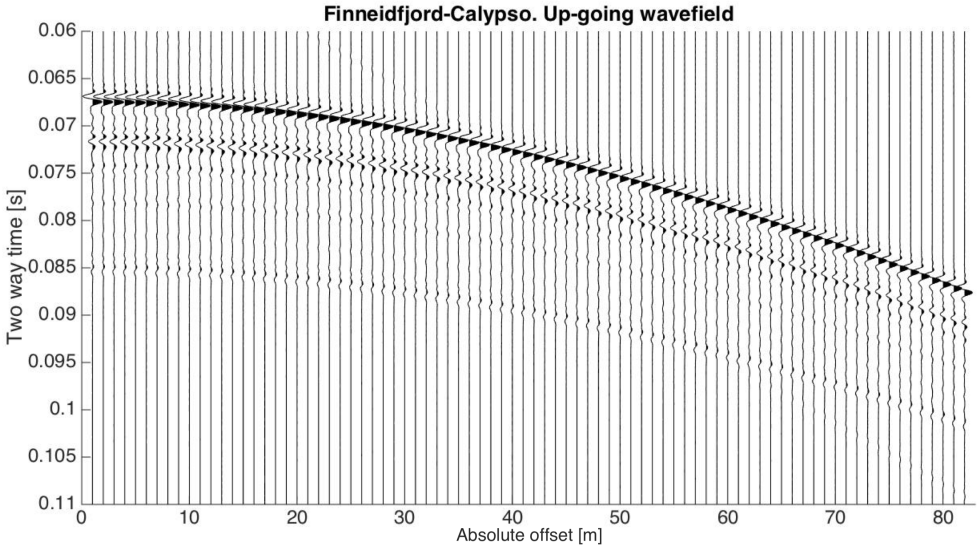

(b)

Figure 2.11: **MSCL log and synthetic data**. Panel a) P-wave velocity and density profile (blue) derived from the piston core *GS-10-163- 02 (Calypso core*) in the location of the super-gather, decimated down to a 20 cm sampling interval (red). Panel b) Synthetic data derived from the MSCL log. No free surface, zero receiver depth.

The ghost prediction in the $f-\kappa$ domain followed a procedure derived from the previous sections:

- Estimation of the receiver depth for each channel in the frequency-offset domain
- Estimation of the local free-surface reflection coefficient for each channel
- Computation of the zero-depth, no-free surface seismic gather on the elastic model derived from a proximal MSCL core log (Fig. 2.11).
- Offset extrapolation and zero-padding
- Generation of one $f-\kappa$ ghosting filter for each channel with the appropriate receiver depth and reflection coefficient. Regularisation and symmetrisation of the matrixes.
- Application of the filter for each receiver depth to the whole gather, back-transformation and offset selection
- Merging of the traces to obtain the new seismic gather.

In order to apply the method to the real dataset, the receiver depth (Δz) for each channel (n) has been estimated using the ghost null frequencies as a function of reflection angle of the sea-floor reflection (Eqs. 2.27 and 2.28). The depth estimation has been cast as a linear inverse problem for the reciprocal of the receiver depths. Four harmonics per channel have been included in the data vector, while the higher ones are used as prediction or validation dataset (Fig 2.12). The uncertainty of the picking as been estimated to translate into a standard deviation of 50 Hz. The problem is well-conditioned and the streamer depth estimate robust, with a narrow 95% confidence interval derived from the diagonal of the posterior model covariance matrix (Menke, 1989; Aster et al., 2005). It's evident in Fig. 2.12 that the data redundancy in the frequency-offset domain is important to constrain the estimated streamer geometry: the higher the number of harmonics per channel used, the narrower the confidence interval of the output value. It is also worth pointing out that the confidence interval becomes systematically broader for higher values of receiver depth; the model is in fact linear for the reciprocal of the depth, hence the uncertainties maps

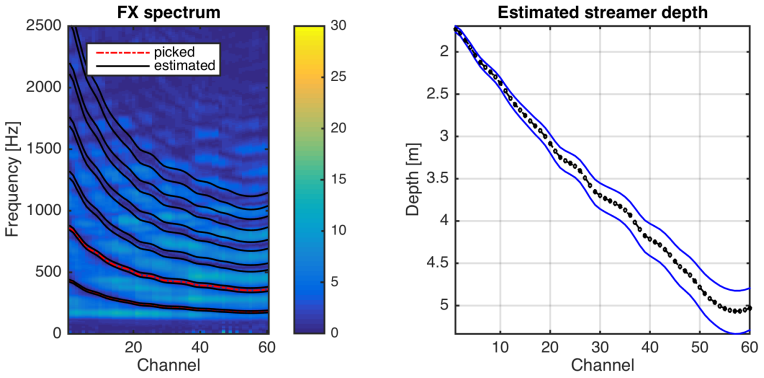

(a)

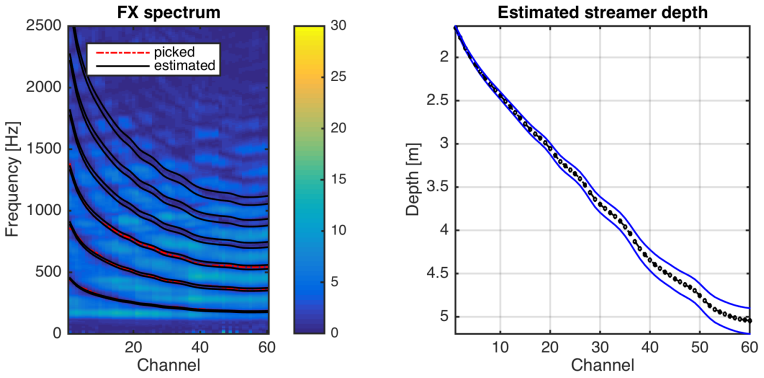

(b)

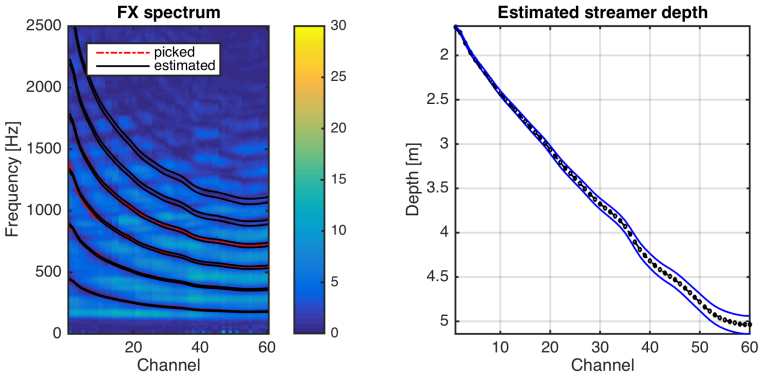

(c)

Figure 2.12: **Receiver depth estimation in the f-x domain**. Inversion of the receiver ghost loci for the receiver depth, varying the number of harmonics used, from panel a to c. Left hand side: frequency-offset amplitude spectrum of the real data; overlaid in red the picked ghost frequencies, in black the predicted ghost null frequencies for the estimated receiver depth. Right hand side: estimated streamer depth (dotted black line) as a function of channel number with 95% confidence interval (solid blue lines).

non linearly (Menke, 1989) in to the spatial domain. The reflection coefficient for each channel has been obtained as the solution of a non linear optimisation problem using the bisection method (Burden and Faires, 1985); the optimal r_0 is the one maximising the normalised cross-correlation value between the predicted trace and the desired trace at the appropriate offset. Using the normalised cross-correlation removes the dependency of the results on the accuracy of the amplitude decay versus offset. The cross-correlation has been performed on the signals tapered around the sea-floor reflected arrival including the ghost, in order to attenuate the bias due to the inaccuracies of the elastic model. Such a process is easily embedded in the $f - \kappa$ ghosting filter generation for each channel.

Before the method is applied to the real dataset, a synthetic explicit total wavefield derived from the core-log has been used as a benchmark, as we did in the tests presented in the previous sections. A perfect match between the synthetic gather with explicit receiver depth modelling and the f-k-predicted synthetic is attained (Fig 2.13). In this case, the proposed method reduces dramatically the computational effort, from 10 minutes to $\sim$1 minute on a standard personal computer, without compromising on the accuracy of the seismic signal.

The obtained seismogram shows also an acceptable degree of match with the real seismic gather (Fig 2.14) both in the time-offset and in the $f - \kappa$ domain, which would be impossible without modelling the receiver ghosts (Fig 2.11, panel b). It is apparent how this will reduce enormously the systematic error in seismic depth imaging or inversion.

Fig. 2.15 shows that introducing the estimated sea-surface reflection coefficient ($r_0(x)$) in the total wavefield calculation further improves the fitness between the computed and the observed seismogram. In this example, this is particularly evident in the nearest 10 channels. The variation of reflection coefficient as a function of offset has a dominant harmonic component with a wavelength in the order of the streamer length, probably reflecting changing in the surface reflectivity due to the sea swell motion.

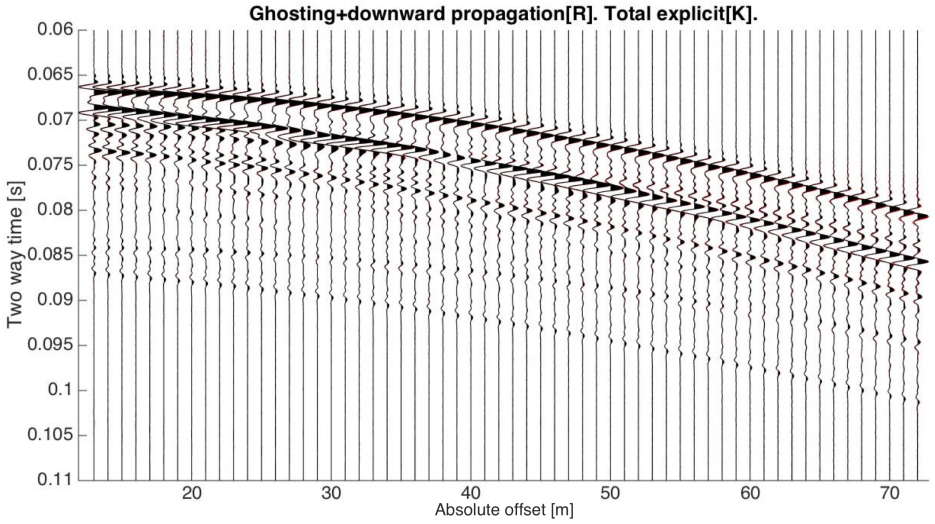

(a)

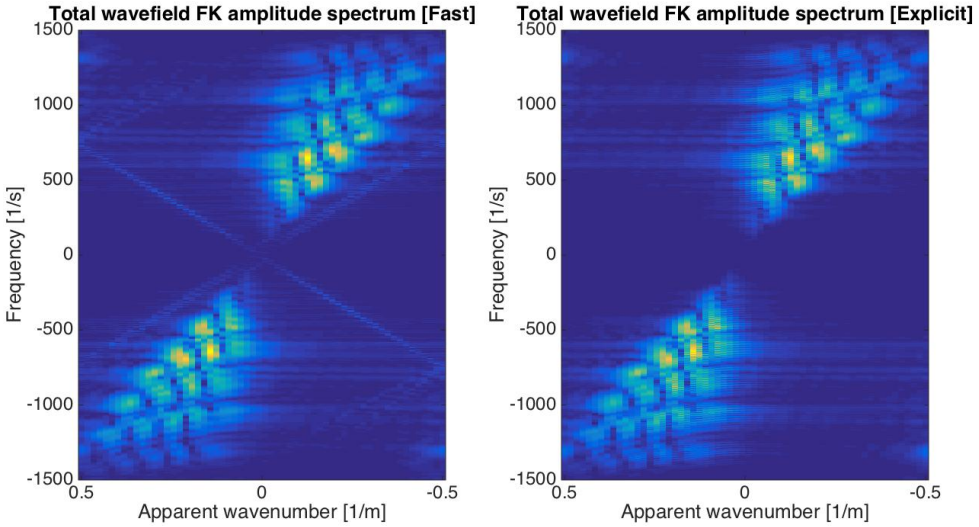

(b)

Figure 2.13: **Benchmarking**. Panel a) comparison of the explicit (black) and fast (red) synthetic total wave fields. Panel b)$f - \kappa$ amplitude spectra.

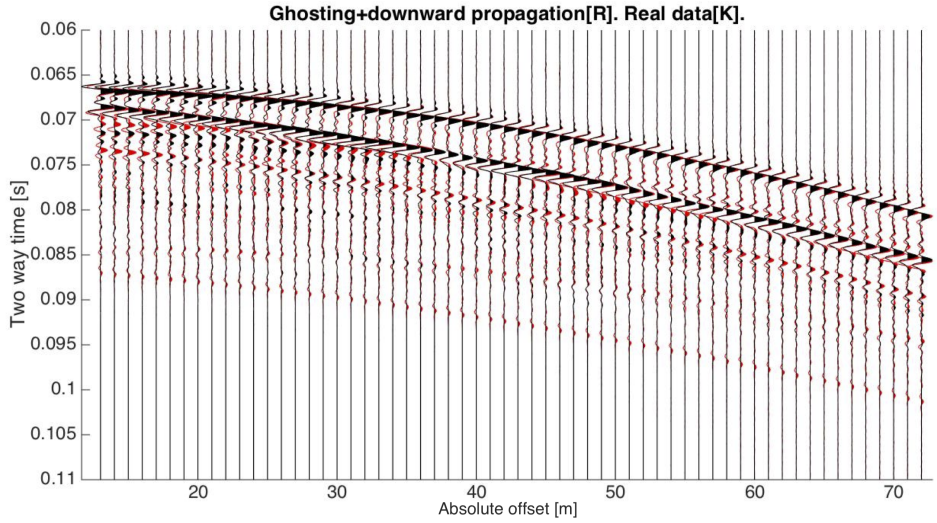

(a)

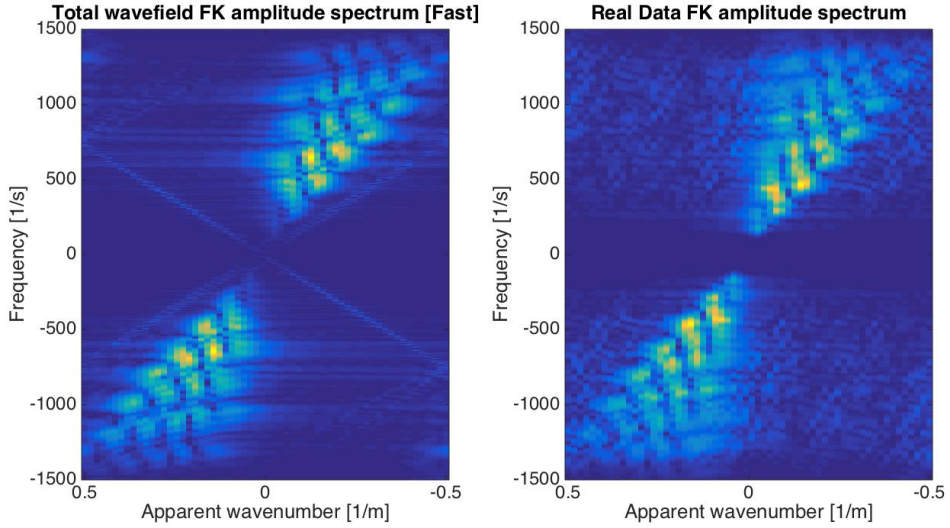

(b)

Figure 2.14: **Real data prediction**. Panel a) comparison of the real (black) and fast (red) synthetic total wave fields. Panel b)$f - \kappa$ amplitude spectra . Note how the systematic error in the seismogram modelling associated with the receiver impulse response is attenuated in a reasonable computing time. The mismatch between real and synthetic can be attributed mostly to inaccuracies in the elastic model and non-coherent noise in the data.

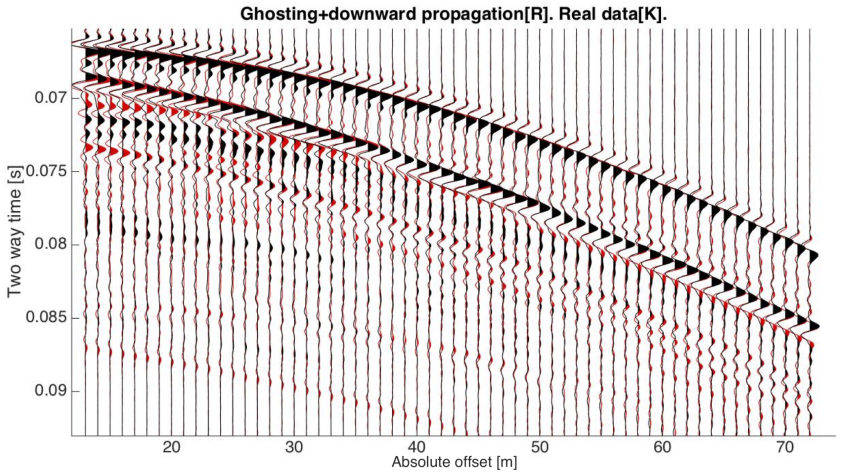

(a)

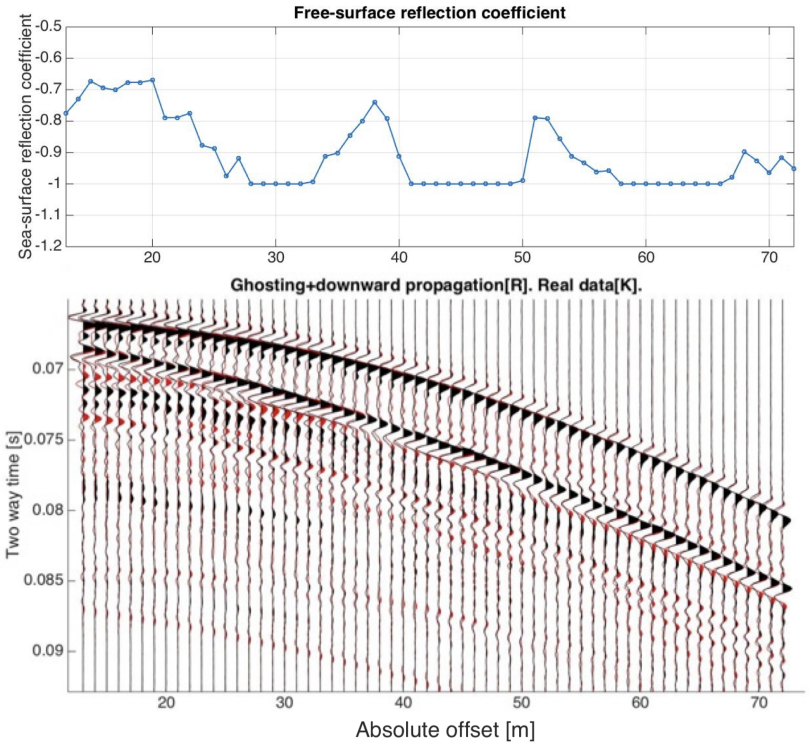

(b)

Figure 2.15: **Optimal reflection coefficient estimate**. Real (black) and fast synthetic (red) seismograms. Panel a) A -1 free-surface reflection coefficient is assumed. Panel b) Optimal reflection coefficient for each channel. Note the significant improvement in the ghost prediction at the shortest offsets.

2.4 Conclusions

In summary, the approach taken in this work for the accurate computation the UHF seismic data involves the solution of the wave equation for a stratified medium and a series of frequency-wavenumber domain signal manipulations:

- Computation of the multi-channel seismogram using the 1D solver.
- Computation of the $f - \kappa$ transform of the seismogram.
- Complex $f-\kappa$ spectra multiplication with both source and receiver transfer functions.
- Downgoing propagation and receiver ghost prediction in the extended $f-\kappa$-channel domain.
- Back-Fourier transformation to the time-offset domain.

This procedure has been developed in order to reproduce the acquisition conditions of near-surface UHF marine seismic reflection data, with accuracy and computing cost adequate for advanced imaging and inversion. The problems of numerical stability, wavenumber resolution and liability to aliasing have been addressed using synthetic data as a benchmark. An example real dataset with strong ghost-contamination and heavily sagging streamer geometry, has been used to demonstrate the efficiency and accuracy of the ghost prediction. Despite an inherent loss of bandwidth associated with including the receiver ghosts in the modelling, this approach avoids non-predictable artefacts arising from pre-stack de-ghosting procedures, which could otherwise seriously jeopardise the inversion results.

3

Pre-stack full waveform inversion of ultra-high-frequency marine seismic reflection data

This chapter has been published as: Provenzano G., Vardy M.E. and Henstock T.J. 2017. Pre-stack full waveform inversion of ultra-high-frequency marine seismic reflection data. **Geophysical Journal International**, 209, 1593-1611. DOI:10.1093/gji/ggx114

Summary

The full waveform inversion (*FWI*) of seismic reflection data aims to reconstruct a detailed physical properties model of the subsurface, fitting both the amplitude and traveltime of the reflections generated at physical discontinuities in the propagation medium. Unlike reservoir-scale seismic exploration, where seismic inversion is a widely adopted remote characterisation tool, ultra high frequency (*UHF*, 0.2-4.0 kHz) multi-channel marine reflection seismology is still most often

limited to a qualitative interpretation of the reflections' architecture. Here we propose an elastic full waveform inversion methodology, custom-tailored for pre-stack UHF marine data in vertically heterogeneous media to obtain a decimetric-scale distribution of P-impedance, density and Poisson's ratio within the shallow sub-seabed sediments. We address the deterministic multi-parameter inversion in a sequential fashion. The complex trace instantaneous phase is first inverted for the P-wave velocity to make-up for the lack of low-frequency in the data and reduce the non-linearity of the problem. This is followed by a short-offset P-impedance optimisation and a further step of full offset range Poisson's ratio inversion. Provided that the seismogram contains wide reflection angles (> 40 *degrees*), we show that it is possible to invert for density and decompose a-posteriori the relative contribution of P-wave velocity and density to the P-impedance. A broad range of synthetic tests is used to prove the potential of the methodology and highlights sensitivity issues specific to UHF seismic. An example application to real data is also presented. In the real case, trace normalisation is applied to minimise the systematic error deriving from an inaccurate source wavelet estimation. The inverted model for the top 15 metres of the sub-seabed agrees with the local lithological information and core-log data. Thus we can obtain a detailed remote characterisation of the shallow sediments using a multi-channel sub-bottom profiler within a reasonable computing cost and with minimal pre-processing. This has the potential to reduce the need of extensive geotechnical coring campaigns.

3.1 Introduction

A quantitative physical model of near-surface marine sediments is of crucial importance in a broad range of environmental and engineering contexts, from the assessment of tsunamigenic landslides hazard and offshore structure stability, to the identification and monitoring of gas storage sites. Currently, marine sediment characterisation is heavily reliant on direct sampling of the seabed, using cores, borehole and/or cone penetrometers (*CPTUs*) (e.g. Stoker et al., 2009; Vanneste et al., 2012) . In this framework, marine seismic reflection data is limited to providing information about the architecture of the stratigraphic discontinuities generating the reflections in the sub-surface, combined with a predominantly qualitative interpretation of the relative amplitude and polarity of the seismic phases. The structural information derived from the sub-bottom profiling can

be correlated to core or borehole logs, where possible, to extend the geotechnical/lithological data from the sampling sites across larger basins. In laterally heterogeneous areas, a large number of direct samples are required to reconstruct the spatial variation of the model to the degree of accuracy required by engineering applications and such an approach is expensive and time-consuming. The reliability of a quantitative estimation of sediment properties is also likely to be undermined by the coring process itself, which deforms and mechanically alters the sample, particularly in low-effective stress environments.

Even though computationally demanding, the inversion of *ultra high frequency (0.2-4.0kHz, UHF)* seismic reflection data potentially provides a non-destructive, faster and cheaper alternative to characterise the mechanics of the sub-seabed. The quantitative interpretation of pre-stack seismic data is a well-established and widely accepted procedure in industry and basin-scale exploration, in the form of either full waveform inversion (FWI) (Tarantola, 1984) or reflection amplitude versus offset inversion (AVO) (Ruthenford and Williams, 1989). It allows improved imaging of complex structures (Tarantola, 1984; Mora, 1980; Virieux and Operto, 2009), detailed rock physics characterisation of oil and gas reservoir (Ostrander, 1984; Ruthenford and Williams, 1989; Fatti et al., 1994; Mallick and Adhikari, 2015), and enhanced resolution regional geology models (Gulick et al., 2013; Morgan et al., 2013).

Over the last few years, quantitative interpretation techniques have started to be applied also to near-surface seismic data in order to remotely derive decimetric resolution shallow sediment physical properties in terms of reflection coefficient and acoustic quality factor (Bull et al., 1998; Pinson et al., 2008; Vardy et al., 2012; Cevatoglu et al., 2015). Holland and Dettmer (2013) used the angle-dependent reflection amplitude as a function of frequency to derive physical properties layering and gradients within the shallow sediments. Recently, post-stack acoustic inversion has been successfully applied on ultra-high-frequency seismic data (Vardy, 2015) to derive quantitative sediment properties from the acoustic impedance.

The dependency of a pre-stack seismic gather on the elastic properties of the propagation medium theoretically allows us to obtain a detailed distribution of compressibility, shear properties and density to the scale of a fraction of the propagated wavelength. Although such properties can be retrieved through

the inversion of the reflections' AVO, a full waveform approach has the advantage to account for all the wave phenomena (Tarantola, 1984, 1986; Fichtner, 2011), within the required resolution and modelling approximation. By exploiting the information contained in the complete waveform, FWI outperforms AVO inversion in most realistic reservoir geophysics application (Mallick and Adhikari, 2015), especially when complicated layer interference and velocity gradients are present (Xu et al., 1993; Igel et al., 1996), which is likely to be a factor in UHF near-surface seismic data.

Here we invert the full waveform of UHF marine data in order to obtain a sub-metric resolution elastic model of the near-seabed. Tests on both synthetic and real pre-stack data, demonstrate the capability of the method to obtain a detailed characterisation of the medium in terms of independent estimates of P-wave velocity, density and Poisson's ratio.

3.2 Methodology and synthetic examples

3.2.1 Full marine seismogram modelling in the varying streamer depth case

The inversion of pre-stack marine seismic data is often addressed within the acoustic approximation to obtain a detailed pressure wave velocity model (Fichtner, 2011; Virieux and Operto, 2009; Tarantola, 1984). Although this approach is widely employed in both industry and academia as an effective tool to improve the quality of the seismic imaging (Morgan et al., 2013), acoustic waveform inversion fails to reproduce an accurate model of the subsurface when shear properties vary in the subsurface, or density is not correlated to P-impedance variations, creating significant amplitude and phase versus offset effects (Mallick and Adhikari, 2015; Silverton et al., 2015). The acoustic approximation is usually justified by the unaffordable computational cost of the finite-differences or finite elements modelling in laterally varying elastic media.

In this paper we account for the elastic properties, assuming that the medium's heterogeneity can be realistically approximated as purely vertical in the range of the imaging aperture (Virieux and Operto, 2009); in UHF seismic, this would be in the order of tens of metres. Despite an inherent loss of horizontal resolution,

such an assumption is acceptable in shallow, recent and weakly tectonised sediments, and allows for the forward model to be computed using an analytic fast solution in the plane wave domain within a reasonable computational cost (Fuchs and Müller, 1971). The program chosen to compute the pressure seismograms is the *Ocean Acoustics and Seismic Exploration Synthesis* from *MIT* (Schmidt and Jensen, 1985; Schmidt and Tango, 1986.), which addresses the reflectivity modelling in an efficient and accurate way for the frequency-wavenumber range of interest.

In UHF marine reflection seismic data, receiver depths in the order of a few metres produce receiver ghost reflections that correspond to frequency notches inside the bandwidth of the signal. Significantly sagging streamer geometries are often observed in the marine-lacustrine setting typical of UHF seismic (Pinson, 2009) and this sub-metric to metric scale variations of the streamer geometry as a function of offset cause non-negligible changes in the source-acquisition system impulse-response. Furthermore, the sea-surface topography approaches the seismic wavelength of a UHF wavefield, causing the sea-surface reflection coefficient to change significantly across the streamer length. In this work we chose to include these factors in the computation of the synthetic seismograms, as opposed to a deconvolution on the observed data. Although inverse ghost filtering would yield a spectral whitening that can be beneficial to the seismic resolution, it is liable to create artefacts inside the bandwidth of the signal which could severely undermine the inversion performance. On the other hand, an explicit full wavefield modelling using the one-dimensional solver would require one forward computation per each receiver offset-depth couple in the appropriate wavenumber bandwidth; since the wavenumber ranges necessary to model each offset are largely overlapping, this approach is clearly inefficient and results in a non-affordable computing cost. In this work, we developed an efficient total seismogram modelling method, which requires only the computation of the pure up-going wavefield at one arbitrary receiver depth, and derives the whole gather in the frequency-wavenumber domain using wavefield decomposition (Verschur et al., 1992; Aytun, 1999). For each channel, the prediction of the down-going wavefield and the downward propagation in the plane wave domain are implemented as a linear filter with the estimated receiver depth and sea-surface reflection coefficient; an inverse two-dimensional Fourier transform gives a seismic gather in an expanded offset range from which the trace at the appropriate offset is selected. The final predicted seismogram

is then obtained by merging the different offsets. The alternative proposed here allowed for a reduction of the computing time of one order of magnitude. Details on the theory and the implementation of the method are given in *Appendix 3.A*. See also **Chapter 2**.

3.2.2 Gauss-Newton seismic inversion

FWI is a non-linear and ill-posed parameter estimation technique, which iteratively updates the earth model $\mathbf{m}$ by minimising a weighted measure of the difference between the computed and recorded seismic data $\delta\mathbf{d}(\mathbf{m})$ (Tarantola, 1984; Virieux and Operto, 2009; Fichtner, 2011). The objective or misfit functional accounts for the amplitude and phase characteristics of the wavefield, either as in the full seismogram, or extracted as pre-stack attributes (Fichtner, 2011; Jimenez-Tejero et al., 2015) and it is regularised in order to penalise physically non-meaningful solutions (Menke, 1989; Asnaashari et al., 2012). The least square regularised objective function reads:

$$e(\mathbf{m}) = \delta\mathbf{d}^T\mathbf{W_d}^T\mathbf{W_d}\delta\mathbf{d} + \delta\mathbf{m}^T\mathbf{W_m}^T\mathbf{W_m}\delta\mathbf{m} \tag{3.1}$$

where $\mathbf{W_d}$ and $\mathbf{W_m}$ are respectively the data and model covariance matrix and $\delta\mathbf{m}$ is measured with respect to a reference model.

At each iteration, the current model $\mathbf{m}_i$ is updated in the direction of the negative gradient of the misfit functional, scaled and weighted by the inverse *Hessian* matrix $\mathbf{H}$:

$$\mathbf{m}_{i+1} = \mathbf{m}_i - \mathbf{H}(\mathbf{m}_i)^{-1}\nabla e(\mathbf{m_i}) \tag{3.2}$$

The ascent direction ∇e is the scalar product between the wavefield partial derivative matrix (*Jacobian* or *sensitivity* matrix $\mathbf{J}$), and the data residual vector $\delta\mathbf{d}$; $\mathbf{H}$ contains the zero-lag autocorrelation of the sensitivity matrix, plus a second order term depending upon the partial second derivatives of the wavefield with respect to each model parameter (Virieux and Operto, 2009).

In three-dimensional FWI, the number of independent model parameters makes the computation of the partial derivative wavefield most often unaffordable. To overcome this limitation, the model update direction is efficiently computed using the adjoint state method (Lailly, 1983; Tarantola, 1984; Virieux and Operto, 2009), whereas the inverse Hessian in equation 3.2 can be replaced by a

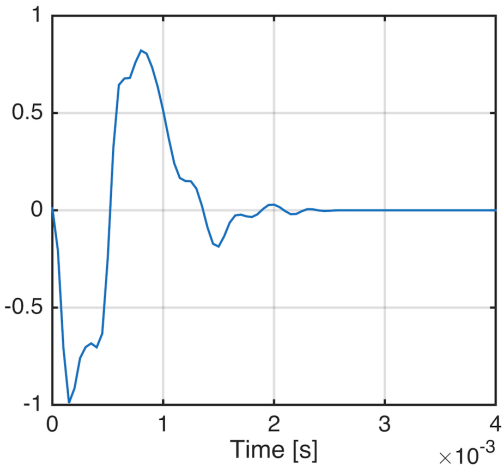

(a)

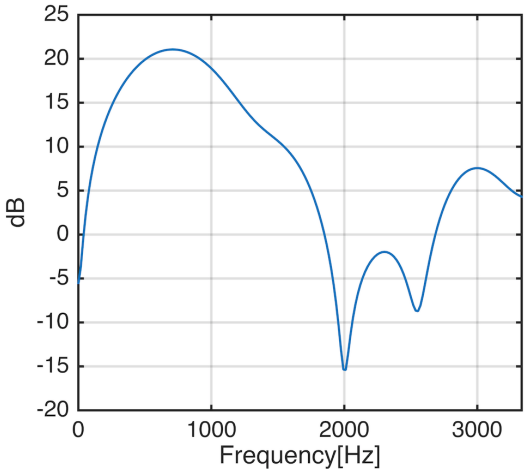

(b)

Figure 3.1: **UHF source signature**: Boomer source wavelet. a) Time domain source signature. b) Power spectrum in deciBel

line-search estimate of the optimal step-length, which ensures the convergence towards the nearest local minimum (Nocedal and Wright, 2006; Virieux and Operto, 2009). However, such a steepest descent implementation does not account for the scaling and uncoupling effect of the inverse Hessian (Virieux and Operto, 2009; Operto et al., 2013) and a robust estimate of the latter in fact significantly improves parameter resolution and convergence speed (Pratt et al., 1998; Operto et al., 2013). Quasi-newton methods, such as the lBFGS (Malinkowski et al., 2011; Gholami et al., 2013a; Dagnino et al., 2014), are now a commonplace implementation of Hessian-based FWI, in which the inverse Hessian is recursively estimated from the evolution of the gradient and model update over a number of previous iterations (Nocedal and Wright, 2006; Virieux and Operto, 2009). Sheen et al. (2006) and Shin et al. (2001), on the other hand, propose to reduce the computational burden of the partial derivative wavefield by exploiting the source-receiver reciprocity.

In this paper, the waveform inversion is implemented as a damped least square Gauss-Newton optimisation problem (Menke, 1989; Aster et al., 2005). In the Gauss-Newton method, a locally linear misfit functional is assumed (Kormendi and Dietrich, 1991; Menke, 1989; Aster et al., 2005), which allows the second order term of the Hessian to be dropped (Virieux and Operto, 2009). We obtain explicitly the sensitivity matrix $\mathbf{J}$ by perturbing each model parameter at each layer depth; the resulting partial derivative wavefield is propagated from the secondary virtual sources to the receivers' position (Rodi, 1976; Sheen et al., 2006; Operto et al., 2013). The effectiveness of this approach in scaling and weighting the gradient is higher than the steepest-descent and quasi-Newton methods, because the approximate Hessian $\mathbf{J}^T\mathbf{J}$ is computed rather than statistically estimated. The relatively low number of unknowns of the 1D modelling makes the computing cost affordable, with wide scope for improvement thanks to the highly parallelisable nature of the sensitivity matrix. The Gauss-Newton method can be applied to trace-normalised seismic data (Lee and Kim, 2003), in which the non-physical phase correction resulting as a by-product of the source deconvolution makes the back-propagation of the adjoint-field inappropriate (Virieux and Operto, 2009). Also, the presence of strong receiver ghost reflections in UHF data undermines the accuracy of the reverse time migration of the residuals (Sun et al., 2015). The model update $\delta\mathbf{m}$ at each iteration can therefore be expressed

as:

$$\delta\mathbf{m} = (\mathbf{J}^T\mathbf{W_d}\mathbf{J} + \mathbf{W_m})^{-1}\mathbf{J}^T\mathbf{W_d}\delta\mathbf{d} \tag{3.3}$$

The first factor of the right hand side of Eq. 3.3 is the regularised approximate Hessian, while the second is the gradient of the misfit functional. Eq. 3.3 has the form of the regularised least square inverse solution for a problem of the kind:

$$\delta\mathbf{d} = \mathbf{J}\delta\mathbf{m} \tag{3.4}$$

It is therefore possible to express the linear operator $\mathbf{J}$ mapping the data residual $\delta\mathbf{d}$ from the data space into the model update $\delta\mathbf{m}$ space in the *Singular Value Decomposed (SVD)* domain. If, for the sake of simplicity, we set the data covariance matrixes equal to the identity and scale the model covariance by the factor α, Eq. 3.3 takes the form (Aster et al., 2005):

$$\delta\mathbf{m} = \sum_{i=1}^{k} \frac{{s_i}^2}{{s_i}^2 + \alpha^2} \frac{{\mathbf{U}_{(:,i)}}^T \delta\mathbf{d}}{s_i} \mathbf{p}^T\mathbf{V}_{(:,i)} \tag{3.5}$$

where $\mathbf{U}$ is the data eigenvector matrix, s_i is the i_{th} singular value and $\mathbf{V}$ is the model eigenvector matrix. This equation expresses the model update vector as the result of the projection of the data residual vector on the model update vectorial space. The hyper parameter α contributes in the filter factor $\frac{{s_i}^2}{{s_i}^2+\alpha^2}$ to damp out the small singular value responsible for numerical instability (Menke, 1989; Aster et al., 2005; Asnaashari et al., 2012). The preconditioning vector $\mathbf{p}$ assigns a different relative weight to each parameter of the sensitivity matrix in order to guide the inversion towards geologically plausible solutions.

From a physical point of view, Eq. 3.4 is equivalent to the *Born approximation* of the wavefield (Jannane, 1989; Virieux and Operto, 2009; Fichtner, 2011), which implies that the data residuals are linearly related to missing heterogeneities in a background elastic model (Tarantola, 1984; Jannane, 1989; Virieux and Operto, 2009; Fichtner, 2011). In this framework, in order for the convergence to local minima to be prevented, the background velocity distribution needs to account for the traveltime information of the data within half a propagated wavelength, otherwise *cycle skipping* (Virieux and Operto, 2009) occurs and a spurious solution is obtained. Resuming, the inversion process involves the following steps:

1. Computation of the seismogram for the current model $\mathbf{m}_i$;

2. Computation of the residual vector $\delta\mathbf{d}$;

3. Computation of the sensitivity matrix by perturbing each model parameter and computing the residuals in a forward finite difference scheme;

4. Singular value decomposition and generalised inverse computation;

5. Computation of the model update $\delta\mathbf{m}$ and of the model $\mathbf{m}_{(i+1)}$;

6. Seismogram computation for the $\mathbf{m}_{(i+1)}$ model;

7. Misfit computation;

8. If the convergence criteria are satisfied, the inversion ends, otherwise goes back to 2.

The process stops when a maximum number of iteration is reached, the misfit goes below a threshold, or the misfit evolution function has reached a *plateau*.

3.2.3 A strategy for the multi-parameter problem

An isotropic and elastic medium is univocally described by a spatial distribution of three independent parameters (Aki and Richards, 2002), most commonly density and the *Lamè* coefficients (Tarantola, 1986); although equivalent in a forward modelling sense, different parametrisations have different convergence properties and parameters' resolution. The most desirable parametrisation guarantees the minimum crosstalk among the unknowns of the inversion (Tarantola, 1986; Kormendi and Dietrich, 1991); ideally, the partial derivative wavefield of one parameter should be uncorrelated with the residual wavefield produced by each other independent parameter (Tarantola, 1986; Operto et al., 2013). In marine reflection seismic data, the presence of only one propagation mode impedes the opportunity to obtain independent estimates of P-wave (Vp) and S-wave velocity (Vs) (Jin et al., 1992; Igel et al., 1996); on the other hand, density is strongly coupled with P-wave velocity at narrow reflection angle; the two parameters can't be effectively resolved and in fact yield a posterior reconstruction of the P-impedance model (Tarantola, 1986; Operto et al., 2013). Here we choose to parametrise the reflectivity of the earth model as a distribution of P-impedance,

Poisson's ratio and density (Debski and Tarantola, 1995; Igel et al., 1996), superimposed to a long-wavelength P-wave velocity model that controls the wavefield kinematic (Tarantola, 1986; Jannane, 1989).

The limited offset, limited bandwidth, lack of diving waves and multi-component data of UHF data produce a highly hierarchical dependancy on the multi-parameter space as a function of the reflection angle range (Tarantola, 1986). P-impedance is the dominant parameter over the whole angle range, and it is sufficient to explain the reflected energy at near-zero reflection angle (Tarantola, 1986). A second order contribution to the wavefield energy is given by the variation of the reflection amplitude with angle; this depends upon the Poisson's ratio and density contrast at the layer interfaces, the first dominating the mid offset AVO, the latter having an increasing importance at greater reflection angles (Koefoed, 1955; Ostrander, 1984; Ruthenford and Williams, 1989; Mallick and Dutta, 2002). The resulting Hessian matrix for a scatterer layer is highly rank-deficient, meaning that only one parameter class can be effectively inverted for in a simultaneous multi-parameter inversion (Operto et al., 2013); despite the inherent stability of the SVD approach, this makes the multiplication by the inverse Hessian not ideal as a means to uncouple the different components of the gradient. On the other hand, the angle dependancy of the secondary virtual sources for the chosen parametrisation, allows us to orthogonalise the problem by appropriately weighting the residual wavefield and inverting sequentially each independent parameter, from the strongest to the weakest contributor to the residual energy (Tarantola, 1986; Igel et al., 1996; Operto et al., 2013). This approach has also the advantage of a simpler implementation of the regularised least-square inversion, as it does not require to build a model covariance matrix that balances the contribution of parameters with different weights (Eq. 3.3).

We first invert for P-wave velocity by keeping Poisson's ratio and density constant to the background values, windowing the data and the partial derivative field around the near-offsets; this is equivalent to a P-impedance inversion, for density is kept constant. We then invert the whole offset range for Poisson's ratio; the virtual source radiation patterns of Poisson's ratio and density are partially overlapping in the mid reflection angle range, hence the estimate will be to some extent affected by crosstalk. If wide reflection angles (> 40 degrees) are available in the data, the relative contributions of density and P-wave velocity to P-impedance are decomposed by inverting for density at constant P-impedance.

A cyclical update of density and Poisson's ratio in this stage makes up for the effect of crosstalk resulting from the previous stage. The reliability of the *a-posteriori* P-wave velocity estimate is ensured by the broad wavenumber content of the P-impedance model (Operto et al., 2013), as opposed to a *a-posteriori* estimation of density from a [*P-impedance, Vp, Poisson's ratio*] parametrisation.

3.2.4 Test on synthetic UHF marine reflection data

We test the performance of the sequential inversions strategy on a synthetic example of pre-stack UHF data. In this experiment, the starting P-wave velocity model is accurate enough to allow for an effective inversion of the reflectivity of the medium. We also assume that the source wavelet is perfectly known. The synthetic *true* model has 18 layers, for a total thickness of 12 metres below the sea-bottom interface at 15 metres water depth; it includes 20 *cm* thick target horizons with distinct elastic characteristics. Changes in acoustic impedance are either correlated to variation in both density and velocity, or density only, and the Poisson's ratio varies independently with respect to the P-wave velocity, in order to mimic both changes in fluid saturation in the same lithology and lithological stratifications (Ruthenford and Williams, 1989). The perfect elasticity implies that there is no intrinsic attenuation (Aki and Richards, 2002). The theoretical source signature is a minimum phase Boomer wavelet (Fig. 3.1) band-pass filtered *0.1-1.5 kHz* (almost 4 octaves). The acquisition simulates a source depth in the order of 10 centimetres and a 60 channel streamer with a group spacing of 1 meter and a minimum offset equal to 13 metres. The receiver depth is equal to 1.85 metres, which corresponds to receiver ghost notches at multiples of 400 Hz (Aytun, 1999). The *true* data have been contaminated by a band-limited zero-mean gaussian noise, for a *signal-to-noise* ratio equal to 50 with respect to the amplitude of the strongest reflection.

The starting model of the iterative inversion is a low-pass filtered (2 metres cut-off wavelength) version of the true model, containing the correct velocity and density trend, but accounting only for the sea-floor primary reflection traveltime and surface-related multiples. With the exception of the sea-floor, the location of the discontinuities is unknown. The starting model has been parametrised as a stack of 58 homogeneous, elastic and isotropic layers with a thickness chosen to be in the order of the tuning thickness for the frequency band employed and the

expected velocity values ($\lambda/4$). This results in a model space with 174 degrees of freedom, which are broken down to 58 per stage in the sequential inversion.

In *Stage 1* (Fig. 3.2) the data are inverted for P-wave velocity only. An accurate P-impedance profile is retrieved and a good waveform match is attained in the short offsets of the seismic gather. Note how the 20 cm thick low-density bed at 3.4 metres is incorrectly identified by a drop in P-wave velocity, while in layers where P-wave velocity and density are correlated, the P-wave velocity change is overestimated to explain the P-impedance variation. This confirms the considerations about the [*Vp, density, Poisson's ratio*] parametrisation in the reflection regime (Tarantola, 1986; Operto et al., 2013). The Poisson's ratio is kept constant in this stage, so that not only P-wave, but also S-wave velocity is effectively updated.

At *Stage 2* the data are inverted for Poisson's ratio, while the other parameters are kept fixed. The misfit is here dominated by the reflection amplitude versus offset variation. The inversion updates the model in the correct direction, but crosstalk with density prevents from reconstructing the fine-scale details of the shear properties, especially where the relative contribution of P-wave velocity and density to the P-impedance is poorly described (Fig. 3.3).

Stage 3 of the inversion firstly optimises density until an accurate impedance distribution is obtained. At this point, the final parametrisation [*P-impedance, density, Poisson's ratio*] is effectively adopted and density evolves independently from P-impedance; this produces a consequent change in P-wave velocity. Note how the P-impedance contrast at 3.4 metres is now correctly decomposed in its relative P-wave velocity and density contributions. The effect crosstalk between Poisson's ratio and density in the previous stage is also made up for by cyclically updating the two parameters: the effectiveness of this stage is particularly evident in layers where the underestimate of density in the starting model had induced an underestimate of Poisson's ratio (and *vice-versa*). The final model (Fig. 3.4) is a high-fidelity representation of the elastic model.

The robustness of the proposed inversion strategy can be tested against variations of the *signal-to-noise* ratio (*SNR*). Gaussian band-limited noise with zero mean has been added in the signal frequency band to the field data with different SNRs and the normalised *L2* model misfit has been computed per each parameter class. As shown in Fig. 3.5, P-impedance is the most robust parameter to increasing random noise energy in the data; Poisson's ratio is also remarkably robust in

a broad range of SNR, while the results of the P-wave velocity/density decomposition at constant impedance quickly deteriorates with decreasing signal-to-noise ratio. Note how, for signal-to-noise ratio lower than 50, the Poisson's ratio data misfit increases steeply, arguably because of the crosstalk between density and shear properties. The results are consistent with the idea that shear properties and density are second order contributions to the misfit value in marine reflection seismograms (Tarantola, 1984, 1986), hence their effect is more quickly buried in high noise levels. Nevertheless, as we will see in the next section, general conclusions about the robustness of the parameter estimation need to account for the medium characteristics and the acquisition parameters.

3.3 Sensitivity issues specific to UHF data

The elastic full waveform inversion of UHF reflection data suffers from specific factors, which are discussed in detail in this section:

1. The limited reflection angle due to the short streamers normally employed limits the possibility to obtain independent information about P-wave velocity and density.

2. The inversion for the Poisson's ratio distribution is highly non-unique, because the AVO characteristics of the gather are dependent upon the Poisson's ratio contrasts (Aki and Richards, 2002), rather than its absolute value, so that the misfit function is insensitive to shear properties gradients. Furthermore, the high Vp/Vs ratio of the shallow marine sediments (in the order of $10^1 - 10^2$) spans a very narrow Poisson's ratio range (Hamilton, 1970).

3. The sensitivity in the mid to long wavelengths of the P-wave velocity model is poor because of the lack of low-frequencies and the limited available offsets (Mora, 1980; Jannane, 1989).

4. The accuracy of the UHF source wavelet estimation using traditional methodologies is compromised by the characteristics of the data and of the typical reflectivity series involved.

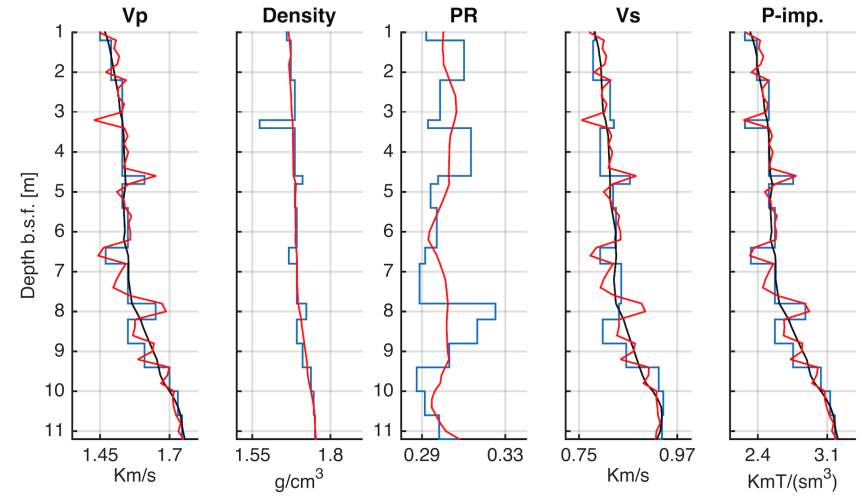

(a)

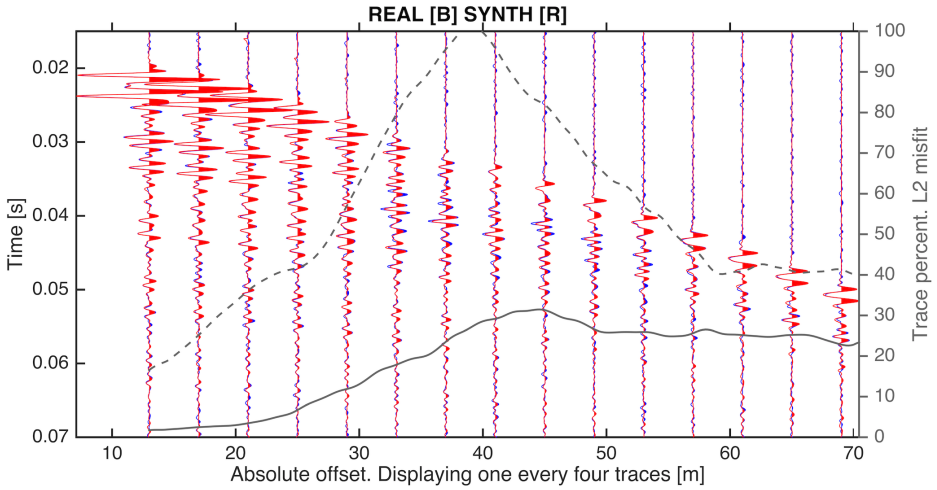

(b)

Figure 3.2: **Stage1, P-wave velocity inversion**. a) Starting model (black), true model (blue), current best model (red). b) Synthetic seismogram (red) overlaid to the "real data" (blue). The solid grey curve represents the trace by trace percentage L2 misfit for the final model, the dashed curve is relative to the model at the beginning of the stage. The Impedance profile is retrieved accurately and a good match is attained in the short offsets of the seismic gather.

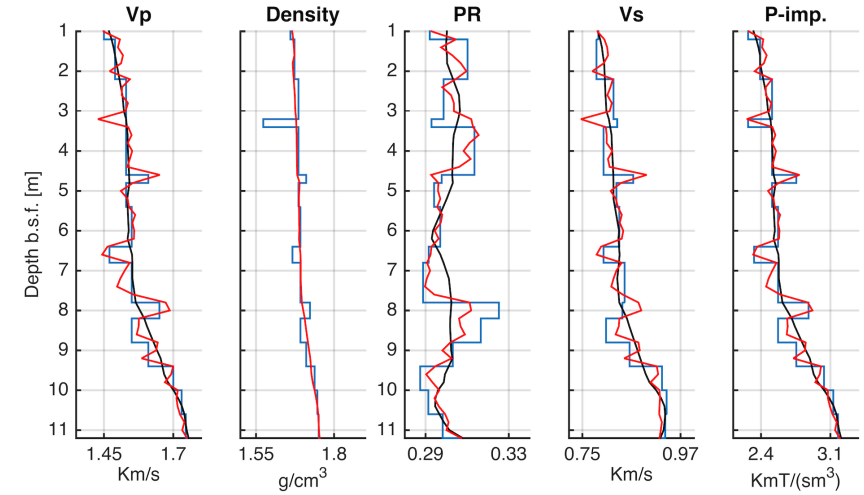

(a)

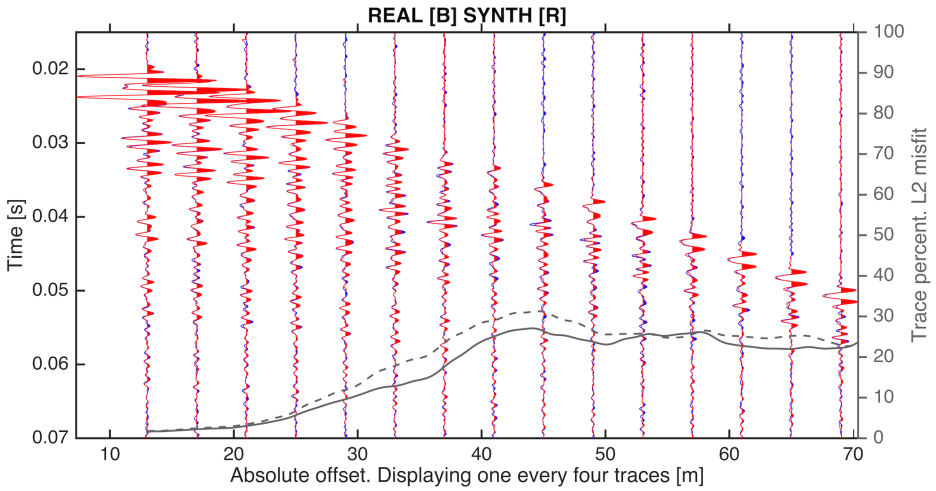

(b)

Figure 3.3: **Stage2, Poisson's ratio inversion**. a) Starting model (black), true model (blue), current best model (red). b) Synthetic seismogram (red) overlaid to the "real data" (blue). The solid grey curve represents the trace by trace percentage L2 misfit for the final model, the dashed curve is relative to the model at the beginning of the stage. In this stage we reduce the data misfit associated to the AVO characteristics of the gather, but the inaccuracies in the starting density model prevent the algorithm from retrieving the shear-properties' fine-scale details.

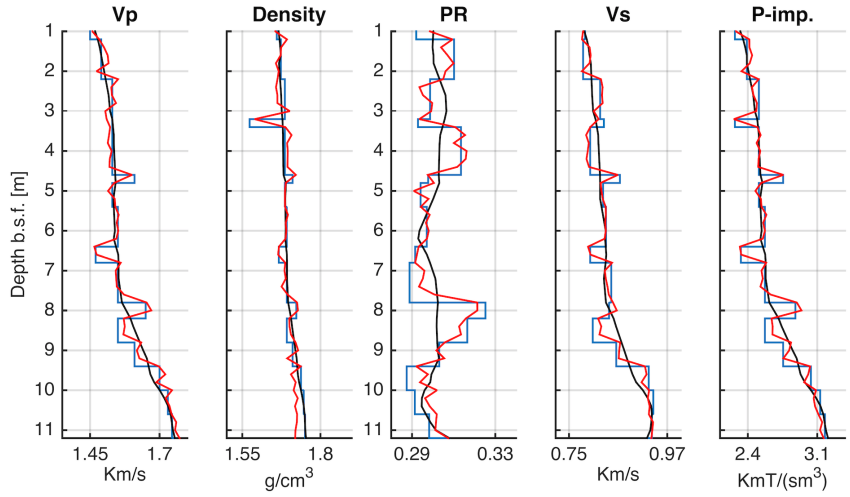

(a)

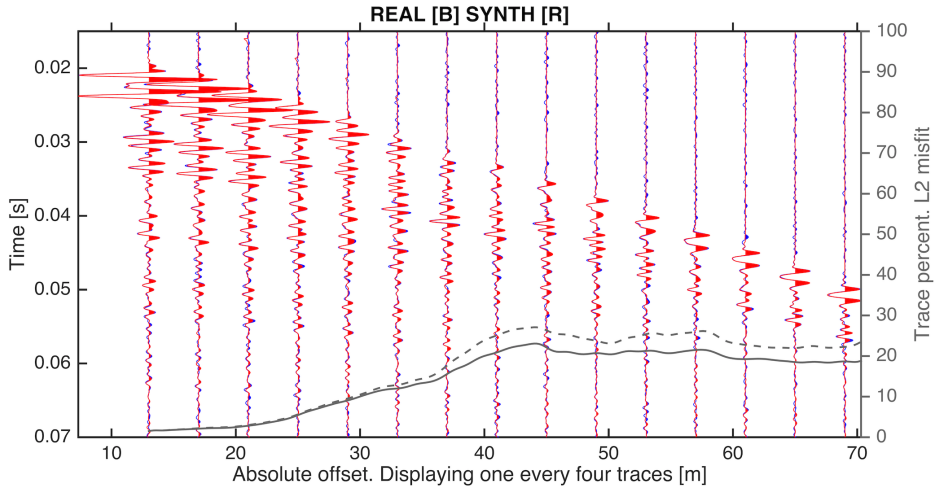

(b)

Figure 3.4: **Stage3, Cyclical density and Poisson's ratio inversion. P-impedance constant**. a) Starting model (black), true model (blue), current best model (red). b) Synthetic seismogram (red) overlaid to the "real data" (blue). The solid grey curve represents the trace by trace percentage L2 misfit for the final model, the dashed curve is relative to the model at the beginning of the stage. In this stage we fit the wide-angle part of the shot gather by optimising cyclically for density and Poisson's ratio. Note how the impedance change right below 3 metres depth is correctly attributed to a density change and the P-wave velocity is changed accordingly to keep the P-impedance constant.

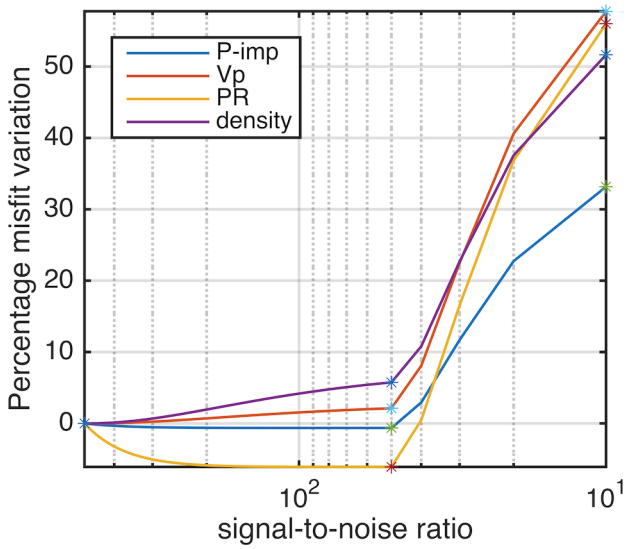

Figure 3.5: **Robustness to random noise**. Model misfit percentage variation for P-impedance, Poisson's ratio, P-wave velocity and density as a function of signal-to-noise ratio (SNR). Note how the acoustic impedance is the most robust parameter, while the Vp/density separation is the most sensitive to the noise energy in a broad SNR range. Interpolated from the computed value (asterisks).

3.3.1 Sensitivity to constant-impedance density variations

A broad literature about the parameter dependancy of marine seismic reflection data shows that independent high frequency variations of P-wave velocity and density at constant impedance are poorly constrained parameters when limited offset are available (e.g. Debski and Tarantola, 1995; Jannane, 1989; Igel et al., 1996). We conduct a sensitivity analysis on a simple homogeneous model with a low impedance 50 cm thick layer, whose density is changed at constant impedance, as a function of the maximum reflection angle at the target. The relative *L2* data misfit is computed against a reference model and the results are plotted in decibel scale in Fig. 3.6a. The rapid decrease in the relative data misfit with decreasing reflection angle suggests that the sensitivity of the inversion to such changes in the subsurface is highly sensitive to the ratio between streamer aperture and target depth. In order to decompose the amplitude and traveltime contribution to the measured misfit, we compute the offset-dependent cross-correlation value and lag; the results show how a density perturbation at constant impedance produces a change in the maximum value of the cross-correlation function (Fig. 3.6b), whilst the lag is not significantly affected, being always equal to or lower than one sample. This results confirm that, although the reflection travel times are insensitive to such perturbations, being mostly controlled by a long-wavelength distribution of the P-wave velocity, density variations at constant impedance do affect the angle-dependent reflectivity of the propagation medium, as a second order contribution to the AVO reflection amplitude (Aki and Richards, 2002). Three density profiles have been picked from the population of models used for the sensitivity analysis to test how this translates into the inversion results. We use a constant starting density model, where the impedance change at the target layer is entirely explained by a P-wave velocity variation, a situation comparable to the end of the second stage of the inversion. The Poisson's ratio profile of the starting model is correct, thereby crosstalk effects do not play a role in the test. The curves computed from the exact AVO equation (Aki and Richards, 2002) for the starting and true models show how the inaccuracy in the density profile at constant impedance contrast produces a residual AVO at long offset, which is greater for the shallower model. The quality of the P-wave velocity/density decomposition in the final models is highly dependent on the reflection angle range (Fig. 3.7) and no independent information about P-wave velocity and

density can be reliably obtained at reflection angles below 30 degrees. Model misfit for each parameter class in the 18 layers model (Fig. 3.8) as a function of a maximum reflection angle shows that P-impedance and Poisson's ratio are robust to changes in the reflection angle; in contrast, the P-wave velocity profile quickly deteriorates as the reflection angle range narrows.

3.3.2 Sensitivity to Poisson's ratio in high Vp/Vs media

Changes in lithology, pore pressure and saturating fluids produce differential variations of compressibility and shear properties, determining changes on the ratio between P-wave and S-wave velocities (Vp/Vs) (Ruthenford and Williams, 1989; Mallick and Dutta, 2002; Igel et al., 1996). However, the Vp/Vs ratio controls the reflectivity of a medium via the Poisson's ratio (Koefoed, 1955; Mavko et al., 2009):

$$\nu = \frac{(V_p/Vs)^2 - 2}{2[(V_p/Vs)^2 - 1]} \tag{3.6}$$

The non linear relationship of Eq. 3.6 determines a range-dependent sensitivity to Vp/Vs changes. For low ν, small changes in the Vp/Vs ratio head to significant variation of ν, thereby creating important AVO effects; in contrast in the range from 0.45 to 0.5, where normally most shallow marine sediments fall (Hamilton, 1970), large changes in Vp/Vs correspond to small variation of Poisson's ratio (Fig. 3.9a), limiting the AVO response (Mallick and Dutta, 2002).

A sensitivity analysis is performed on a simple elastic model with a low-impedance 50 cm thick target layer, whose Vp/Vs ratio is 5 times higher than the surrounding homogeneous medium, simulating the presence of a under-consolidated, high-porosity and high pore-pressure sediment bed. Within a broad range of ν, we introduce perturbations to the S-wave velocity of the target layer and measure the relative $L2$ misfit with respect to a reference model. The sensitivity to Vs perturbations rapidly falls with increasing Poisson's ratio, regardless the amount of perturbation added (Fig. 3.9b). To study how this loss of sensitivity affects the inversion performances, we pick four models from the sensitivity analysis in four different Poisson's ratio ranges and run the inversion starting from a homogeneous profile. Although the Vp/Vs ratio contrast at the target layer boundary is 5 for every model, the corresponding Poisson's ratio variation drops

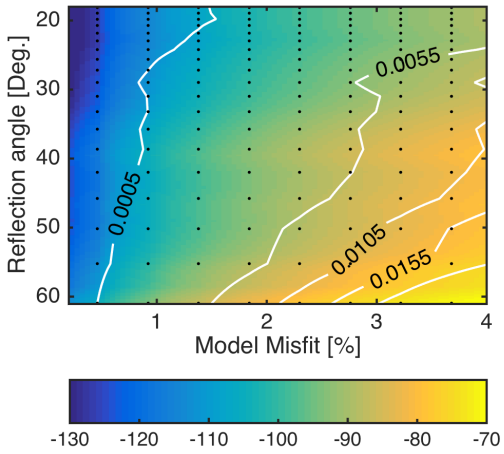

(a)

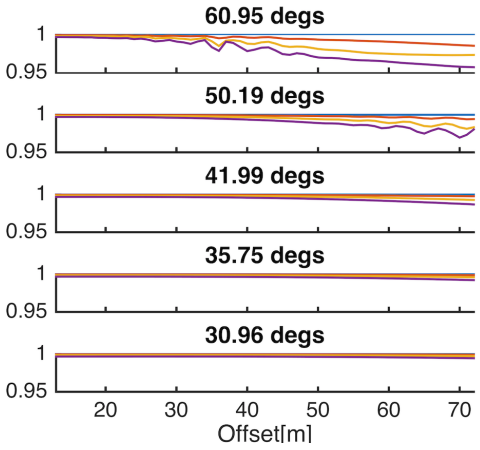

(b)

Figure 3.6: **Constant-impedance density sensitivity analysis**. Per each reflection angle, the *L2* data misfit normalised to the seismogram energy is computed between a reference model and a range of models with increasing percentage perturbation of the target layer density. a) Data misfit normalised to the total data energy in deciBel. The contour plot shows the percentage iso-misfit surface. The black dots correspond to the computed models. b) Maximum cross-correlation value as a function of offset at different maximum reflection angles. The offset-dependent correlation is computed per different perturbation values (increasing from pale blue to magenta).

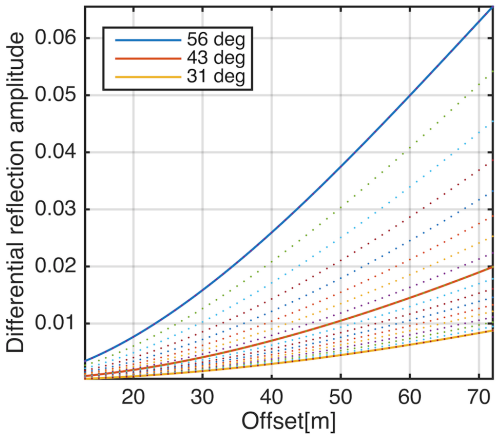

(a)

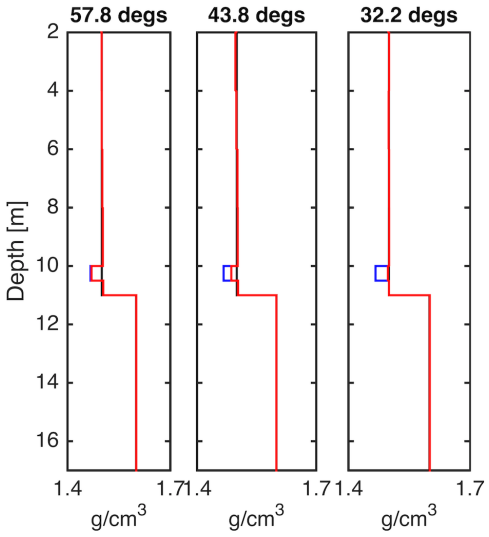

(b)

Figure 3.7: **Constant-impedance density sensitivity analysis**. a) Differential reflection AVO computed between a constant density model, and a model where both density and Vp contribution are present, within a reflection angle range corresponding to changes in sea-floor depth from 15 to 50 metres. The solid lines are relative to the models considered for the inversion. The legend contains the reflection angle at the target layer. b) Retrieved density profile (red), against true density profile (blue). The starting density model is homogeneous (black), although it corresponds to a correct P-impedance profile.

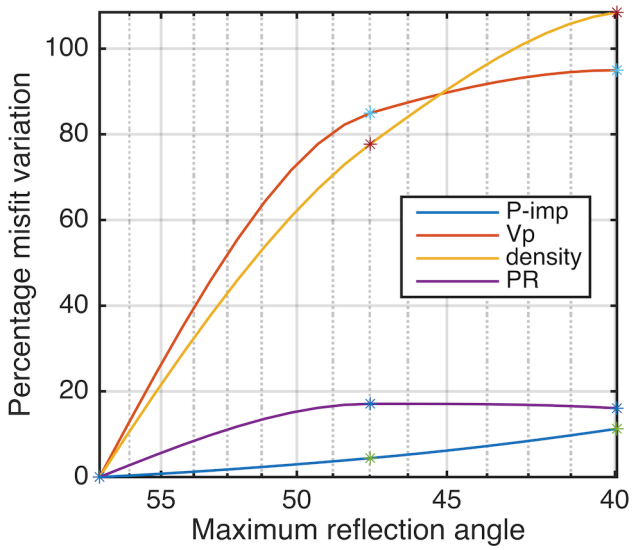

Figure 3.8: **Robustness to changes in the reflection angle range**. Model misfit percentage variation as a function of the maximum reflection angle for the complex 18 layers model per each parameter class. Interpolated from the computed value (asterisks).

quickly below 5% for *Vp/Vs* ratio higher than 4 (Table 3.1). This is apparent in the residual *Amplitude Versus Angle (AVA)* computed between the starting homogeneous Poisson's ratio model and the true model containing the target interface (Fig. 3.10). As a consequence, in the presence of noise the match between retrieved and true S-wave velocity profile deteriorates when the Poisson's ratio background value increases (Fig. 3.11). The *Vp/Vs* increase at the target interface is accommodated for by a *Vs* profile with a similar contrast, but an erroneous relatively long-wavelength trend.

To address this non-uniqueness issue, we propose a structure-constrained gradient preconditioning: in the framework of a sequential strategy, the normalised derivative of the P-impedance obtained from the first stage of the inversion is used to weigh each element of the misfit gradient in the Poisson's ratio stage. Thus the inversion updates preferentially the Poisson's ratio of layers with a significant change in the acoustic properties, imposing a correlation between changes in P-impedance and *Vp/Vs* ratio. The final model misfit is significantly improved by preconditioning (Fig. 3.12), especially for the low-sensitivity, high Poisson's ratio cases. Ambiguities in the interpretation of the interface location are reduced

	ν 1	ν 2	Vp/Vs 1	Vp/Vs 2
a	0.33	0.4949	2	10
b	0.4666	0.4987	4	20
c	0.4920	0.4996	8	40
d	0.4984	0.4999	18	90

Table 3.1: **Sensitivity to Vp/Vs ratio**.Table of Poisson's ratio and Vp/Vs ratio of the models used for the sensitivity analysis. Index 1 refers to the surrounding medium, index 2 to the target layer.

without the need of additional *a-priori* information. This approach remains essentially data-driven and fits naturally in the sequential inversion strategy.

3.3.3 Complex trace inversion to improve the model kinematics

The lack of low frequencies and the limited offsets in UHF data determine a low sensitivity to the mid-to-low wavelengths of the earth-model (Mora, 1980; Jannane, 1989). Although the background P-wave velocity distribution within the top 50 metres of the sub-seabed is close to the water velocity (Hamilton, 1970), this characteristic can be conducive to cycle-skipping and local minimum entrapment in the P-wave velocity inversion (Tarantola, 1984; Virieux and Operto, 2009), which would jeopardise the reconstruction of the elastic model in the following steps. To reduce this problem, when the knowledge of the starting model is poor, we exploit the properties of the complex trace, combined with a multi-scale approach, which progressively includes higher frequency in the inversion (Bunks et al., 1995a). The seismic signal $s(t)$ can be considered as the real part of a complex $c(t)$ trace whose imaginary part is its *Hilbert transform* $h(t)$(Taner et al., 1979), *i.e.* its $\pi/2$ phase-shifted version:

$$\mathbf{c}(t) = \mathbf{d}(t) + i\mathbf{h}(t) \tag{3.7}$$

The *instantaneous phase* (IP) is defined as the inverse tangent of the ratio between the imaginary and the real part, while the modulus of the complex trace is known

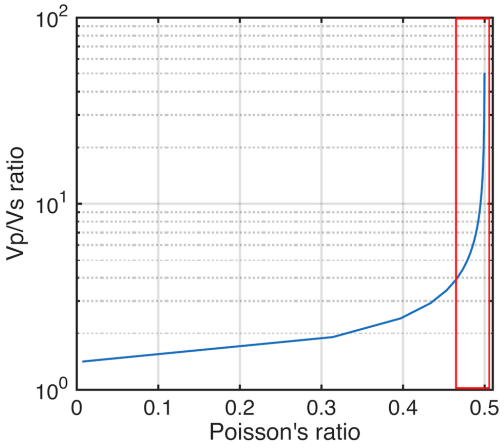

(a)

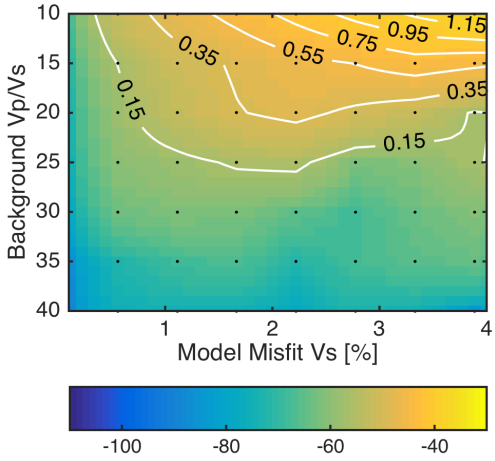

(b)

Figure 3.9: **Poisson's ratio sensitivity**. a) Poisson's ratio vs Vp/Vs ratio. Most unconsolidated sediments fall into the red box, where great changes in Vp/Vs correspond to a narrow Poisson's ratio range and thereby to a small AVO effect, which translates into a poorer sensitivity. b) Over a broad Vp/Vs ratio range of the encasing medium, the L2 data misfit is computed between a reference model and a range of models with increasing percentage perturbation of the target layer S-wave velocity. Data misfit normalised to the total data energy in deciBel. The contour plot shows the percentage iso-misfit surface. The black dots correspond to the computed models.

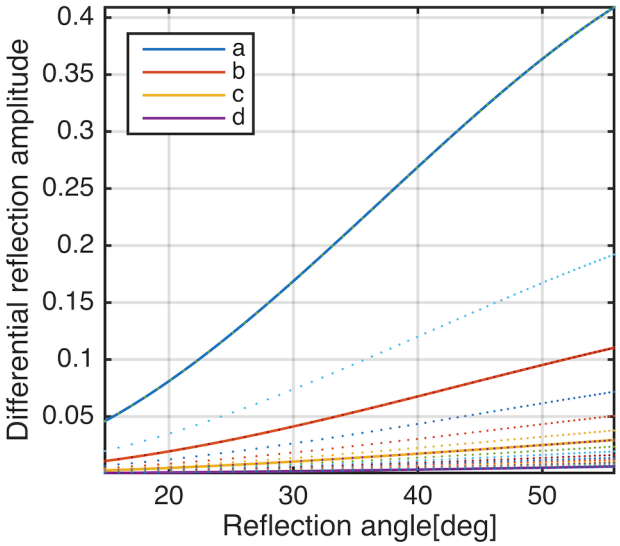

Figure 3.10: **Poisson's ratio sensitivity**. Difference between the AVA of the starting and true Poisson's ratio profiles in the four Vp/Vs ranges considered in the sensitivity analysis (solid lines). Intermediate differential AVA curves are shown with the dotted lines. The quick fall in differential AVA from the first solid line (Vp/Vs=2) to the first dotted line (Vp/Vs=3) is consistent with the quick loss in sensitivity shown in figure 3.9b

.

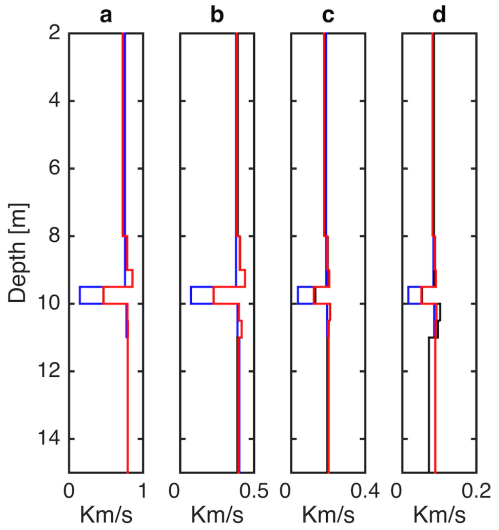

(a)

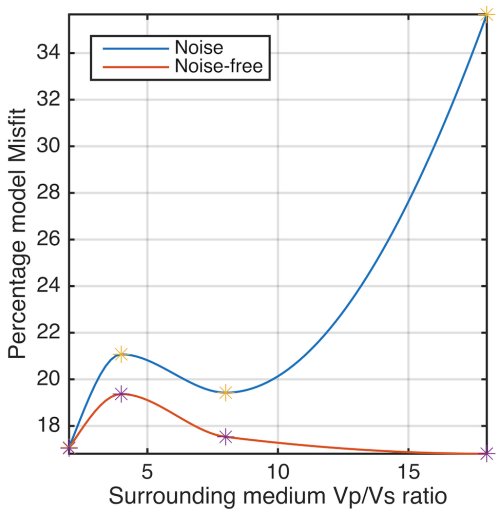

(b)

Figure 3.11: **Poisson's ratio inversion as a proxy to Vs. Sensitivity analysis**. Poisson's ratio inversion for the models from *a* to *d*, with and without noise. a) Retrieved S-wave velocity profile in the noise-free (red) and noise-contaminated data (black), against the true Vs profile (blue). b) Final Vp/Vs ratio misfit for models from *a* to *d* in the noise-free and noise-contaminated cases. Interpolated from measured data (asterisks).

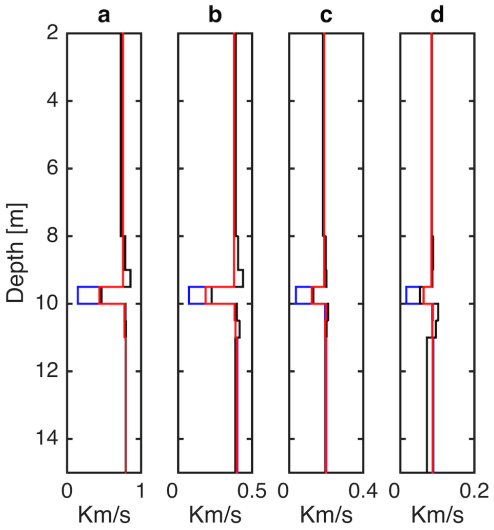

(a)

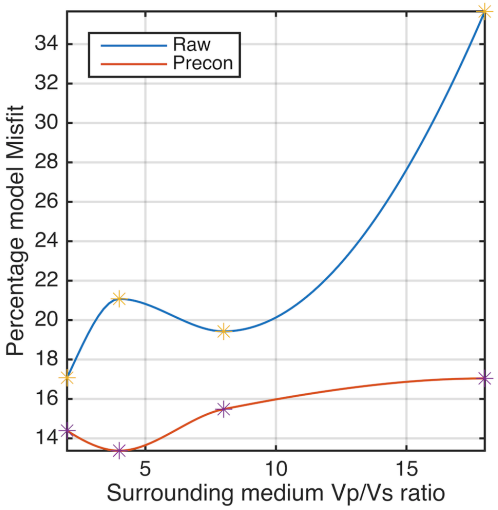

(b)

Figure 3.12: **Poisson's ratio inversion as a proxy to Vs. Sensitivity analysis**. Poisson's ratio inversion of models from *a* to *d* with structure-constrained gradient preconditioning. Noise-contaminated data. a) Retrieved S-wave velocity profile with (red) and without (black) gradient preconditioning, against the true Vs profile (blue). b) Final Vp/Vs ratio misfit for models from a to d with and without gradient preconditioning. Interpolated from measured data (asterisks).

as the *envelope* or reflection strength. Here we use a modified version of the instantaneous phase, proposed by Jimenez-Tejero et al. (2015), where the inverse tangent computed on the ratio between the absolute value of the imaginary trace and the real trace. It reads:

$$\phi(t) = tan^{-1}(\frac{|\mathbf{h}(t)|}{\mathbf{d}(t)}) \tag{3.8}$$

Separating instantaneous amplitude and phase information of the seismogram is beneficial to the convergence properties of FWI (Fichtner, 2011; Bozdag et al., 2011; Fichtner et al., 2008). The modified instantaneous phase is less liable to cycle skipping when FWI is applied to limited-offset, band-limited seismic reflection data (Jimenez-Tejero et al., 2015), which is commonly the case in near-surface marine reflection seismic; furthermore, the phase-only virtual source for P-wave velocity is naturally uncoupled in the reflection regime with Poisson's ratio and density over the whole offset range, for it is less AVO-dependent. For elastic seismic inversion, the complex trace attributes are easily incorporated into a multi-stage approach, where the instantaneous phase is inverted first for the P-wave velocity distribution until convergence is reached and the reflected phases are correctly aligned; after that, the elastic model parameters are inverted for using a misfit functional based on the instantaneous amplitude. The same considerations about the sensitivity to the elastic model space hold in the envelope-based misfit functional, as the trace envelope is sufficient to describe the AVO characteristics of the gather.

3.3.4 The source-independent approach

Inaccuracies in the estimation of the source wavelet are among the main causes of systematic error in the FWI of real data. Statistical source estimation based on the seismic convolution theory assumes a white reflectivity series (Dey and Lines, 1998; Mallick and Adhikari, 2015); although this is the most popular approach in seismic modelling and imaging, such an assumption is likely to be violated in UHF near-surface data, because the short reflectivity series involved do not allow for a statistically robust estimate of a white signal and graded boundaries become increasingly important at the sub-metric scale. More complex methods, such as homomorphic deconvolution in the cepstral domain (Ulrych, 1971), are compromised by strong ghost contamination. Therefore we use the source normalisation

scheme proposed by Lee and Kim (2003). According to the convolution theory, a seismic trace can be expressed in the frequency domain by multiplying the complex spectra of the source and the impulse response of the propagation medium, or *Green's function* (Aki and Richards, 2002).

$$\mathbf{d}(\omega) = \mathbf{s}(\omega)\mathbf{g}(\omega) \tag{3.9}$$

Let $\mathbf{d}_R(\omega)$ be a reference trace chosen from the multi-channel seismic gather, where $\mathbf{g}(\omega)$ in Eq. 3.9 is replaced by $\mathbf{g}_R(\omega)$. Normalising the seismogram for the reference trace in the frequency domain effectively deconvolves the data from the source signature:

$$\mathbf{d_N}(\omega) = \frac{\mathbf{s}(\omega)\mathbf{g}(\omega)}{\mathbf{s}(\omega)\mathbf{g}_R(\omega)} = \frac{\mathbf{g}(\omega)}{\mathbf{g}_R(\omega)} \tag{3.10}$$

where $\mathbf{g}_R(\omega)$ is the impulse response at the reference receiver. In Eq. 3.10, $\mathbf{d}_N$ is independent from the source signature and essentially reduced to the *Green's function* normalised to the impulse response at the reference receiver location, normally chosen to be the closest to the source (Lee and Kim, 2003; Joo et al., 2012; Kwon et al., 2015). In the so-obtained normalised data space, the inversion, rather than being driven by the recorded wavefield, seeks for the match between the relative changes in the impulse response of the medium with respect to the reference trace position.

No changes in the virtual sources radiation patterns are observed, hence the parameter dependancy of the normalised data from the elastic model space is not modified. The spectral normalisation, however, is liable to instabilities if the reference trace spectrum contains near-zero values at certain frequencies. In order to overcome this issue, the back transformation to the time domain is computed assigning a specific weight to each frequency component to damp out the spikes in the spectra corresponding to poles in the inverse filter. Although this approach would be easily incorporated in a frequency domain inversion, back transformation to the time domain is necessary to allow for the inversion to be performed on the time-dependant complex trace attributes.

3.4 Application to a real UHF dataset

3.4.1 Setting and Data overview

In order to test the performance of the proposed inversion scheme, we apply the methodology to a real UHF multi-channel shallow water seismic gather acquired in the Solent, UK. The seismic source is an electro-acoustic Boomer plate, capable of producing a high-frequency, wide-band and highly repeatable minimum phase pulse (Verbeek and McGee, 1995) (Fig. 3.1); the receiver streamer has 60 channels with minimum offset equal to 10 metres, one-meter group spacing and 7 elements per group. Both source and receiver directivity filters have been applied to the synthetics in the FK domain prior to the misfit computation (Verbeek and McGee, 1995; Riedel and Theilen, 2001). The inversion is performed on the reference-trace deconvolved seismograms, which is expected to be robust against inaccuracies in the wavelet estimate. Since the sea surface multiple reflections are not included in the forward modelling, the data are bottom muted above the first order sea floor multiple; the only other pre-processing applied to the data is the muting of the direct wave and a frequency filtering in the appropriate modelling band.

Previous geophysical data available in the area comprise acoustic quality factor Qp (Pinson et al., 2008), and long-wavelength P-wave velocity field from Migration Velocity Analysis (MVA) (Pinson, 2009), along with lithology, porosity and density log-measurements of a proximal sediment core. Seismic to log calibration identifies a 1-to-3 metres thick gravel layer, with low Qp (c. 50), high P-wave velocity and density; it overlays, separated by an erosive unconformity, an over-consolidated clay-dominated layered sediment sequence, with high Qp (c. 150) and acoustic velocity. The sediment sequence below the unconformity is interbedded by sub-metric shelly and limestone layers, and thus likely has detectable variations of shear properties. At the bottom of this 15 metres thick sequence, there is a strong impedance contrast interface.

The combination of shallow water environment (16 metres water depth) and streamer aperture, makes the reflection angle range wide enough to obtain independent estimates of density and P-wave velocity (64 to 47 degrees from the shallowest to the deepest interface), while the relatively low Vp/Vs ratio of the over-consolidated clayey sequence is favourable to the shear properties inversion.

The medium is parametrised as a stack of 78, 20 cm-thick homogeneous layers, from the seabed at 16 metres below the free surface, down to 15 metres below the seafloor. The MVA velocity profile is used as the starting Vp model. The initial Poisson's ratio model consists of a gradient for the top gravel sequence from 0.5 at the seafloor to 0.45 at the top of the layered sequence, whose value remains constant down to the bottom of the model. The latter is an unusually low value for shallow marine sediments, but is required due to the over-consolidation; tests run with higher average Poisson's ratio resulted in higher data misfit. Although we invert here for the elastic parameters, the forward model includes a long-wavelength Qp model determined using the spectral ratio method from near-offset Boomer and Chirp over the sediment sequence (Pinson et al., 2008); the Qs model is derived from Qp using, in the absence of other information, a high-Q empirical relationship between compressional and shear attenuation, i.e. $Qs = 4/9Qp$ (Aki and Richards, 2002).

3.4.2 FWI and comparison with the ground-truth

In the FWI for the elastic parameters, the strategy described in the methodology section is applied, with a misfit functional based on the complex trace attributes: the modified instantaneous phase is used to obtain a P-wave velocity model robust to cycle-skipping; the elastic model parameters controlling the AVO are then inverted sequentially using the instantaneous trace amplitude. The first stage of the inversion updates the MVA velocity model by fitting the instantaneous phase of the seismogram, starting from a cut-off frequency of 0.5 kHz and progressively broadening the bandwidth up to 1.5 kHz. After convergence is attained in the instantaneous phase domain, the envelope of the seismograms are inverted for P-wave velocity; a near-offset taper is applied to the data to attribute higher weight to the near-vertical reflection amplitude and reduce the crosstalk with Poisson's ratio. In Fig. 3.13, note how the reflection strength inversion updates the velocity model in the absolute values, while the location of peaks and troughs in the velocity structure has already been constrained by the instantaneous phase (IP) inversion. Poisson's ratio inversion reduces the misfit between the computed and the field data, with an importance increasing with increasing offset (Fig. 3.14). No gradient preconditioning is applied in this stage, as the highly heterogeneous

impedance in the shallowest two metres would produce a strong bias in the solution, preventing the model from evolving in the deeper portions; nevertheless, the relatively low Poisson's ratio in the site allows for obtaining a stable result. In the final stage, the inversion for density yields minor improvements in the impedance profile; when convergence is reached, density is inverted for independently from P-impedance, alternating steps of Poisson's ratio optimisation (Fig. 3.15).

A synoptic view of the elastic model and the ground-truth is shown in Fig. 3.16. The seismic inversion site is five hundred metres away from the ground-truth, since the irregular sea bottom at the core site invalidated the 1d assumption. However, the lateral continuity of the reflections in the pre-stack-migrated seismic section (Fig. 3.16) suggests that, other than changes in depths and layer thicknesses, the sediment properties are equivalent. The reflectors of the PSDM seismic section are used to correlate the inversion results to the core measurements, which have been filtered down to the seismic resolution after the removal of outliers and non-significant values. The axis scale of the porosity is reversed, to highlight the positive correlation between the reduction of porosity and the P-impedance (Vardy, 2015); we also expect to find a positive correlation between the clay content and the Poisson's ratio (Hamilton, 1970). The sedimentary log ranges from clay to gravel for loose sediments, whereas the presence of lithified material is marked by values going past the gravel base-line. We divide the section into units, colour coded and labeled in Fig. 3.16.

Unit a. The top 3 metres of the model are characterised by a high-impedance top portion overlaid by a low-impedance, low-density and lower Poisson's ratio deeper part; although no ground-truth density and porosity are available at this depth, the results are consistent with the gravel layer, with internal heterogeneity confirmed by the presence of reflections in the PSDM section. Note in figure 3.13 how the inner structure of the gravel layer recognised by the inversion was instead averaged in a uniform high-velocity layer in the MVA model. A strong reduction of the Poisson's ratio is observed from the top to the bottom of the unit, as expected inside the shallowest seabed sediment as a consequence of increasing consolidation with depth.

Unit b. Here higher impedance and higher Poisson's ratio than the bottom of unit *a* are obtained; the top and bottom boundaries correlate to two strong reflections in the PSDM section, while the core data identifies a clay bed

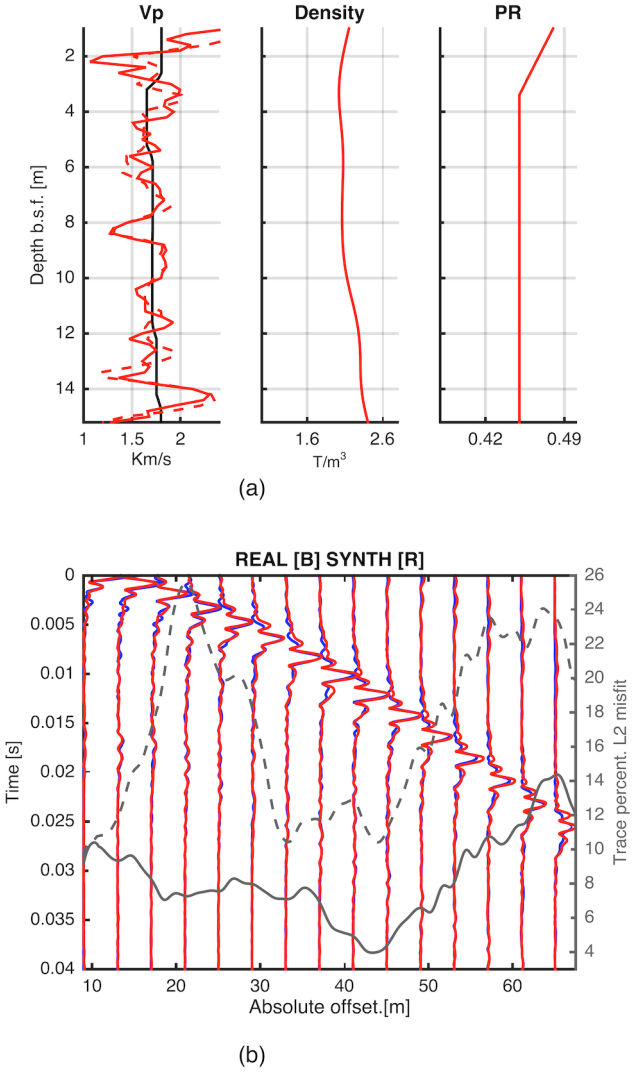

Figure 3.13: **Stage1. P-wave velocity inversion**. Instantaneous phase multi-scale P-wave velocity inversion, followed by a P-wave velocity instantaneous amplitude inversion with short offset windowing. In panel a, the starting model (black) and the final model at this stage (red). The dashed red line is the Vp model after the instantaneous phase inversion only. In panel b, the envelope of the synthetic seismogram (red) overlaid to the real (blue) and percentage misfit as a function of offset, at the start and at the end of the stage (dashed and solid grey lines).

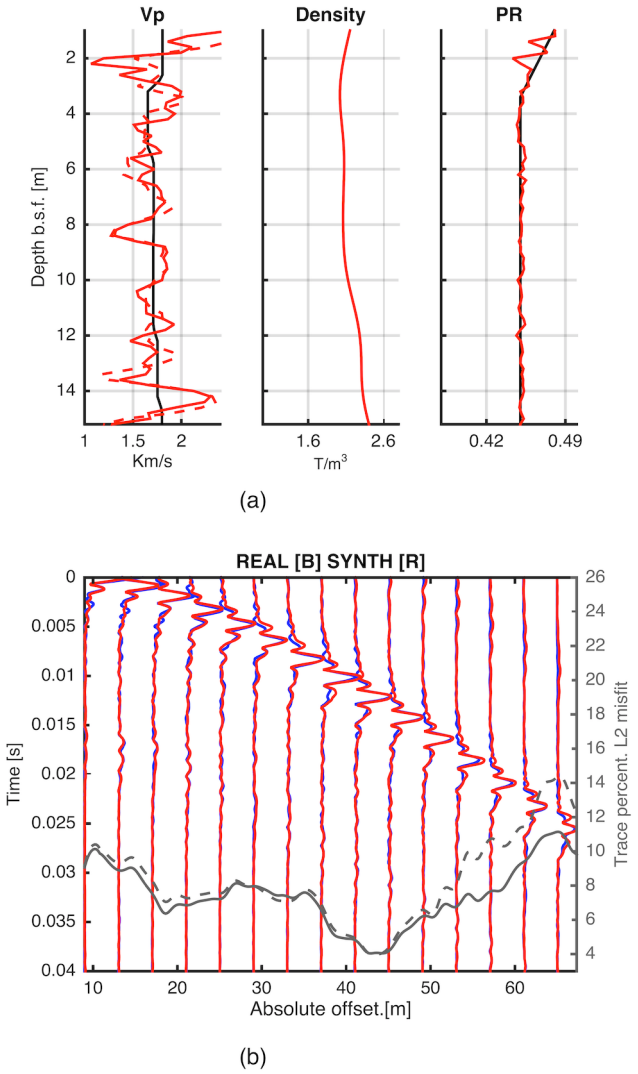

Figure 3.14: **Stage2. Instantaneous amplitude Poisson's ratio inversion**. In panel a, the starting model (black) and the final model at this stage (red). In panel b, the envelope of the synthetic seismogram (red) overlaid to the real (blue) and percentage misfit as a function of offset, at the start and at the end of the stage (dashed and solid grey lines).

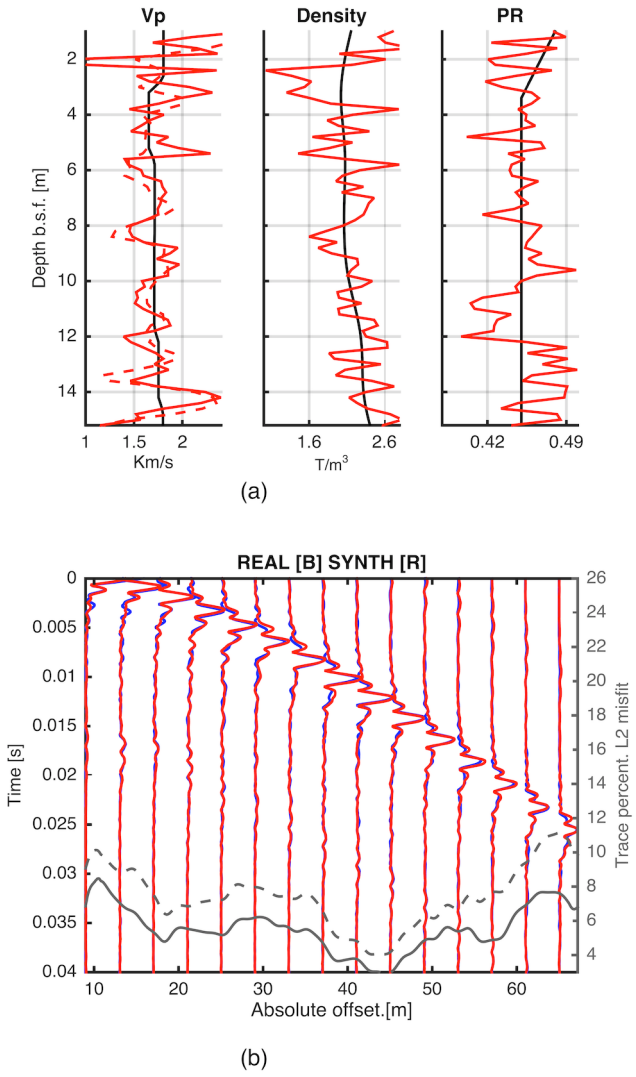

Figure 3.15: **Stage 3. Instantaneous amplitude cyclical density and Poisson's ratio inversion**. Firstly, density is updated independently from Vp to optimise the impedance; after convergence, impedance is kept constant and density and Poisson's ratio are inverted for cyclically. In panel a, the starting model (black) and the final model at this stage (red). In panel b, the envelope of the synthetic seismogram (red) overlaid to the real (blue) and percentage misfit as a function of offset, at the start and at the end of the stage (dashed and solid grey lines).

with a density and porosity structure which mimics the inverted impedance and density profile; note how the strong impedance contrast at the bottom of the unit has no clear correspondence in the density data at the core location, consistently with a weaker and locally less continuous reflection in the PSDM seismic. The increase of Poisson's ratio is in agreement with a more cohesive medium, which is less conducive to shear wave propagation.

Unit c. The impedance and density trends match the porosity and ground-truth density, consistent with changes from fine-grained sediments to silt-dominated beds. Poisson's ratio in this unit is anti-correlated to the impedance profile; this can be explained by an increased stiffness in the micro-fabric of the sediments, which determines an increase of compressional wave velocity correlated to a decrease of the Vp/Vs ratio. At the bottom of the unit, the decrease of impedance and increase of Poisson's ratio correlates to a increased clay content in the lithological log.

Unit d. The Impedance and density profiles have a positive gradient, which correlates to the transition to a coarser-grained portion of the lithological log, reaching a maximum in a composite sandy layer interbedded by a thin clay-rich bed; the latter has a distinct low density and high Poisson's ratio signature in the inverted model. The excellent agreement between the ground truth and the model in this layer is encouraging.

Unit e. Impedance and density decrease in a one-meter thick bed interbedded by a higher impedance and density thinner layer. This correlates with a clay bed interbedded by a thin coarser-grained interval. Poisson's ratio shows a decrease in this unit, with a negative peak corresponding to the coarse-grained layer depth and an increase in the clay content towards the base. Density and porosity from the log are consistent with the inversion results.

Unit f. High impedance and density unit, interbedded by a 20 cm thick bed with low impedance and density. The ground-truth shows a similar pattern and correlates the low-impedance layer with a shelly sediment bed within the clay-dominated sediment. Poisson's ratio has a negative trend at the top, reaches a negative peak at the low-impedance sand layer location, and

sharply increases in the bottom clay-rich portion. In this unit, changes between cohesive and granular medium have a clear signature on the Poisson's ratio variations.

Unit g. This unit shows an alternation of lows and highs in impedance and density. The sharp increase of impedance at the bottom corresponds to a strong continuous reflection in the PSDM seismic; this correlates to a fining-upward, from gravel to clay, sediment interval. The internal lithological layering seems to have a signature in the 20 cm thick sharp decrease of Poisson's ratio at a depth compatible with the gravely-sandy part. Note how, at this depth, the quality of the inverted density profile has deteriorated as a consequence of the narrower reflection angle range.

Unit h. The top part of this unit shows a decrease of impedance and density, which correlates to the density and porosity profiles, followed by an increase which can be related to the top of a rocky unit.

3.4.3 Comments

The real data example corroborated most of the conclusions drawn from the synthetic sensitivity tests. The combination of streamer aperture and water depth ensured that the reflection angle range was wide enough to obtain an independent characterisation of the subsurface in terms of P-wave velocity, density and Poisson's ratio, without assuming any a-priori relationship between the parameters. Despite the simple starting model used and the deterministic approach, a sensible solution has been obtained. The convergence properties of the modified instantaneous phase have been exploited to reduce the risk of cycle-skipping, whereas possible inaccuracies in the source wavelet have been mitigated by using the reference-trace normalisation. The offset-dependent misfit evolution throughout the inversion confirmed that the sequential optimisation is a reasonable and effective way to tackle the hierarchical dependancy of the data on the elastic parameters. The presence of strong internal heterogeneity inside the top gravel layer undermined the effectiveness of the Poisson's ratio gradient preconditioning scheme; however, the relatively low Poisson's ratio in the site and the wide reflection angle, allowed for the shear properties inversion to produce stable results using a raw gradient calculation.

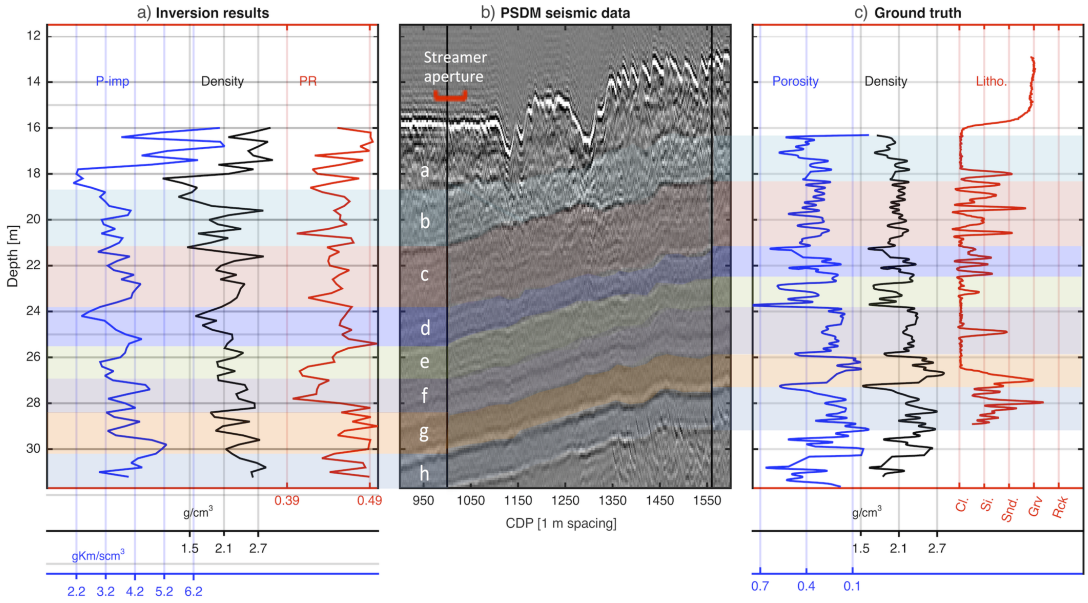

Figure 3.16: **Inversion results interpretation**. In panel a) inverted P-impedance, density and Poisson's ratio. In panel b) PSDM seismic section with location of the acquisition site (left vertical line) and core position (right vertical line). Overlaid to the acquisition site, the red line indicates the width of the acquisition streamer. Note how the vertical dimension is greatly exaggerated. In panel c) wet bulk density, fractional porosity and sedimentary column from log; the latter is a curve whose values are proportional to the relative abundances of clay, silt, sand, gravel and lithified sediment. The labelled units are colour-coded to highlight the correlation between the inversion results and the ground-truth.

The Qp macro-model estimated using the spectral ratio method (Pinson et al., 2008) and the derived Qs were included in the forward model, in particular to account for the strong intrinsic attenuation within the top low-Qp gravel layer. Although a high-fidelity attenuation model would further improve the characterisation of the sediment column, a reliable and precise wavelength-scale Qp-model is difficult to achieve: in the high Qp limit there is little attenuation per wavelength, and in the low Qp limit the energy is unable to propagate. In particular, within the FWI framework, there is low sensitivity to attenuation and strong crosstalk with the elastic model parameters (e.g. Malinkowski et al., 2011; Kamei and Pratt, 2013); furthermore, constraining Qs from marine seismic data would require isolating converted S-waves. In this case study, the sensitivity to Q is further limited by the large-scale high quality factor of the fine-grained, cohesive sediments that form the dipping beds (Pinson et al., 2008; Malinkowski et al., 2011), which limits the change in waveform due to attenuation. However, the large-scale, high precision, Qp model of Pinson et al. (2008) accounts for the intrinsic attenuation of energy, enhancing the stability of the inversion and the reliability of the solution.

Conclusions

This work demonstrates that it is possible to use a multi-channel UHF sub-bottom profiler to derive a high-fidelity distribution of the elastic properties of the subseabed with a sub-metric resolution, using a relatively simple algorithm, with a simple pre-processing of the raw data and without detailed a-priori information. A dedicated modelling and inversion strategy has been developed to account for the specific acquisition conditions and frequency content of shallow marine data within a reasonable computing time on a standard workstation. A broad range of synthetic tests along with a real data case study have been used to explore the capabilities of the inversion method and to define the conditions under which a full elastic characterisation can be obtained.

We have shown that:

- A sequential inversion strategy is an efficient way to tackle the multi-parameter dependancy of the data, and can be used to derive P-wave velocity, bulk density, and Poisson's ratio profiles.

- The relative contribution of density and P-wave velocity to P-impedance can be decomposed, provided that reflection angles > 40 degrees are available.

- P-impedance is the most robust parameter to noise and can be effectively obtained from narrow reflection angle data even if P-wave velocity and density cannot be separated, as long as a reliable low-wavenumber velocity model is available.

- The Poisson's ratio inversion does not require wide reflection angle data, but it suffers from an important loss of sensitivity in very high Vp/Vs ratio media, which can be partially made up for using a structure-oriented gradient preconditioning.

The elastic model obtained shows a good agreement with the ground-truth density and porosity, and a correlation is shown between clay content and Poisson's ratio distribution. Estimates of physical properties, such as undrained shear strength, effective stress, overpressure ratio and porosity, can be derived from the inverted elastic model (Hamilton, 1970; Richardson and Briggs, 1993; Mavko et al., 2009; Vardy, 2015). This opens the way to the extensive use of quantitative seismic interpretation as a means to obtain a detailed characterisation of the shallow sediment properties, as an efficient alternative to costly and time-consuming coring campaign.

Acknowledgements

The authors wish to thank Luke Pinson and John Davis for their help in acquiring the data used as the field data case study, along with Tim Minshull and Antonis Zervos for their informative discussions regarding inversion and geomechanics. We also thank Ludovic Métivier, Richard Hobbs and an anonymous reviewer for the useful comments, that greatly improved the quality of the manuscript. The field data preconditioning was performed using a combination of Landmark's ProMAX software, MatLab, and Seismic Unix. The full waveform forward modelling was performed using the MIT OASES algorithm. All other processing used custom-written algorithms.

3.A Efficient receiver ghost prediction in the general varying streamer depth case

A recorded seismic reflection pressure wavefield is the convolution between a purely up-going wavefield and the impulse response of the acquisition system as a function of receiver depth, free-surface reflection coefficient and spatial frequency (Aytun, 1999). The total wavefield at depth h in the frequency-wavenumber domain can be obtained from the up-going field $\mathbf{P}_k{}^{-}(h_0)$ as:

$$\mathbf{P}_k(h, r_0) = \mathbf{P}_k{}^{-}(h_0)\mathbf{F}1_k(h, r_0)\mathbf{F}2_k(h, h_0) \tag{3.11}$$

where:

$$\mathbf{F}1_k(h, r_0) = (1 + r_0 e^{(-j2k_z h)}) \tag{3.12}$$

predicts the receiver ghost at depth h as a function of the vertical wavenumber $k_z = \sqrt{k^2 - k_x^2}$, with a free-surface reflection coefficient equal to r_0, whereas:

$$\mathbf{F}2(h, h_0) = e^{(jk_z(h-h_0))} \tag{3.13}$$

is the downward propagation operator from h_0 to h accounting for the travel-time difference per each plane-wave component. The time-offset domain seismogram is obtained via two-dimensional Fourier inverse transformation:

$$\mathbf{d}(t, x) = \mathcal{F}^{(-1)}\{\mathbf{P}_k(h, r_0)\} \tag{3.14}$$

In the general case of offset-varying streamer depth and sea-surface reflection coefficient, the complete N-channels seismic gather can be obtained by selecting each trace from the corresponding redundant-offset domain gather and then merging the offsets. A compact mathematical formulation exploits the properties of the two-dimensional *dirac* delta function:

$$\mathbf{d}_i(t, x) = \mathcal{F}^{(-1)}\{\mathbf{P}_k(h(i), r_0(i))\} \tag{3.15}$$

$$\mathbf{d}(t, x) = \sum_{i=1}^{N} \int_{-\infty}^{+\infty} \int_{-\infty}^{+\infty} \delta(t - \tau, x_i)\mathbf{d}_i(\tau, x_i) d\tau dx \tag{3.16}$$

As opposed to an explicit full wavefield modelling, only the computation of the up-going wavefield at constant depth is required, and the whole gather is obtained by signal manipulation, with significant savings in the computing cost.

In general, the filter parameters h and r_0 are not known in advance with the accuracy required by UHF seismic modelling and need to be estimated from the data. The receiver ghost loci in the frequency-offset (Fx) domain are a function of the receiver depth:

$$fn_{(x_i)} = n\frac{V_w}{2h_{x_i}\cos(\theta(i))} \tag{3.17}$$

where n indicates the order of the harmonic, V_w is the water layer velocity and θ is the reflection angle from the sea-floor, which can be approximated as the ratio between the traveltimes (Pinson, 2009):

$$\theta = (t_0/t_i) \tag{3.18}$$

provided that t_0 corresponds to a near-vertical reflection. Eq. 3.17 establishes a linear relationship between receiver-ghost null-frequencies and the reciprocal of the receiver depth as a function of offset. The estimation of the offset-dependent receiver depths can be then cast as a linear inverse problem (Aster et al., 2005); provided that more than one harmonic per offset is available, the problem is over-determined and the linear formulation is convenient to derive robust confidence intervals for the solution (Menke, 1989; Aster et al., 2005). In Fig. 3.17 we show the observed null frequency versus the predicted null frequency for the estimated depth, overlaid to the frequency-offset amplitude spectrum of the real data. The estimated depth profile in the lower panel shows a clearly sagging geometry and the effect of the tail-buoy in the far-offset channels.

The reflection coefficient per each each channel can be conveniently obtained as the solution of a non linear optimisation problem using deterministic algorithms as simple as the bisection method (Burden and Faires, 1985); the optimal $r_0(x_i)$ maximises the normalised cross-correlation value between the predicted trace and the desired trace at the appropriate offset. Although this step is model-based, it only requires an accurate a-priori estimate of the sea-floor depth: the normalised cross-correlation removes the dependency of the results on the accuracy of the sea-floor reflection AVO, while signal tapering around the sea-floor reflected arrival helps to attenuate the bias due to the inaccuracies of the elastic model. The estimated reflection coefficient obtained for the real data didn't differ significantly from -1 and hence are not shown here.

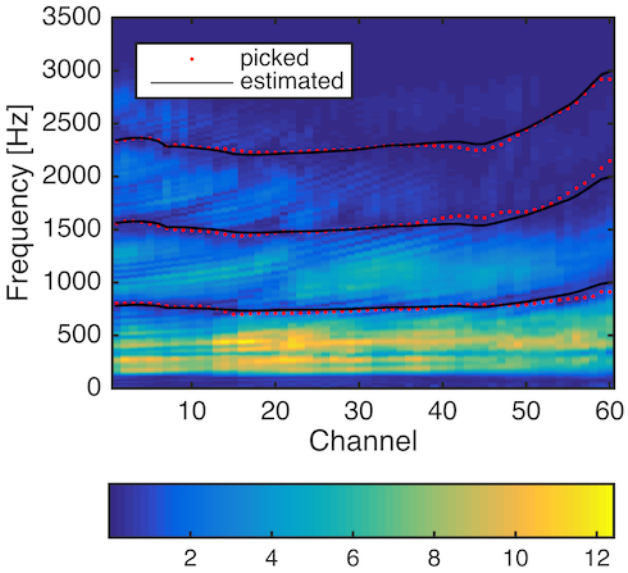

(a)

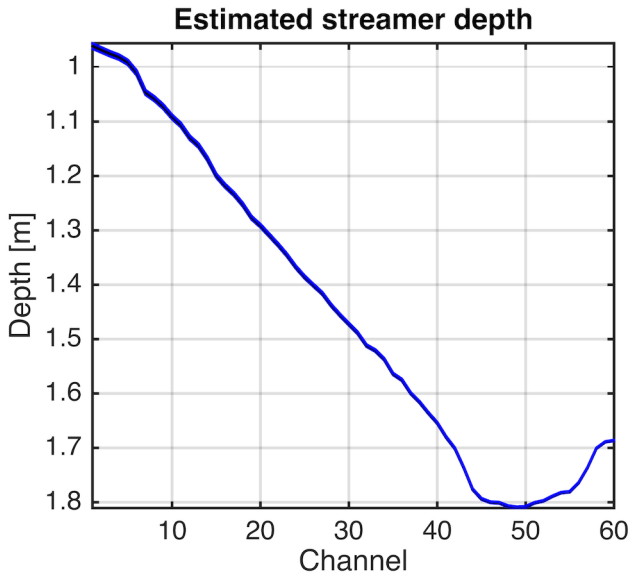

(b)

Figure 3.17: **Streamer depth estimation**. In panel a, the frequency-offset power spectrum with overlaid the picked and the predicted null frequencies; the latter are computed using Eq. 3.17 from the inverted streamer depth shown in panel b. Note that the sagging receivers' depth profile and the uplift in the farther channels due to the use of a tail-buoy.

4

Decimetric-resolution stochastic inversion of shallow marine seismic reflection data; dedicated strategy and application to a geohazard case study

This chapter has been sent for publication as G. Provenzano, M. E. Vardy, T. J. Henstock, 2018. Decimetric-resolution stochastic inversion of shallow marine seismic reflection data. Dedicated strategy and application to a geohazard case study. Submitted to **Geophysical Journal International**

Summary

Characterisation of the top 10-50 m of the subseabed is key for landslide hazard assessment, offshore structure engineering design and underground gas-storage monitoring. In this paper, we present a methodology for the stochastic inversion of ultra-high-frequency (UHF, 0.2-4.0 kHz) pre-stack seismic reflection waveforms,

designed to obtain a decimetric-resolution remote elastic characterisation of the shallow sediments with minimal pre-processing and little a-priori information. We use a genetic algorithm in which the space of possible solutions is sampled by explicitly decoupling the short and long wavelengths of the P-wave velocity model. This approach, combined with an objective function robust to cycle skipping, outperforms a conventional model parametrisation when the ground-truth is offset from the centre of the search domain. The robust P-wave velocity model is used to precondition the width of the search range of the multi-parameter elastic inversion, thereby improving the efficiency in high dimensional parametrisations. Multiple independent runs provide a set of independent results from which the reproducibility of the solution can be estimated. In a real dataset acquired in Finneidfjord, Norway, we also demonstrate the sensitivity of UHF seismic inversion to shallow subseabed anomalies that play a role in submarine slope stability. Thus, the methodology has the potential to become an important practical tool for marine ground model building in spatially heterogeneous areas, reducing the reliance on expensive and time-consuming coring campaigns for geohazard mitigation in marine areas.

4.1 Introduction

A quantitative high-resolution physical model of the top 50 m of the subseabed is of key importance for a wide range of geohazard and offshore engineering applications: identification of potential shallow landsliding (Vanneste et al., 2013); monitoring of gas storage sites (Cevatoglu et al., 2015); and assessment of offshore structures' stability (Vardy et al., 2012). Currently, engineering-scale sediment characterisation relies heavily on direct sampling of the seabed and in-situ measurements (e.g. Stoker et al., 2009). This is expensive and time-consuming for large areas, as well as being liable to alter the sediment properties during the coring process (Clare et al., 2017; Monrigal et al., 2017; Vardy et al., 2017).

Variations in lithology and pore-pressure conditions produce mechanical layering in the shallow subsurface, that can be conducive to changes in the stability conditions of submarine slopes (Vardy et al., 2012; Vanneste et al., 2013). Corresponding anomalies in compressibility, shear resistance and density, have recognisable footprints on the amplitude and phase of the multi-offset reflected

seismic waveforms (Ostrander, 1984; Ruthenford and Williams, 1989). Therefore, seismic reflection data have the potential to be used as a remote sensing tool for shallow geohazard estimation (Mallick and Dutta, 2002; Vardy et al., 2017). As opposed to reservoir-scale seismic exploration, ultra-high-frequency (UHF, 0.2-4.0 kHz) multi-channel marine seismic reflection data are historically under-used in industry for offshore engineering design, being most often limited to a to semi-quantitative interpretation of the reflection amplitudes and facies geometries. Recent advances, however, have shown the potential use of UHF data as a quantitative tool (Vardy et al., 2017), from acoustic quality factor estimation (Pinson et al., 2008) and acoustic impedance inversion (Vardy, 2015), to elastic pre-stack inversion of the full waveform (Provenzano et al., 2016, 2017).

Full waveform inversion (FWI) is a process by which the initial state of knowledge about a given parametrisation of the propagation medium (model) is iteratively improved, by maximising the fitness between the observed seismograms and the data computed using a forward modelling operator that approximates the wave equation (Mora, 1980; Tarantola, 1984; Virieux and Operto, 2009). The oscillating nature of the data makes the high-frequencies of the inversion strongly non-linear with respect to the long-wavelengths of the P-wave model (cycle skipping; Tarantola, 1984; Fichtner, 2011), and non-linearity is enhanced by the interdependency among the different elastic parameters (Operto et al., 2013; Gholami et al., 2013a,b). A deterministic inversion thus requires an accurate starting model and an equally accurate estimation of the Hessian matrix (Virieux and Operto, 2009; Fichtner, 2011; Operto et al., 2013; Dagnino et al., 2014).

Alternatively, the inversion can be tackled with a stochastic approach, which samples the model space with a density proportional to the *Posterior Probability Density function (PPD)* (Sambridge and Mosegaard, 2002; Sen and Stoffa, 2013). In addition to being less reliant upon the accuracy of the starting solution, stochastic seismic inversion, in principle, allows lots of potentially useful information on the performance of the inversion to be extracted from the PPD (Sambridge, 1999; Tarantola, 2005). This includes, but it's not limited to, the multi-parameter solution uncertainties and crosstalk resulting from the noise content, the limited offset and bandwidth of the data, and the inherent interdependency of coupled parameters. However, most often deterministic FWI is the only feasible approach in three-dimensional environments because of the high number

of model evaluations required in high-dimensionality spaces and the computing cost of the seismogram modelling.

Stochastic optimisers such as Genetic Algorithm (Goldberg, 1989), Simulated Annealing (Rothman, 1985) and Particle Swarm Optimisation (Kennedy and Eberhart, 1995), implement analogies between numerical optimisation and natural biological and physical phenomena. They represent a compromise between the extensive exploration of the model space, and the exploitation of the current state of information about the model (Sambridge and Mosegaard, 2002). Although providing a biased posterior distribution of models (Sambridge and Mosegaard, 2002; Sambridge, 1999; Sen and Stoffa, 1996; Aleardi and Mazzotti, 2017), they are computationally more affordable than a pure Bayesian approach, and more robust against local minima entrapment than a deterministic algorithm (Tarantola, 1984; Sen and Stoffa, 2013; Sambridge and Mosegaard, 2002).

These algorithms have been applied to FWI of both land and marine data, for reservoir characterisation and shallow drilling hazard assessment, (Stoffa and Sen, 1991; Sen and Stoffa, 1992; Mallick and Dutta, 2002; Mallick and Adhikari, 2015; Sajeva et al., 2016; Aleardi and Mazzotti, 2017), especially when a one-dimensional parametrisation of the problem is sensible, and hence the number of unknowns lower. Stochastic optimisers would be especially beneficial to the inversion of seismic data for shallow geohazard purposes, because of the difficulties of obtaining a reliable starting elastic model from a typical UHF reflection dataset, as well as the capability of providing solution error bounds for geological interpretation and engineering design (Morgan et al., 2014; Vardy, 2015; Vardy et al., 2015).

In this paper we present a sub-metric resolution stochastic seismic inversion methodology based upon a genetic algorithm, custom-built for limited offset, limited bandwidth seismic reflection data. The performance of the stochastic algorithm is tested on both synthetic and real data. In summary, this paper aims at demostrating that:

1. Our proposed strategy is effective at reducing the dependency from the search range design compared to a genetic algorithm with a conventional parametrisation.

2. A two-stage multi-parameter inversion with data-driven preconditioning improves the performance of the inversion, and the interpretability of the estimated elastic model.

3. Elastic layering, corresponding to key-features for slope instability, can be successfully identified and quantitatively described; in an area subject to shallow landsliding (Finneidfjord, northern Norway). A sediment bed corresponding to the glide plane of multiple-landslide events is accurately located and its changes in pore-fluid saturation quantified.

This underpins the application of UHF seismic reflection data as a remote sensing tool for ground-model building and geohazard estimation, reducing the need for expensive and time-consuming coring campaigns.

4.2 Data and methodology outline

4.2.1 Example estimation of a starting model from UHF data

Shallow marine seismic reflection data typically suffer from the limited offset and lack of low frequencies of the source-acquisition system, which severely limits the sensitivity to the broad-band multi-parameter space (Mora, 1980; Jannane, 1989). Furthermore, most shallow marine datasets are single-component and do not contain post-critical reflections, which limits the possibility of uncoupling the effect of the different elastic parameters (Kormendi and Dietrich, 1991), as well as the sensitivity to the long wavelength distribution of shear properties and density (Operto et al., 2013; Provenzano et al., 2017). As a result, the solution of the inverse problem is highly dependent upon the starting model (Virieux and Operto, 2009; Operto et al., 2013).

In high-resolution reflection seismic data, due to the limited aperture, a starting model is typically obtained from limited-offset normal-move-out velocity analysis (e.g. Aleardi et al., 2016), from which an interval P-wave velocity profile is derived (Dix, 1955). The uncertainty associated with this process can be high, and bias the seismic inversion towards unreliable solutions.

As an example, we simulate a synthetic UHF seismic reflection dataset (Fig. 4.1a), acquired in a shallow marine context with a one-dimensional isotropic elastic

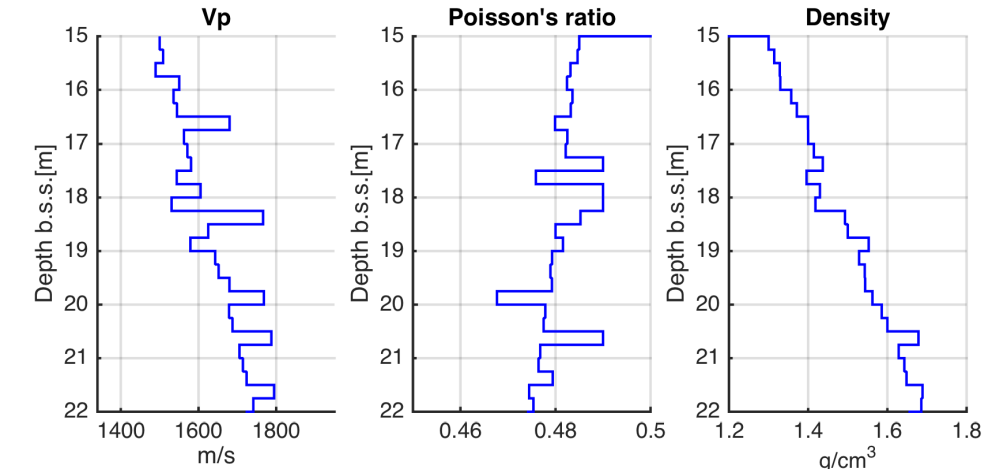

(a)

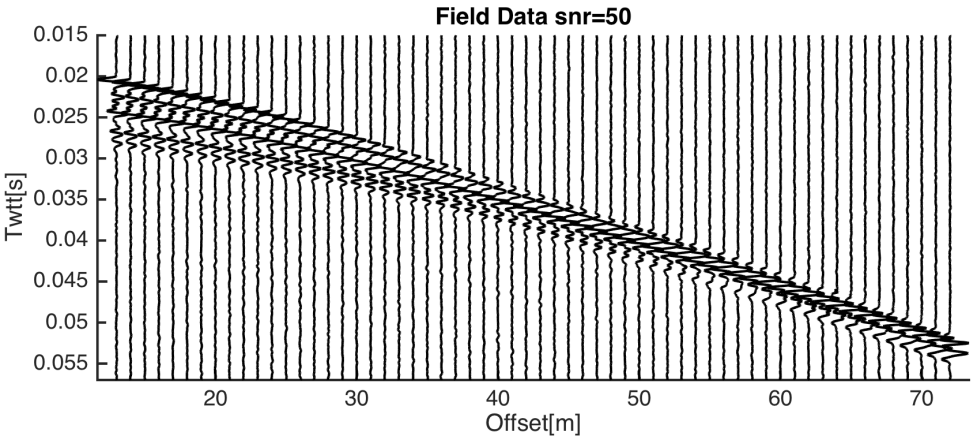

(b)

Figure 4.1: **One-dimensional elastic model and synthetic data**. In panel a) horizontally layered elastic model, parametrised as P-wave velocity (Vp), Poisson's ratio (ν) and density (ρ); depth relative to the sea surface. In panel b) common-shot multi-channel reflection seismic data simulating the acquisition in a shallow marine environment. The seismogram is computed using the *Oases* software (Schmidt and Jensen, 1985; Schmidt and Tango, 1986.), and contaminated with band-limited random noise; signal-to-noise ratio is equal to 50, computed with respect to the strongest reflection

.

shallow subsurface (Fig. 4.1b); the model is a 7-m thick stack of 30 homogeneous layers, representing a site with a strong P-wave velocity gradient and properties reasonable for near-surface sediments (Hamilton, 1970). We suppose no data-independent information is available in the site about the P-wave velocity trend, and we want to derive interval velocities from reflection moveout semblance analysis.

The source wavelet is the signature of a Boomer electro-acoustic plate, whose effective bandwidth spans from 0.2 to 2.5 kHz (Verbeek and McGee, 1995); the simulated streamer comprises 60 channels with 1-m spacing and minimum offset of 13 m. A realistic level of band-limited random noise has been added to the data; namely, the signal-to-noise ratio, computed with respect to the seafloor reflection amplitude, is equal to 50. Note in Fig. 4.1b how the strong P-wave velocity gradient determines a compression of the time delay among reflections at the longest offsets, which makes it difficult to accurately use moveout-based velocity estimation tools. The broad moveout semblance maxima (Fig. 4.2) produce uncertainties in the velocity picking that translate into a broad range of possible interval P-wave velocity profiles; such variability is in general beyond a cycle-skipping safe domain (Virieux and Operto, 2009; Fichtner, 2011; Aleardi et al., 2016), and suggests that move-out velocity analysis is not a robust tool to obtain a starting P-wave model for local-search FWI. In the absence of reliable Cone Penetrometer Tests (CPT) and/or core-logs, the starting S-wave velocity and density profiles would also be derived from this P-wave model, further jeopardising the chance to converge to the global minimum of the multi-parameter objective function.

The latter is in fact a typical situation in engineering-scale seismic exploration and clarifies the potential benefits of a seismic inversion strategy that reduces the dependency upon the initial state of information. In the next sections, we demonstrate that, although the inherent sensitivity limitation of this kind of data cannot be overcome, our stochastic approach can still provide a robust solution when a wrong velocity trend is used to build the starting model search range.

4.2.2 Proposed genetic algorithm-based strategy

Stochastic optimisers like the genetic algorithm (GA Goldberg, 1989) represent a compromise between the systematic exploration of the model space and the

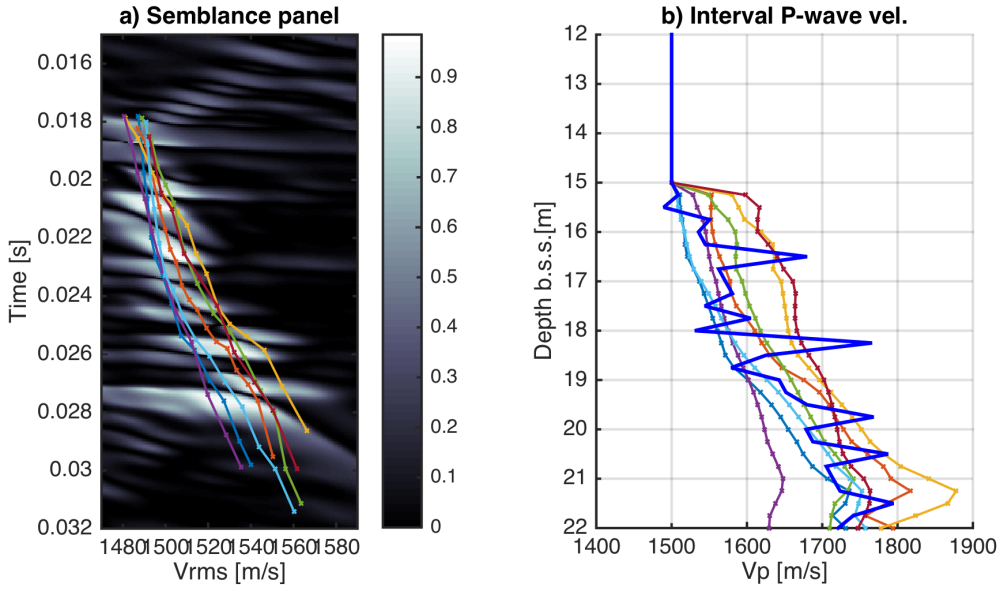

Figure 4.2: **Deriving low-frequency P-wave velocity model from NMO analysis**: panel a) stacking velocity semblance panel with possible V_{rms} pickings; panel b) interval P-wave velocity models (dotted-lines) derived using Dix (1955) equation from the V_{rms}, and true Vp model (solid blue).

exploitation of the current state of information about the physical model (Sambridge and Mosegaard, 2002); although more robust to cycle-skipping than deterministic FWI (Sajeva et al., 2016), they can similarly suffer from local-minima entrapment, depending on the model space dimensionality and the nature of the objective function (Sajeva et al., 2017).

In this paper, we introduce relevant changes to a classic evolutionary algorithm framework, in order to attenuate the bias inherited from ill-characterised a-priori distributions, and reduce the effective size of the model space. The proposed strategy is based on the genetic algorithm developed by Vardy (2015), adapted to the multi-parameter FWI of multi-channel data (Fig. 4.3). The subsurface is assumed to be horizontally stratified (Fig. 4.1), and each isotropic elastic layer is parametrised in terms of P-impedance (Z), Poisson's ratio (ν) and density (ρ) (Debski and Tarantola, 1995; Igel et al., 1996; Provenzano et al., 2017). The inversion workflow can be divided into 3 stages:

1. In the first stage, the goal is to obtain a high-fidelity P-wave velocity model, robust to inaccurate a-priori information. An initial population of P-wave

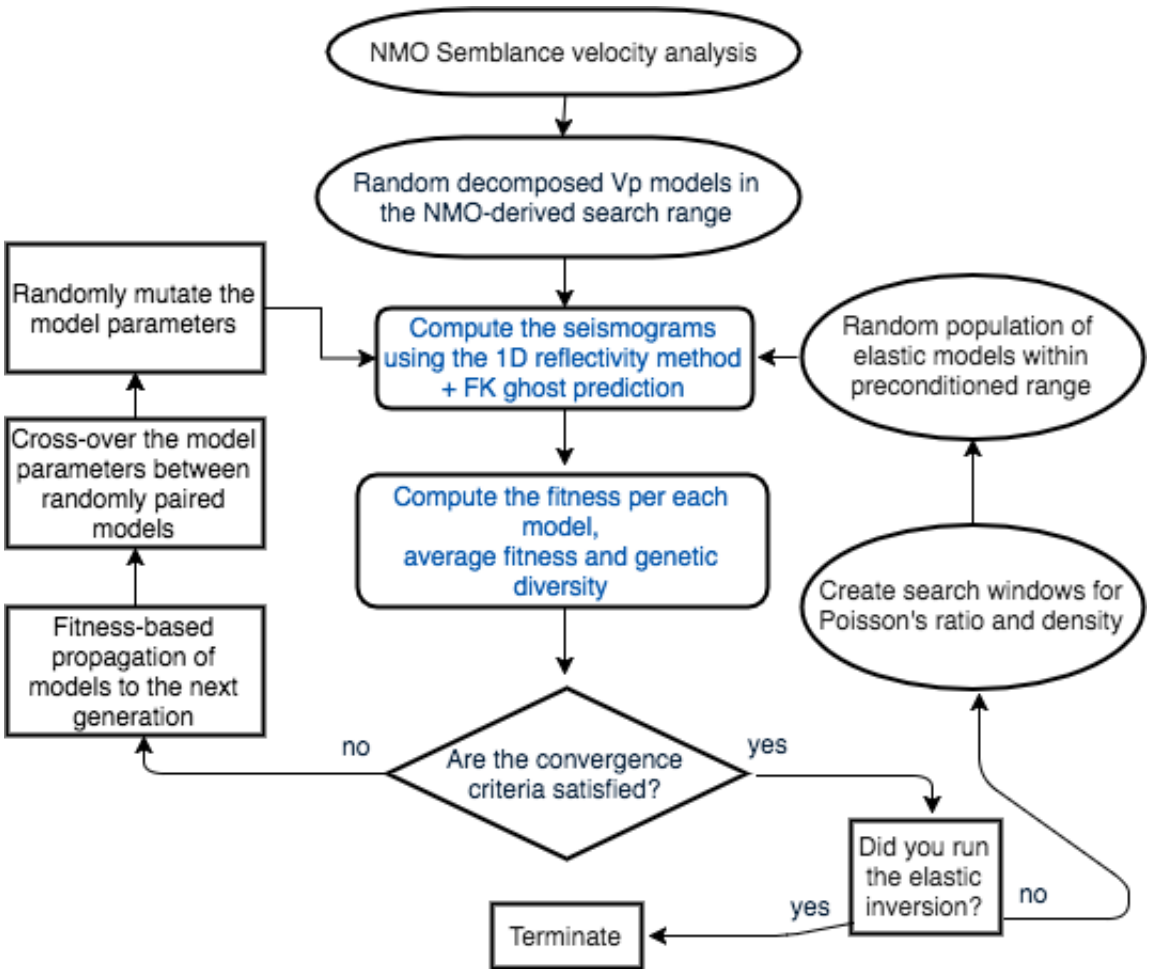

Figure 4.3: **Inversion workflow**. The computation of the forward model within each generation is parallelised using openMP.

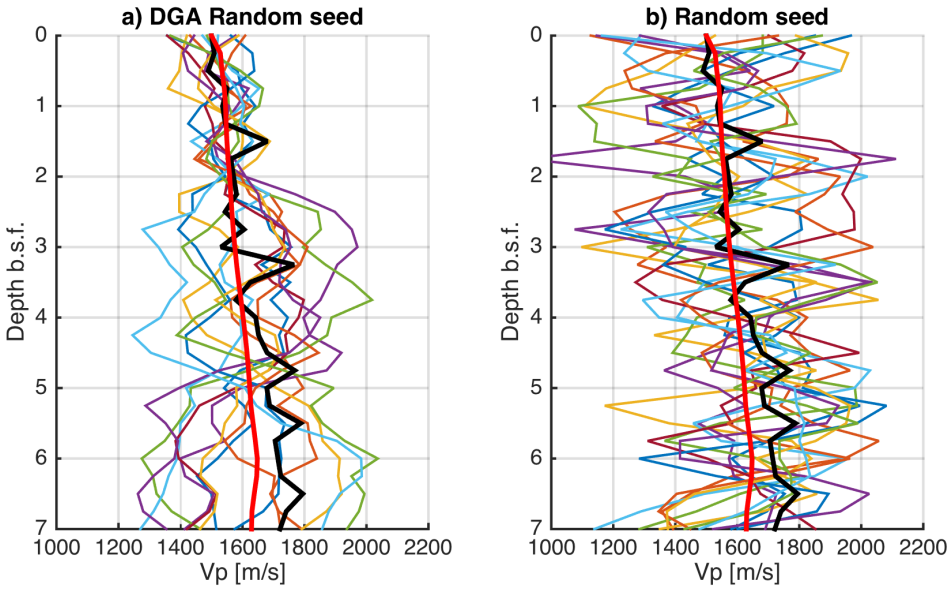

Figure 4.4: **Random seeds** In panel a) random models (thinner lines) generated by the decomposed algorithm within a search range designed around the semblance velocity model (thick red), and true Vp model (thick black). Correlation length for the high-frequency component is equal to the thickness of the individual layer ($0.25cm \simeq \lambda_{min}/4$), and $\simeq 1m$ for the long component. In panel b) the random models are instead generated by sampling randomly the same Vp search window.

profiles is generated within a search-window built around the semblance-derived interval velocities. Unlike a classic GA, which performs a purely random exploration of the model space, here each individual of the initial population results from the superposition of a random long-wavelength component and a high-frequency perturbation, defined according to the frequency band of the data, and the minimum expected velocity. For each model, the multi-channel seismogram is computed using a homogeneous-layer method (Schmidt and Jensen, 1985; Schmidt and Tango, 1986.) and the value of the objective function is calculated. The following generation is then populated using a stochastic remainder criterium (Vardy, 2015); all models with fitness better than average are propagated to the next generation and the remaining individuals are randomly selected among the entire population. The survivors are crossed-over and mutated according to user-defined crossover and mutation probabilities. The long- and short-wavelength components of the model are completely decoupled, with the crossover and mutation elements of the GA operating on each independently.

2. After convergence is attained, the data are inverted for the elastic properties (Z, ν, ρ) . The genetic algorithm operates on the multi-parameter elastic space, preconditioned by the robust P-wave velocity model obtained in the previous stage. Shear-wave velocity and density trends, which can't be constrained independently by single-component marine seismic data alone (Operto et al., 2013), are derived from the long wavelengths of the P-wave velocity profile, by using appropriate rock-physics relationships (Hamilton, 1970; Richardson and Briggs, 1993; Mavko et al., 2009). By contrast, the high-frequency, reflective component, of the elastic model is estimated from the offset-dependent seismic waveforms. The width of the search range is modulated by the local P-wave reflectivity; the higher the P-impedance contrast, the wider the range. The rationale is to bias the inversion towards regions where anomalies in the elastic properties are most probable: Poisson's ratio and density are expected to change where P-wave impedance changes (Hamilton, 1970; Mavko et al., 2009), i.e. at interfaces between sediment types. Thereby the effective size of the model space is selectively

reduced, thus improving the efficiency in high-dimensional parametrisations (Tarantola, 2005; Sajeva et al., 2016).

3. Multiple independent runs are performed, each starting from an independent random population of models (Sen and Stoffa, 1992; Vardy, 2015). This produces an ensemble of statistically independent solutions, from which the model parameters' error boundaries can be computed, without the bias of genetic drift and model inter-dependency (e.g. Vardy, 2015). The process is iterated until the estimate of the median model is stable, as in Stoffa and Sen (1991). The aim of this process is to obtain a measure of the reproducibility of the solution rather than an importance sampling of the PPD, which is not achievable using a GA without further exploration of the model space (Stoffa and Sen, 1991; Sambridge, 1999; Aleardi and Mazzotti, 2017).

In the next section we provide experimental proof of the efficacy of the methodology on both synthetic and real data: the decoupled approach, is effective at retrieving the true P-wave velocity model even when it lies at the edges of the range, while the structural preconditioning improves the efficiency of the elastic inversion by reducing the size of the model space. Both synthetic data (Fig. 4.1) and a real case study are presented. We will hereafter refer to our proposed strategy as *DGA (Decomposed Genetic Algorithm)*. In analogy with Bayesian methods, the search domain will be referred to as a-priori probability density function (PDF).

4.3 Implementation and results

4.3.1 Robust P-wave velocity estimation with constant density and shear properties

Here we compare the proposed DGA to a GA inversion with a traditional parametrisation, for the reconstruction of an accurate P-wave velocity model starting from a ill-constructed a-priori search domain. The data and the true elastic model are shown in Fig. 4.1. The search window is built around the interval P-wave velocity model derived from semblance velocity analysis (Dix, 1955), in purple in Fig. 4.2, which represents an underestimate of the velocity gradient of about 5 %. Hence, the true model is significantly offset from the centre of the uniform a-priori PDF.

The model is parametrised as a stack of 30 layers with a thickness of 25 cm, down to a depth of 7-m below the seafloor. Only P-wave velocity is inverted for, whereas Poisson's ratio and density are kept fixed at this stage to a uniform profile ($\nu = 0.48$ and $\rho = 1.5 g/cm^3$). A population of 160 individuals sampled from the a-priori PDF evolve through 150 generations according to a L1 data fitness criterium (Menke, 1989), based either on the real waveform or its modified instantaneous phase (MIP; Jimenez-Tejero et al., 2015).

The DGA explores the model space by explicitly decomposing each random subsurface profile into a slowly-varying component, in the order of the dominant propagated wavelength ($\geq \lambda_{dom}$), and an independent high-frequency perturbation, in the order of the tuning thickness for the maximum frequency contained in the data ($\simeq \lambda_{min}/4$). This is achieved by generating two random series of chromosome values (i.e. P-wave velocity per layer), with correlation lengths respectively equal to λ_{dom} and $\lambda_{min}/4$, and superimposing them to create the broadband subsurface model (Fig. 4.4). For the P-wave velocities and source bandwidth of this test, the correlation lengths of the short and long wavelength components are respectively 0.25 and 1.25 m (Table 4.1). The decomposed approach is taken in both the sampling of the starting random population from the search range, and in the mutation and crossover through the generations. High mutation rates and relatively low crossover probabilities are used to enhance the explorative nature of the algorithm, and prevent from earlier convergence to local minima (Sen and Stoffa, 2013). The process thus accounts for the dual nature of the subsurface properties the seismic data are sensitive to, i.e. kinematic and reflective (Mora, 1980; Jannane, 1989). By contrast, in a conventionally parametrised GA the reconstruction of the broadband earth model results from random mutation and crossover operating on each layer individually. Unlike the DGA, the model samples of the GA are high-variance profiles clustered around the centre of the search domain, and are in fact more likely to produce geologically unrealistic features (Fig. 4.4).

In Figs. 4.5 and 4.6, we compare the median model and the 66 and 95 % solution confidence limits obtained from 50 independent inversion runs. The variation band of minimum and average L1 data misfit across the generations is also

	One parameter (Vp)	Elastic (Z, ν, ρ)
L(m)	1.25	-
S(m)	0.25	0.25
Number of variables	30	90
Mutation prob.	0.2	0.001
Crossover prob.	0.4	0.6
Number of individuals	160	320
Number of generations	150	150
Number of runs	50	50

Table 4.1: **DGA inversion parameters**. User-defined genetic algorithm parameters for the first-stage P-wave velocity inversion, and the following preconditioned simultaneous elastic inversion.

shown. The results show that the spectrally-decomposed algorithm outperforms the conventional parametrisation in attenuating the bias of the starting model: regardless the seismic attribute used, the true model is in fact included in the 95 % confidence limit of the DGA solution (grey shaded area in Figs. 4.5 and 4.6). However, the median model of the DGA waveform-based inversion is offset from the true P-wave profile, and the reproducibility of the solution is poor (Fig. 4.5). The MIP-based misfit functional (Jimenez-Tejero et al., 2015) ensures more stable results (Fig. 4.6), proving a higher sensitivity to long-wavelength changes in the model, and lower liability to cycle skipping. In contrast, the waveform based objective function strongly suffers from local minima entrapment, because of the high non-linearity of the objective function with respect to the P-wave velocity trends (Virieux and Operto, 2009; Operto et al., 2013). Therefore, the modified model exploration strategy is effective at attenuating the footprint of inaccurate a-priori information, but only if combined with an appropriate objective function.

By decomposing the P-wave velocity model into independent long and a short components, and using a misfit criterium robust to cycle skipping, the inaccuracy in the starting model has been compensated for. Also, the model heterogeneities have been correctly located. The next step is to use this result to precondition the high-resolution multi-parameter elastic inversion.

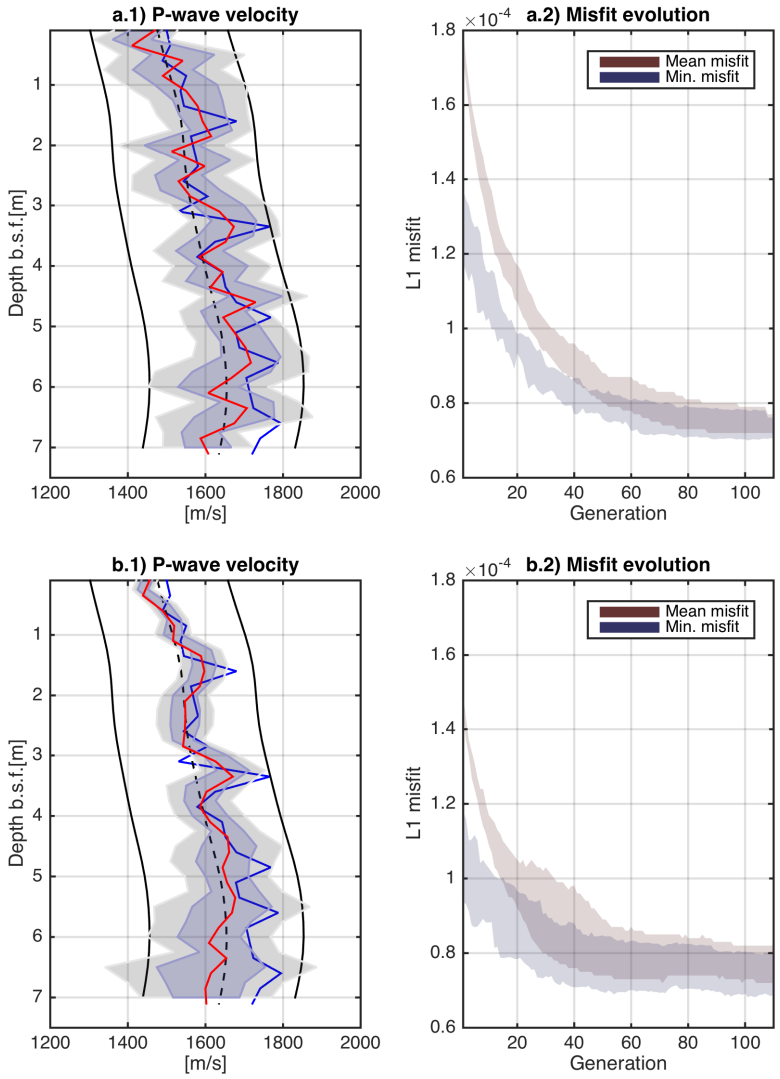

Figure 4.5: **Vp inversion. Waveform L1 misfit functional.** In panel a, results obtained using a GA with a conventional strategy; in panel b, results obtained using our DGA. True model (blue); median model (red) and shaded areas for the 66 (blue) and 95 (grey) % confidence intervals of the solution are computed from an ensemble of 50 independent realisations; the solid black lines are the limits of the search range built around the NMO model (dashed black line). The variability range of the average and minimum misfit evolution over the generations is shown. The final minimum misfit is lower for the DGA inversion, and the true model is included in the confidence interval. However, the high variability of the solution reveals a remarkable liability to cycle skipping.

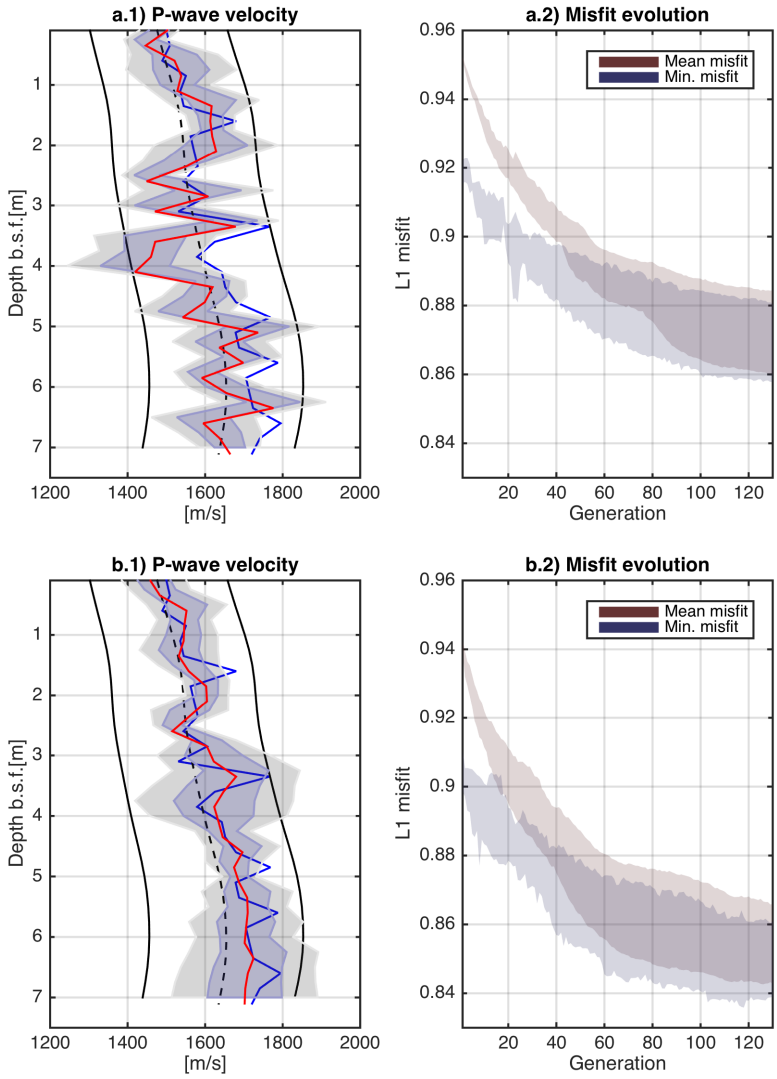

Figure 4.6: **Vp inversion. Complex trace L1 misfit functional.** In panel a, results obtained using a GA with a conventional strategy; in panel b, results obtained using our DGA. True model (blue); median model (red) and shaded areas for the 66 (blue) and 95 (grey) % confidence intervals of the solution are computed from an ensemble of 50 independent realisations; the solid black lines are the limits of the search range built around the NMO model (dashed black line). The variability range of the average and minimum misfit evolution over the generations is shown. Note how the DGA solution (panel b) is less dependent from the central model (dashed line) of the a-priori distribution, and that the final minimum misfit is lower than the traditional GA.

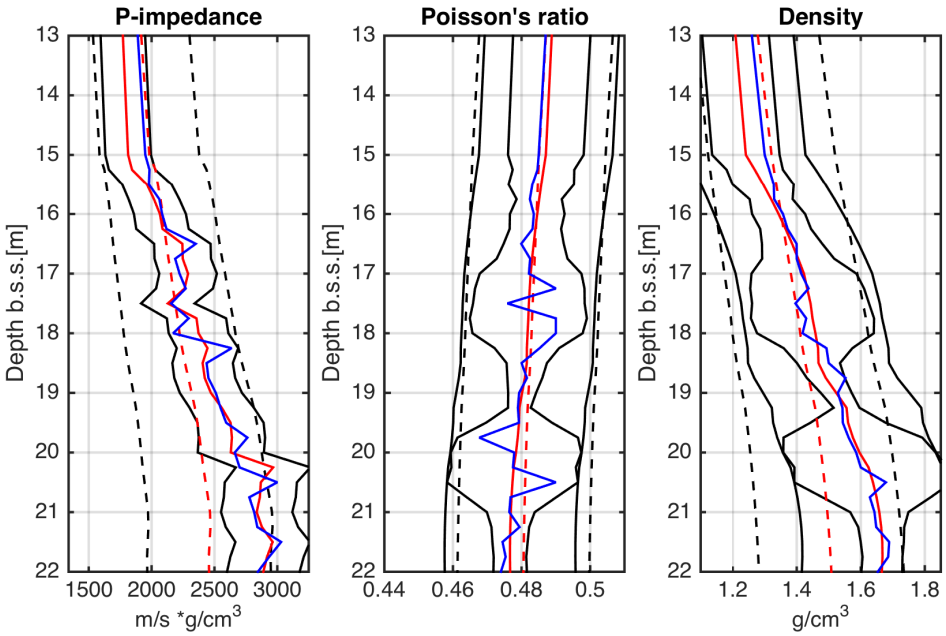

Figure 4.7: **Advantage of using the P-wave velocity model to precondition the search window**. Elastic model parametrised as (Z, ν, ρ). Note that the Z model obtained at the first stage of DGA (solid red), allows us to build accurate estimates of the shear and density trends (also in solid red). The derived ranges (solid black) contain the true model (blue). Using the semblance P-wave model with the same empirical relationship (dashed red), increases the chances of excluding the true model from the search window (dashed black). In this example, this is particularly evident for density.

4.3.2 Structure-preconditioned elastic inversion

Here we exploit the information contained in the estimated P-wave velocity model, in order to guide the inversion for the elastic properties. The model is parametrised in terms of P-impedance (Z), Poisson's ratio (ν) and density (ρ) (e.g. Debski and Tarantola, 1995; Igel et al., 1996; Provenzano et al., 2017). No independent constraint on the shear and density macro-model is posed by the single-component, limited offset data. So, in the absence of independent geological and geotechnical information, a sensible relationship with the P-wave velocity is needed to derive the elastic starting model. We make the assumption that such a relationship is available in our synthetic test, and is representative only of the long-wavelength component of the model. The high-wavenumber component, on the other hand, varies independently for each parameter, simulating changes in lithology and/or fluid saturation (Igel et al., 1996; Mallick and Dutta, 2002); such anomalies are the target of the elastic inversion, and are estimated entirely from the offset-dependent reflected wavefield.

The high-dimensionality of the multi-parameter problem determines a rapid increase of the model space volume with the range width, hence of the number of model evaluations needed to identify and sample its high-fitness region (Tarantola, 2005; Sajeva et al., 2016, 2017). In our specific test, each elastic layer is described by a triad of independent parameters (Z, ν and ρ), for a total of 90 degrees of freedom. It can be therefore beneficial to reduce the volume of the model space by selectively narrowing the search domain. For this purpose, we further exploit the information contained in the P-wave velocity profile to precondition the elastic inversion. The exploration of the elastic model space is biased towards model heterogeneity locations identified by regions of contrasting P-wave velocity, from the results of the first inversion stage.

The preconditioned search range for either ν and ρ, for each depth, is compactly defined as:

$$R = F(Vp_{sm}) \pm w_0 p \tag{4.1}$$

where:

$$p = \frac{\left|\frac{\partial^2 Vp}{\partial d^2}\right|}{max\left(\left|\frac{\partial^2 Vp}{\partial d^2}\right|\right)} \tag{4.2}$$

the search range R is thus obtained from the smooth P-wave velocity Vp_{sm} using the rock-physics relationship F; the half-width w_0 can be modulated by the second

derivative of Vp, computed with respect to the depth d, and normalised to one. In Fig. 4.7 we compare the state of information available from the move-out based interval acoustic velocities with the one from the FWI P-wave profile; the latter allows us to build a more accurate multi-parameter search window, that reduces the risk of ruling out the true model from the a-priori model distribution.

The inversion parameters are summarised in table 4.1. Compared to the Vp-stage, we use a lower mutation rate, a higher crossover probability and a higher number of individuals per generation, to account for the higher number of unknowns (Stoffa and Sen, 1991; Sen and Stoffa, 1992). In Figs. 4.8 and 4.9, we show the inversion results and the marginal confidence intervals for the elastic inversion, respectively with and without range-width modulation. The confidence limits in both case are a high-fidelity representation of the elastic model, despite the low sensitivity of limited-offset marine data to shear properties variations, within the narrow Poisson's ratio range of shallow sediments (Mallick and Dutta, 2002; Provenzano et al., 2017). However, the fully-preconditioned test, with range modulation, produces solution confidence regions with better defined shear and density heterogeneities, especially in the deeper parts of the model.

In Fig. 4.10 the synthetic seismogram for the final FWI-model is overlaid to the real one, and the offset-dependent L1 misfit is plotted for each DGA stage. It is worth pointing out that the Vp-model, although obtained via instantaneous phase inversion, is responsible for a significant reduction of the waveform misfit, especially at the far offsets. The final misfits for the elastic models obtained with the two preconditioning techniques are similar; despite the higher misfit in some of the farthest channels, the fully-preconditioned solution has a higher fitness value, thanks to the better match at the higher-energy shortest offsets.

With a view to reducing the size of the models space, the range-width preconditioning will be key in the inversion of the real case study, where the presence of a 50 cm thick gas-saturated layer requires the inversion to explore a wide range of elastic moduli values in a thick spatial parametrisation.

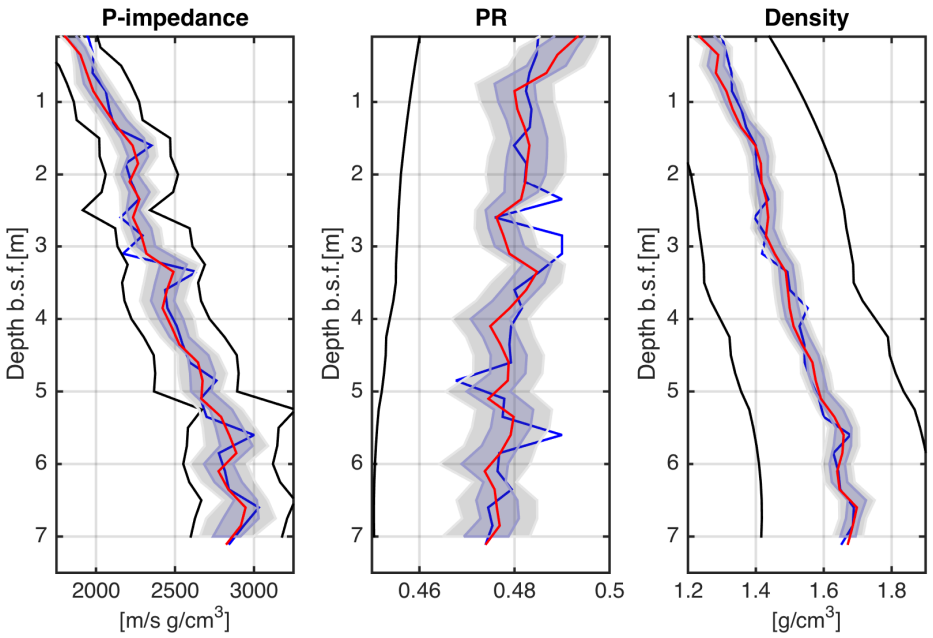

Figure 4.8: **Elastic multi-parameter inversion with long-wavelength preconditioning.** Median model (red) and 66 (blue) - 95 (grey) % confidence intervals obtained from 50 independent inversion runs; true model in blue and range boundaries in solid black. In this test, the preconditioning on Poisson's ratio and density is only in the long-wavelength of the P-wave velocity model obtained in the previous stage.

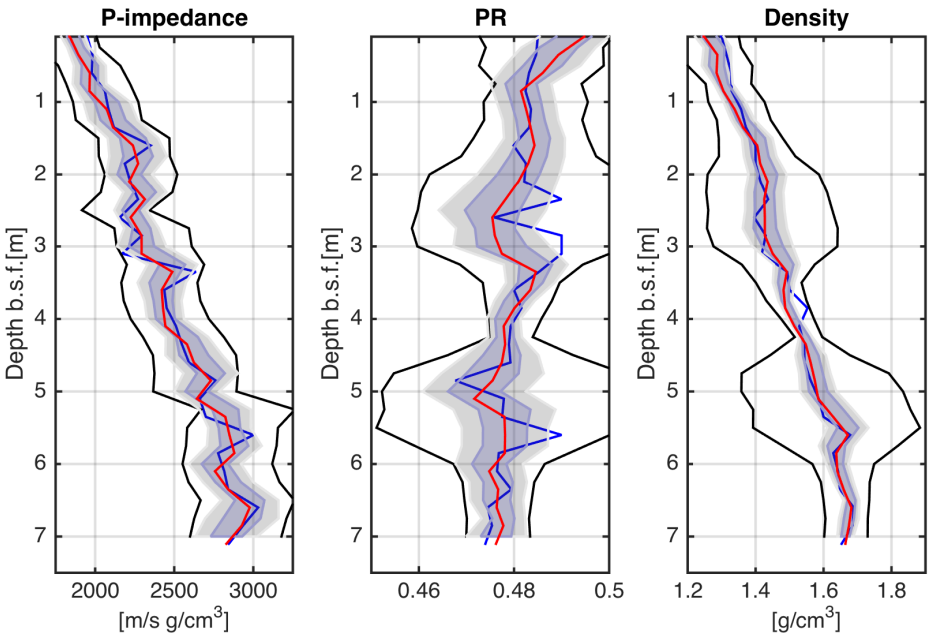

Figure 4.9: **Elastic multi-parameter inversion with full preconditioning.** Median model (red) and 66 (blue) - 95 (grey) % confidence intervals obtained from 50 independent inversion runs; true model in blue and range boundaries in solid black. In this test, full preconditioning is used, and the width of the search range is modulated by the local P-wave velocity model heterogeneities obtained in the previous stage.

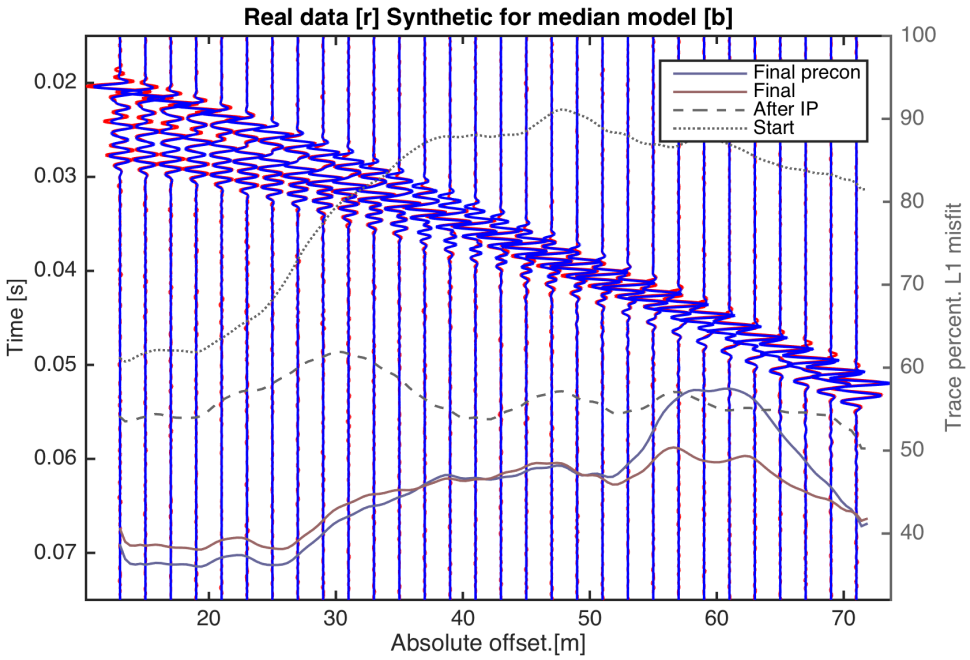

Figure 4.10: **Two-stage elastic inversion offset-dependent misfit**. Real seismogram (red), Synthetic seismogram (blue) for the median model after elastic FWI. Overlaid, offset-dependent trace-normalised L1 misfit for the starting NMO model (dash-dot grey), the final Vp model (dash grey), and the two median models, with and without range-width preconditioning (respectively blue and red).

4.3.3 Identification of shallow weak layers

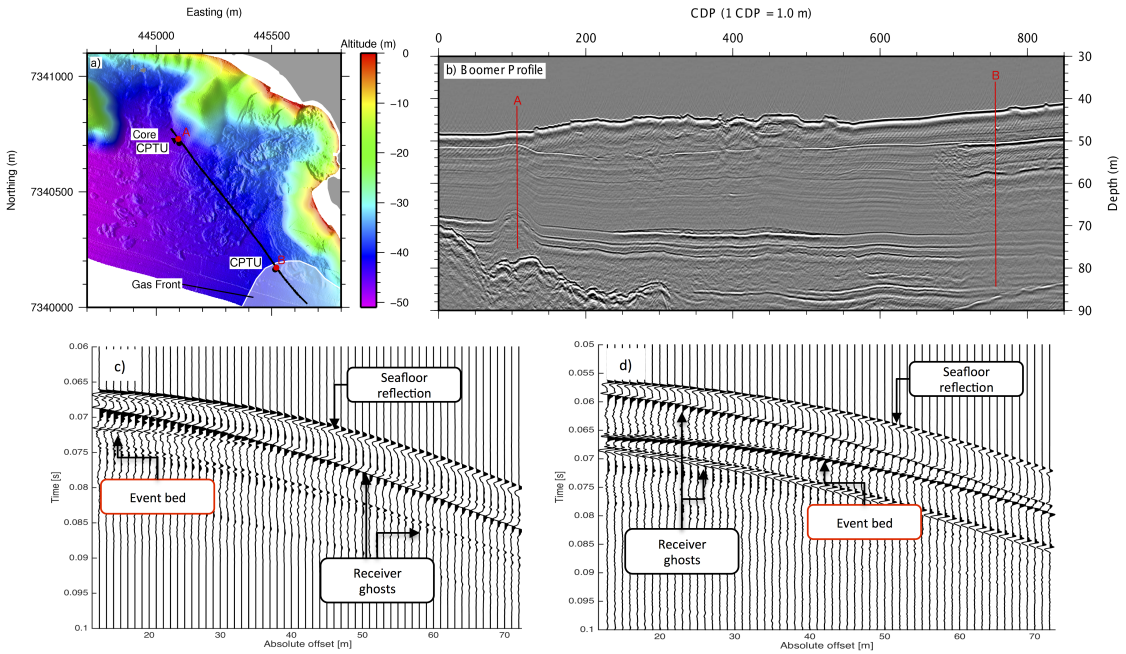

Figure 4.11: **Real data, Finneidfjord**. Panel a) bathymetric image of the study area, with location of the two common shots (site A and B). The seabed morphology clearly shows indicators of multiple marine landslides deposits. The gas front area is shaded. Panel b) migrated Boomer seismic line crossing the gas front. Panel c and d: Seismic gather respectively of site A and B. Note how the strong receiver ghost reflections cross the event bed reflection in site A.

4.3.3.1 Acquisition design and background information

Here we apply the elastic FWI to two UHF multi-channel seismic datasets acquired on a marine slope prone to shallow landsliding, in the Sørfjorden side-fjord near the town of Finneidfjord (Norway). The extensive suite of high frequency geophysical, geotechnical and geological data in the study area (e.g. Steiner et al., 2012) identifies a composite 50 cm thick clay-rich bed with low stiffness, low density and high overpressure ratio that lies at shallow depth within the background silty-clay sediments (Vanneste et al., 2012; Vardy et al., 2012; Vardy, 2015). This layer has been recognised as the failure plane for multiple submarine landslides from the last few decades and is is thus referred to as *event bed* (L'Heureux et al., 2012; Steiner et al., 2012; Vanneste et al., 2012, 2015; Vardy et al., 2012). The

saturation state of the event bed changes across the basin, from a water-saturated zone in the north to a gas-bearing area to the south (Vardy et al., 2012; Morgan et al., 2014).

The seismic source is a Boomer wide-band electro-acoustic plate with an effective bandwidth spanning from 0.2 to 2.5 kHz. The acquisition system is a 60-channel streamer with 1.0 m group spacing and maximum offset equal to 72 meters. A single receiver group has a length of 1 m and is made up by 7 elements. Both source and receiver group wavenumber filters have been included in the modelling. The receiver ghost reflections are a strong source of coherent noise in the data (Fig. 4.11), particularly at site A, where the seafloor ghost reflection has higher energy than the event bed reflection and the respective traveltimes intersect. We include the receiver ghosts in the forward model by integrating the one dimensional solver with a custom-built frequency-wavenumber filter that accounts for the strong variation of the streamer depth and sea-surface reflection coefficient with offset (Provenzano et al., 2017).

Because of the availability of a reliable ground-truth, the challenging nature of the seismic data and the geohazard implications, this is an excellent case study to test the potential of UHF seismic inversion.

4.3.3.2 Elastic FWI and ground-truthing

We apply the inversion at two key locations, outside (Site A) and inside (Site B) the gas front (Fig. 4.11), with the aim to locate and characterise the event bed, and quantify the changes in partial gas saturation. P-wave velocity and bulk density measurements from a *Multi Sensor Core Logger (MSCL)* core proximal to Site A (Fig. 4.11), provide the low-frequencies to build a reliable starting model; therefore the computational effort in this section will be devoted to the identification of geohazard-relevant features. The one-dimensional approximation is justified by the almost plane-parallel geometry of the shallow reflectors in the pre-stack depth-migrated (PSDM) image (Fig.4.11). Preliminary analysis of the available reflection angle range suggests that, due to the short aperture of the data compared to the target depth, density and P-impedance can't be resolved independently (Provenzano et al., 2017), therefore a full elastic (Z, ν, ρ) multi-parameter inversion would be heavily ill-posed. As shown in Igel et al. (1996)

and Provenzano et al. (2016), a more appropriate parametrisation in this case is (Z, ν).

	One parameter (Vp)	Elastic (Z, ν)
S(m)	-	0.15
Number of variables	-	120
Mutation prob.	-	0.001
Crossover prob.	-	0.6
Number of individuals	-	420
Number of generations	-	100
Number of runs	-	50

Table 4.2: **Site A inversion parameters**. User-defined genetic algorithm parameters for the simultaneous elastic inversion.

	One parameter (Vp)	Elastic (Z, ν)
S(m)	0.2	0.2
Number of variables	35	70
Mutation prob.	0.01	0.001
Crossover prob.	0.6	0.6
Number of individuals	320	500
Number of generations	120	150
Number of runs	10	50

Table 4.3: **Site B inversion parameters**. User-defined genetic algorithm parameters for the first-stage P-wave velocity inversion, and the following preconditioned simultaneous elastic inversion.

Inversion parameters at site A are presented in Table 4.2. The relatively narrow range of expected values allowed for the simultaneous (Z, ν) inversion to converge to a satisfactory solution. The median model attains an excellent match with the MSCL acoustic impedance within the seismic resolution (Fig. 4.12), capturing the composite structure of the low-impedance anomaly between 3.5 and 4.0 m depth. The results suggest that the strongest heterogeneity at the event bed

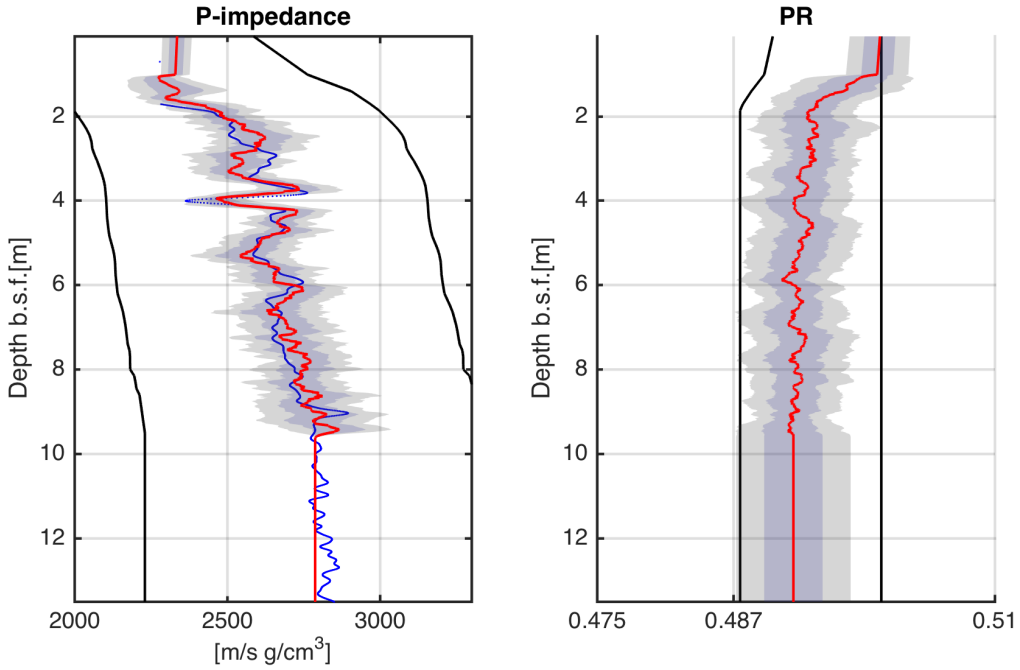

Figure 4.12: **Site A elastic inversion results.** Median (solid red) and 66 - 95 % confidence intervals (respectively blue and grey) obtained from 50 independent inversion runs; MSCL Impedance measured in-situ (blue); search boundaries (solid black lines).

is the bottom interface, whereas the top one is probably a graded boundary at the seismic resolution. The Poisson's ratio model, on the other hand, does not contain important discontinuities, most probably because of the low-sensitivity of reflection data to changes in shear properties in the range of non-lithified sediments (≥ 0.49; Hamilton, 1970; Mallick and Dutta, 2002; Provenzano et al., 2017). In Fig. 4.13 we compare the real seismogram to the computed one for the best-fit model; note that the small amplitude negative polarity reflection associated with the event bed is correctly represented in the inversion, despite the strong receiver ghost, which overlaps the up-going reflection within a significant range of offset. The small reduction of normalised offset-dependent misfit between the starting low-frequency model and the FWI-solution, is explained by the low energy of the subsurface reflections compared to the primary and ghost seafloor reflections.

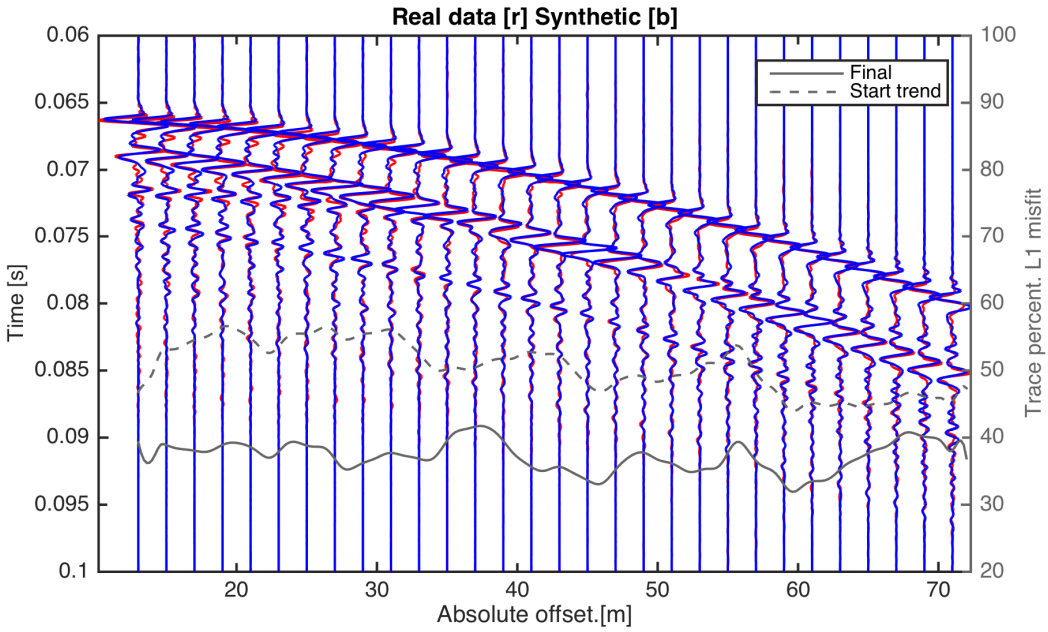

Figure 4.13: **Site A elastic inversion offset-dependent misfit**. Real seismogram (red), Synthetic seismogram (blue) for the median model after elastic FWI. Overlaid, offset-dependent trace-normalised L1 misfit for the starting low-frequency model (dash-dot grey) and the final FWI-model (solid grey).

The inversion at site B is performed using the parameters summarised in Table 4.3. Because we want account for the possible presence of free gas, broader (Z, ν) search windows are required to allow for the inversion to converge close to the true elastic model; due to the gas saturation, P-impedance values close-to or lower-than the water column acoustic impedance are expected, and Poisson's ratio can span a broad range of values (Anderson and Hampton, 1980a; Ostrander, 1984; Tóth et al., 2014). Attempts to invert simultaneously Z and ν failed to converge to a meaningful solution, thus the two-stage preconditioned strategy is applied to reduce the size of the model space. The first stage of P-impedance inversion places the event bed between 7.5 and 8.0 m below the seabed; this model is then smoothed with a correlation length of 50 cm (Fig. 4.14), and used to precondition the range-width of the elastic inversion. The final model shows a drop of Z at 7.4 m b.s.f., with a 95% confidence interval reaching values below $600 m/s \cdot g/cm^3$, correlated to a decrease in ν. The confidence intervals for ν are broad, and the solution for Z shows a probably non-physical long wavelength harmonic trend, as a consequence of the limited sensitivity of the short-offset reflection data in a relatively deep-water environment (Mallick and Dutta, 2002; Operto et al., 2013). Nevertheless, the FWI univocally identifies a shallow horizon with reduced bulk modulus, consistent with the presence of free gas in the pore space. The solution models after each stage account for a significant reduction of the offset dependent misfit in Fig. 4.15 compared to the initial state of information, and the final computed seismogram shows an excellent match with the real one.

4.3.3.3 Can we quantify the free-gas content?

As an example application, we use the FWI results to estimate a partial gas-saturation distribution in the sediment column. The presence of small amounts of free gas in the pore space is expected to produce a strong increase in the bulk sediment compressibility, having, on the other hand, little effect on its shear modulus (Mavko et al., 2009). Therefore, a drop of P-wave velocity associated with a decrease of Poisson's ratio is expected (Aki and Richards, 2002). Also, gas-bubble resonance produce frequency-dependent changes in attenuation and P-wave velocity, which are significant at frequencies higher than the characteristic

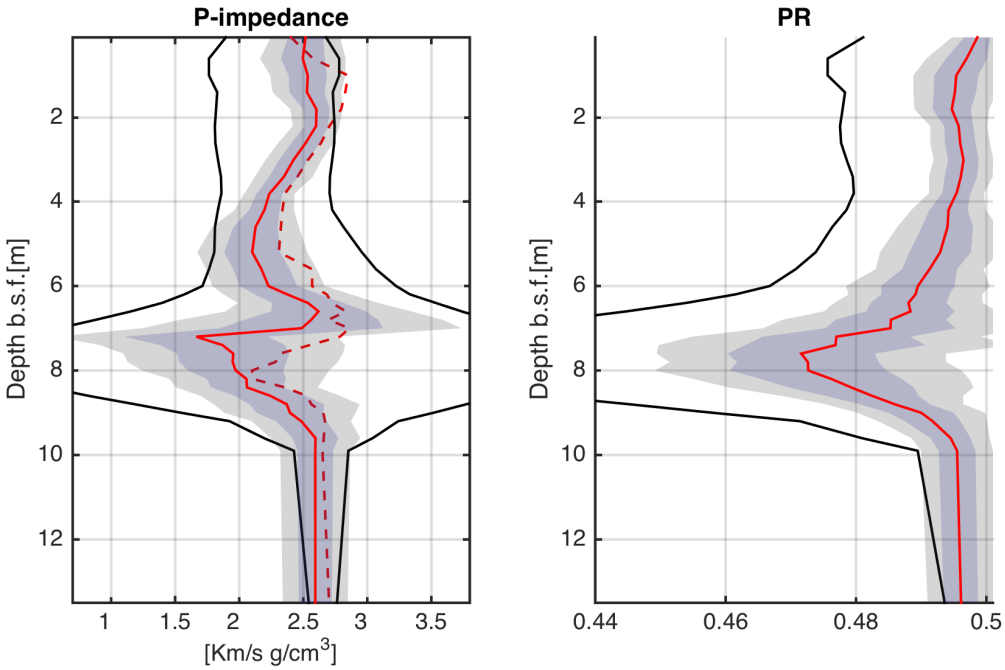

Figure 4.14: **Site B elastic inversion results.** Median model (solid red) and 66 - 95 % confidence intervals (respectively blue and grey) obtained from 50 independent inversion runs; search boundaries (solid black lines); the red dashed line is the smoothed P-impedance model from the single-parameter inversion, whose local rate of change is used to precondition the width of the search range for the elastic inversion.

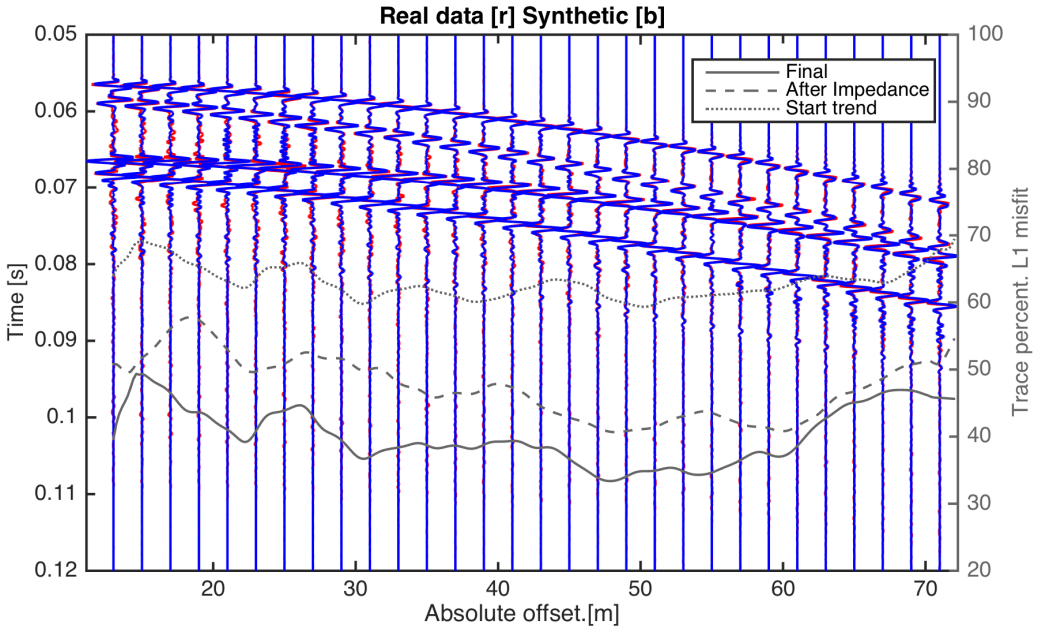

Figure 4.15: **Site B elastic inversion offset-dependent misfit**. Real seismogram (red), Synthetic seismogram (blue) for the final model after elastic FWI. Overlaid, offset-dependent trace-normalised L1 misfit for the starting low-frequency model (dash-dot grey), the final Vp model (dash grey), and the final FWI-model (solid grey).

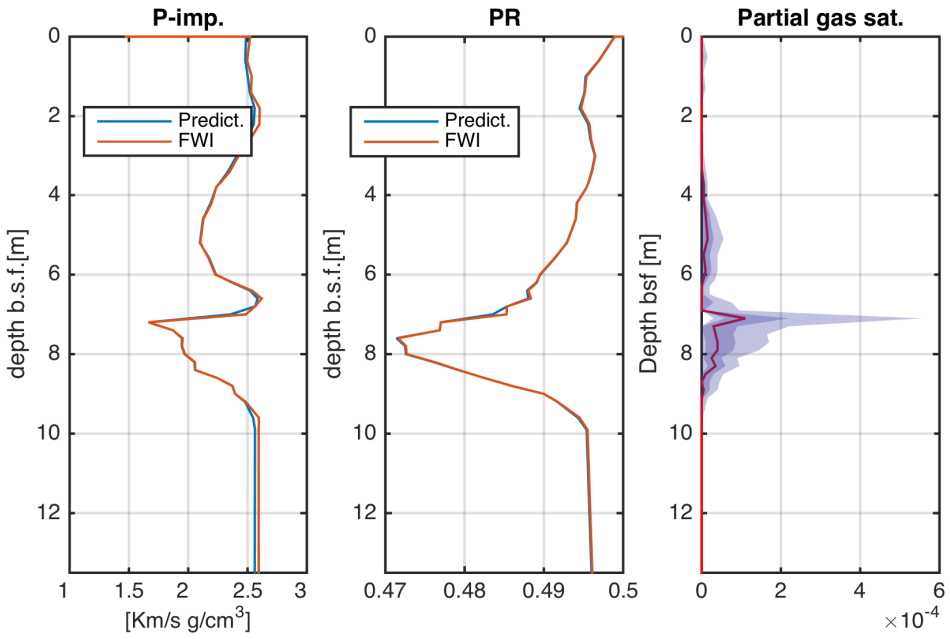

Figure 4.16: **Site B. Partial gas saturation from Z and ν.** P-impedance and Poisson's ratio predicted (blue) using Anderson and Hampton (1980b) model are compared with the FWI-solution (red). In the right panel, log-scale partial gas saturation estimated by fitting the median (red), and the 66 % (blue) and 95 % (grey) confidence limits.

resonance frequency of the dominant bubble size (Anderson and Hampton, 1980a; Tóth et al., 2015).

Under the assumption that bulk mechanical effects dominate in our frequency band (0.2-2.5 kHz; Riedel and Theilen, 2001), we apply the geo-acoustic model by Anderson and Hampton (1980b) to estimate the partial gas saturation (Tóth et al., 2014). The model accounts for the increase of compressibility due to the presence of gas in the pore space, with respect to a water-saturated sediment at a given hydrostatic pressure. The model predicts the three-phase medium bulk modulus (K_m), and the shear modulus (μ), from which the (Z,ν) couple at each depth can be derived assuming an elastic isotropic mechanics (Mavko et al., 2009). The partial gas-saturation value is obtained by iteratively minimising the difference between the FWI-model and the predicted one.

Fig. 4.16 shows the results obtained at site B by fitting the FWI results within the confidence intervals, and compares the FWI-solution with the elastic

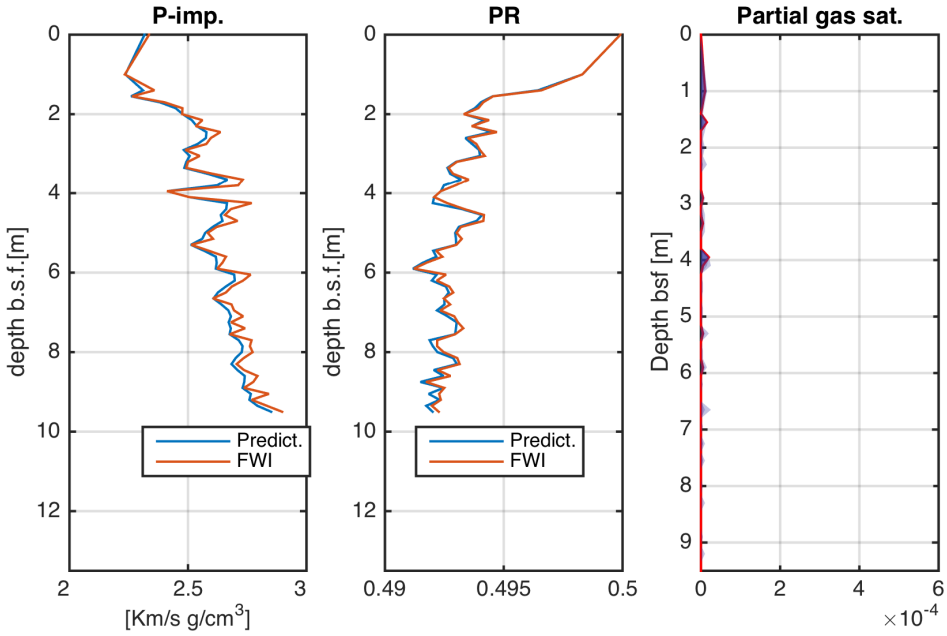

Figure 4.17: **Site A. Partial gas saturation from Z and ν.** P-impedance and Poisson's ratio predicted (blue) using Anderson and Hampton (1980b) model are compared with the FWI-solution (red). In the right panel, log-scale partial gas saturation estimated by fitting the median (red), and the 66 % (blue) and 95 % (grey) confidence limits.

properties predicted by the geo-acoustic model. A free-gas anomaly is placed at 7.5 m below the sea-floor, with a partial gas saturation confidence area in the order of 0.03%; this in good agreement with previous results obtained independently at the same site employing different high-resolution seismic sources with dissimilar inversion techniques (Vanneste et al., 2013; Morgan et al., 2014). The same procedure applied to site A resulted in a gas saturation one order of magnitude lower (Fig. 4.17).

4.3.4 Discussion

The real case study demonstrates stable results, in excellent agreement with the geotechnical ground-truth at the seismic resolution. This makes a strong case for the use of seismic data as a remote characterisation tool for decimetric-scale features relevant to geohazard. In general, even when the final solution confidence intervals are broad, as in site B, the stochastic inversion succeeds at improving the a-priori state of information about the subsurface, in a purely data-driven way. In Site A, the solution for P-impedance reproduces the MSCL Vp data, almost perfectly within the seismic resolution, constituting a virtual *in-situ* elastic log. In site B, our structure-preconditioned strategy is fundamental to obtain convergence in the simultaneous multi-parameter inversion. The (Z, ν) model univocally identifies a shallow horizon showing a typical signature of gas saturation, as expected from the available independent data.

In the real data example, the availability of a P-wave velocity profile, measured on a core proximal to the inversion site, allowed us to design an accurate search range for the stochastic optimiser. When this is not the case, low-resolution P-wave models obtained from the reflection kinematics (e.g. from NMO analysis), can be used for the purpose. However, especially in sites with a strong shallow velocity gradient, inaccuracy in the semblance-derived starting model could bias the genetic algorithm away from the true broadband model. On the other hand, a uniform search range, between the maximum and the minimum expected velocities, significantly increases the number of samples required for an effective exploration of the model space (Tarantola, 2005), therefore reducing the chances of convergence within a feasible computing time (*curse of dimensionality*, e.g.; Sajeva et al., 2016, 2017). Thus, we suggest that reflection moveout analysis can be used as a quick method to narrow the range of possible earth models, and that

this should be combined with an appropriate seismic inversion strategy. In the synthetic example, the proposed decoupled parametrisation of the P-wave velocity model, combined with a misfit criterium based on the instantaneous phase (Jimenez-Tejero et al., 2015), proved to be able to compensate for ill-constructed search ranges, attenuating the bias of the starting model on the solution.

In the preconditioned elastic stage, a robust relationship among the long wavelength of the elastic parameters is only needed to build the search window, and can reflect the expected sediment type (Hamilton, 1970; Richardson and Briggs, 1993), or previous information about the recent geological history of the study area (e.g. Vardy et al., 2017). Detectable converted S-wave and post-critical reflections would probably allow us to constrain independently the shear properties long wavelengths, but this is often not the case in short-offset marine data (Kormendi and Dietrich, 1991; Igel et al., 1996; Vardy et al., 2017).

The elastic stage of reflection FWI aims at estimating the high-frequency elastic structures responsible for the offset-dependent seismic reflectivity, which are indicators of local anomalies in sediment fabric, lithology, or partial fluid saturation. The constraint posed by reflection data on the elastic parameters is highly hierarchical (Tarantola, 1986; Igel et al., 1996), namely higher for P-wave impedance, whereas independent density anomalies can only be detected if wide reflection angles are available ($> 40°$; Provenzano et al., 2017). Sensitivity to differential changes of P- and S- waves in non-lithified, water-saturated media is also low, because they span a narrow Poisson's ratio range, with little footprint on the AVO response (Mallick and Dutta, 2002; Provenzano et al., 2017). This explains, in the synthetic example, the lower accuracy of the reconstructed shear and density profiles compared to the P-wave impedance result, and, in the real data, the absence of significant Poisson's ratio interfaces correlated to the event bed. By contrast, small amounts of gas in the pore space correspond to greater Poisson's ratio anomalies, as in site B (Ostrander, 1984; Mallick and Dutta, 2002).

The aforementioned sensitivity issues in the multi-parameter elastic space can in principle be quantitatively estimated from the posterior model ensemble as solution non-uniqueness. Several techniques have been developed in the literature in order to make the evolutionary optimiser a proxy to Bayesian statistics (e.g., Sen and Stoffa, 1992, 1996; Sambridge, 1999; Aleardi and Mazzotti, 2017). However, it is beyond the scope of this paper to address the issue of an effective importance sampling of the model space using a genetic algorithm. The approach of

this work is to perform multiple inversion runs, starting from independent random model populations (Sen and Stoffa, 1992; Vardy, 2015), in order to estimate the reproducibility of the solution without the bias of genetic drift and model inter-dependency (e.g. Vardy, 2015).

In the real case study, the partial gas saturation boundaries estimated from the elastic model confidence intervals are consistent with previous independent geophysical studies (e.g. Vanneste et al., 2013; Morgan et al., 2014). While the gas saturations at this site have not been measured in situ (through pressure coring, or similar), the consistency amongst different geophysical methods is promising, especially because of the potential destabilising effect of gas-pockets within near-seafloor beds (e.g. Vanneste et al., 2013). However, similarly to the cited works, the compressible-gas model used (Anderson and Hampton, 1980b) does not account for gas bubble resonance. As shown by Tóth et al. (2015), the validity of this assumption is highly dependent on the dominant gas bubble size, which exerts an important influence on apparent P-wave velocity dispersion and attenuation (Anderson and Hampton, 1980a). Such frequency-dependent effects are negligible only at frequencies lower than the gas bubble characteristic frequency (Wilkens and Richardson, 1998). Since the bubble size is not known to the accuracy required to rule out P-wave velocity dispersion at the upper end of the spectrum of our data ($\simeq 2.0-3.0kHz$), this approach could have underestimated the true gas saturation value, and should therefore be considered a lower bound.

4.4 Conclusions

We proposed a dedicated strategy for the pre-stack waveform inversion of ultra-high-frequency marine reflection data, based on a genetic algorithm with a carefully constructed model space, and demonstrated the potential of the method as a tool for the remote characterisation of decimetric thickness layers.
In summary:

1. We have demonstrated that a genetic algorithm optimisation is not inherently robust against inaccurate starting models, and requires appropriate model parametrisation and a careful choice of the objective function. A spectrally-decoupled exploration of the model space, combined with a

complex-trace based objective function has been shown to increase robustness against inaccurate a-priori distribution, e.g. derived from inaccurate pickings in reflection moveout analysis.

2. We have also shown that this robust P-wave velocity model can be used to precondition the multi-parameter elastic inversion, in order to reduce the size of the model space in high-dimensionality parametrisations. This allows us to obtain a complex elastic model starting from little a-priori information.

3. A real case study has confirmed the potential of stochastic seismic inversion as a tool for the remote characterisation of decimetric-scale structures useful for shallow geohazard assessment. A sedimentary bed correlated to the failure depth of multiple landslides in the study area has been identified. Signatures of changes in its partial gas saturation have been detected in the elastic model. Within the seismic resolution and sensitivity, an excellent match with the ground truth has been obtained

The proposed strategy for engineering-scale FWI is thus a precious practical tool to complement information from bathymetry, sub-bottom profilers, cores and CPTUs for shallow geohazard assessment, reducing the need of expensive and time consuming geotechnical sampling campaigns in areas prone to shallow marine landsliding.

Acknowledgments

The work presented here was funded through the SEABED consortium with additional funding through the International Centre for Geohazards (ICG). The authors would like to thank Antonis Zervos, Tim Minshull and Hector Marin Moreno for the fruitful discussions regarding inversion and geomechanics. The field data preconditioning was performed using a combination of Landmark's ProMAX software, MatLab, and Seismic Unix. The forward modelling was performed using the MIT OASES algorithm. All other processing used custom-written algorithms. The authors acknowledge the use of the IRIDIS High Performance Computing Facility, and associated support services at the University of Southampton, in the completion of this work.

5

Can we detect in-situ instability conditions from shallow marine reflection seismic data?

Summary

[1] In this chapter, we compute synthetic UHF seismic reflection data from a set of synthetic marine slopes in which disequilibrium compaction is induced during deposition. Rather than simulating realistic slope conditions, our goal is to showcase seismic reflection data as a tool for the remote detection of submetric scale, potentially destabilising effective stress reductions, in a variety of permeability structures and sedimentation rates. We simulate continuous deposition of sediment on a consolidating infinite marine slope, using combinations of sedimentation rate and permeability distribution representative of different depositional environments in which shallow landsliding is observed (Masson et al.,

[1]Section 5.2 of this chapter is based on the formulation developed in Zervos (2014), generalised for heterogeneous models

2006). A time-evolving acoustic impedance model is derived from porosity using an empirical relationship reasonable for shallow marine sediments (Vardy, 2015), and multi-channel UHF seismic reflection datasets are computed. The seismograms show the development of negative polarity reflections generated at lower-impedance horizons, corresponding to stratigraphic layers with localised disequilibrium compaction. The amplitude of the reflections is a function of the excess pore pressure distribution, which in turn depends on the permeability structure and the sedimentation rate. The detectability of destabilising effective-stress reductions is limited by the signal-to-noise ratio, resolution and sensitivity of the data. The characteristics of the computed seismograms, however, suggest that seismic inversion can be applied successfully, within the aforementioned limitations. Provided that the empirical porosity-acoustic impedance relationship is representative of the rock physics of the medium, the inverted model can then be used to derive porosity. This poses constraints on the in-situ excess pore pressure distribution, providing valuable information about the effective stress conditions of the slope. In turn, the effective stress profile for a slope directly influences its stability, controlling the level of stress required to trigger failure and lateral movement of material.

5.1 Introduction

Background

Submarine landslides involve the movement of thousands of km^3 of sediments (Halflidason et al., 2005; Masson et al., 2006) and are spread worldwide in a variety of depositional environments (Garzaglia et al., 2005). Hazards associated with modern submarine landslides include human fatalities and damage to shoreline and/or offshore engineering structures (Masson et al., 2006; Shanmugam, 2015). Unlike their land equivalents, they are observed on very low-angle slopes (even below 2°) with relatively low sedimentation rates (Urlaub et al., 2012; Madhusudhan et al., 2017), and are recognised as a cause of tsunamis that can travel for 100s km and therefore extend the hazard over huge areas (Skvortsov and Bornhold, 2007; Conway et al., 2012).

Localised development of pore overpressure, i.e. pore pressure higher than hydrostatic, has been commonly regarded as a preconditioning factor in the oc-

currence of slope failure (Leynaud et al., 2007; Flemings et al., 2008; Dugan and Sheahan, 2012). Sediment beds with low effective stress are believed to act as glide planes of translational slides in both continental shelf and near-shore contexts (L'Heureux et al., 2012; Vanneste et al., 2013; Madhusudhan et al., 2017). Although numerical modelling studies suggest that overpressure development by sedimentary loading alone is not likely to cause submarine landsliding under realistic sedimentation rates (Urlaub et al., 2012), it can however favour the occurrence of slope failure in the presence of transient loading caused by either natural causes, such as earthquakes or gas-hydrate dissociation (Dugan and Flemings, 2000; Masson et al., 2006; Stigall and Dugan, 2010; Madhusudhan et al., 2017), or anthropic, e.g. industrial blasting or piling (Masson et al., 2006; Vanneste et al., 2013, 2015).

The evaluation of in-situ stability conditions of the shallow sub-seafloor is strongly reliant on direct sampling of the seabed via cores and CPTUs (Stoker et al., 2009; Colombo et al., 2016; Madhusudhan et al., 2017), which provide centimetre-to-millimetre vertical resolution data, but are limited by logistics to a coarse spatial coverage. Unlike basin scale research (Binh et al., 2009; Marin-Moreno et al., 2012, 2013), non-invasive estimations of pore-pressure distribution are not commonly employed in offshore geotechnics, and very rarely link the quantitative interpretation of geophysical data to effective stress conditions.

Seismic field exploration methods can provide important constraints on the effective stress conditions of the the shallow subsurface, by virtue of the dependency of the dynamic elastic moduli, and hence acoustic impedance, on the overpressure distribution (Dugan and Sheahan, 2012; Marin-Moreno et al., 2012, 2013; Vardy, 2015), and have the potential to cover large areas in a quick and cost-effective way. Ultra-high-frequency (0.2-12.5 kHz) seismic surveys provide a sub-metric to centimetric resolution in shallow marine environments, and a penetration depth in the order of a few tens of m; this has proven to have the potential to identify and characterise sedimentary beds acting as preconditioning factor of submarine slides (Vardy et al., 2012; Vanneste et al., 2015).

The lower vertical resolution compared to direct soil sampling, makes the seismic data unfit for the detection of millimetric features that can be key in preconditioning slope instability (Viesca and Rice, 2012; Madhusudhan et al., 2017), whereas other factors contributing to slope stability, such as plasticity (Gordon and Flemings, 1998), are not part of the relevant physics of wave propagation.

Permeability distribution is loosely constrained by the attenuation characteristics of the medium. Though a reliable attenuation model can be obtained from broadband data (> 5 octave; Pinson et al., 2008), this hardly attains the spatial resolution necessary to capture model heterogeneities at the scale required by slope stability characterisation.

Nevertheless, because of the sensitivity to the low-stress elastic response of the sediment at a sub-metric scale (Dugan and Sheahan, 2012; Vardy et al., 2017), UHF seismic data can contribute to identify areas preconditioned to landsliding, where overpressure build-up is a factor in the in-situ stability conditions (Vanneste et al., 2015). Thanks to the time-effective acquisition over large areas, and the non-destructive nature, this has the potential to integrate with bathymetric and geological data in optimising the design of higher resolution geotechnical data acquisition campaigns (Carlton et al., 2017).

Outline of the chapter

We present synthetic tests showcasing the use of marine seismic data as a tool for the remote sensing of disequilibrium compaction. We simulate the acquisition of ultra-high-frequency multi-channel reflection seismic data, during the sedimentary loading of an infinite marine slope with permeability layering (Bethke, 1985; Huang and Griffiths, 2010). The thickness of the model is in the order of tens of m and the deposition interval in the order of $1 - 10ka$ (*kilo annum*=1000 years).

We first outline the mathematical model and numerical solution to the Terzaghi consolidation equation (Gibson, 1958; Powrie, 2002; Huang and Griffiths, 2010) for a horizontally stratified medium, with variable sedimentation rate; the formulation includes the moving sediment-water boundary originally developed by Zervos (2014).

We explore different combinations of sedimentation rate and permeability layering, examples of sedimentary structures that can be observed in a variety of geological settings: (1) Peri-glacial, with silty-clayey deposition, interrupted by rapid sedimentation of a few-decimetres thick low-permeability composite layer [e.g. Finneidfjord, Norway , Vardy et al. (2012); Vanneste et al. (2015)] (2) Deltaic, with high permeability contrast between sandy sediments and clay beds, and high-sedimentation rate [e.g. Gulf of Mexico, Flemings et al. (2008); Long et al. (2008, 2011)] (3) Continental shelf, with coarsening upward silty-clayey

sedimentary sequences [e.g. AFEN (Atlantic Frontier Environmental Network) landslide complex, Madhusudhan et al. (2017)]. The evolution of overpressure ratio, porosity and factor of safety is then presented for each of the sedimentary structures considered.

The presence of low-permeability beds in the sedimentary column produces disequilibrium compaction and thus deviations from the normally consolidated effective stress profile. This in turn induces stratigraphic variations in porosity, which can be linked to acoustic impedance using an empirical relationship valid for shallow marine sediments (Hamilton, 1970; Richardson and Briggs, 1993; Vardy, 2015). Noise-contaminated seismic data are then generated with a frequency content and acquisition geometry typical of shallow marine reflection data.

The seismic data characteristics, along with the possibility to apply seismic inversion and infer in-situ effective stress conditions, are discussed. Within the limitations of the simple geotechnical model used, the results support the use of multi-channel seismic reflection data to identify over-pressure anomalies, on the road to an integrated geophysical-geotechnical approach in the characterisation of landslide geohazard.

5.2 Consolidating infinite slope modelling

In this work, we use a one-dimensional consolidating elastic slope model (Gibson, 1958; Huang and Griffiths, 2010), integrated with a moving sediment-water interface during deposition (Zervos, 2014). The slope is assumed to be under hydrostatic pore pressure conditions when loading starts and soil particles are deposited over time according to a time-varying sedimentation rate. Due to the added load, the slope will consolidate, with transient vertical pore fluid flow dissipating the excess pore pressure generated (Gibson, 1958). The presence of low permeability layers within the sediment column can inhibit this process and lead to disequilibrium compaction and localised over-pressure build up; the consequent reduction of the effective stress facilitates slope failure by reducing the shear resistance of the sediment (Huang and Griffiths, 2010; Dugan and Sheahan, 2012; Marin-Moreno et al., 2012).

During deposition, the seafloor position potentially changes due to the new material being deposited, and overpressure can develop within the new sediments. Hence sedimentation is accounted for not only as an external load, but also as

a part of the consolidating slope. The problem is one-dimensional, governed by water mass balance considerations and a linear elastic stress-strain response of the soil skeleton. The solid grains are assumed incompressible, hence load-induced deformations are entirely attributed to variations of the pore space volume, which lead to a time evolution of permeability, according to an exponential relationship between intrinsic permeability and porosity (Binh et al., 2009). Thermo-chemical reactions, such as dehydration and cementation effect, that play an important role in basin scale compaction studies (Gordon and Flemings, 1998; Marin-Moreno et al., 2012, 2013; Colombo et al., 2016), are also unlikely to be a factor in shallow, low-temperature sediments (Dugan and Sheahan, 2012), and are therefore not accounted for in the modelling. In this section, we lay out the fundamental equations describing the model and the boundary conditions. Those are derived from the original formulation developed by Zervos (2014) for a homogeneous slope, and generalised to account for a time and space varying permeability.

5.2.1 Mathematical formulation

5.2.1.1 Model setup and definitions

We consider a sediment column of unit weight γ on an infinite slope of angle θ, submerged under hydrostatic conditions (Figure 5.1). The thickness of the sediment, measured normal to the slope from the impermeable bedrock to the seafloor, is D. We isolate a block of length $2l$ along the slope and depth $(D - z)$, where z is the distance of the base of the block from the the base of the column, measured normal to the slope (Fig. 5.2). The average vertical depth of the layer's surface from the sea surface is d_0. The following forces and stresses act on the block (Fig. 5.2):

- Its own weight, $W = 2l(D - z)\gamma$, where we assume the soil unit weight γ to be uniform for simplicity.

- The average pressure of the overlying body of water, $p_0 = \gamma_w d_0$; this varies from p_L upslope to p_R downslope. By integrating the force along the slope length, we obtain the resultant normal force $F_n = 2lp_0$ acting at the surface of the block.

- The average normal stress σ_z and shear stress τ at the bottom of the block.

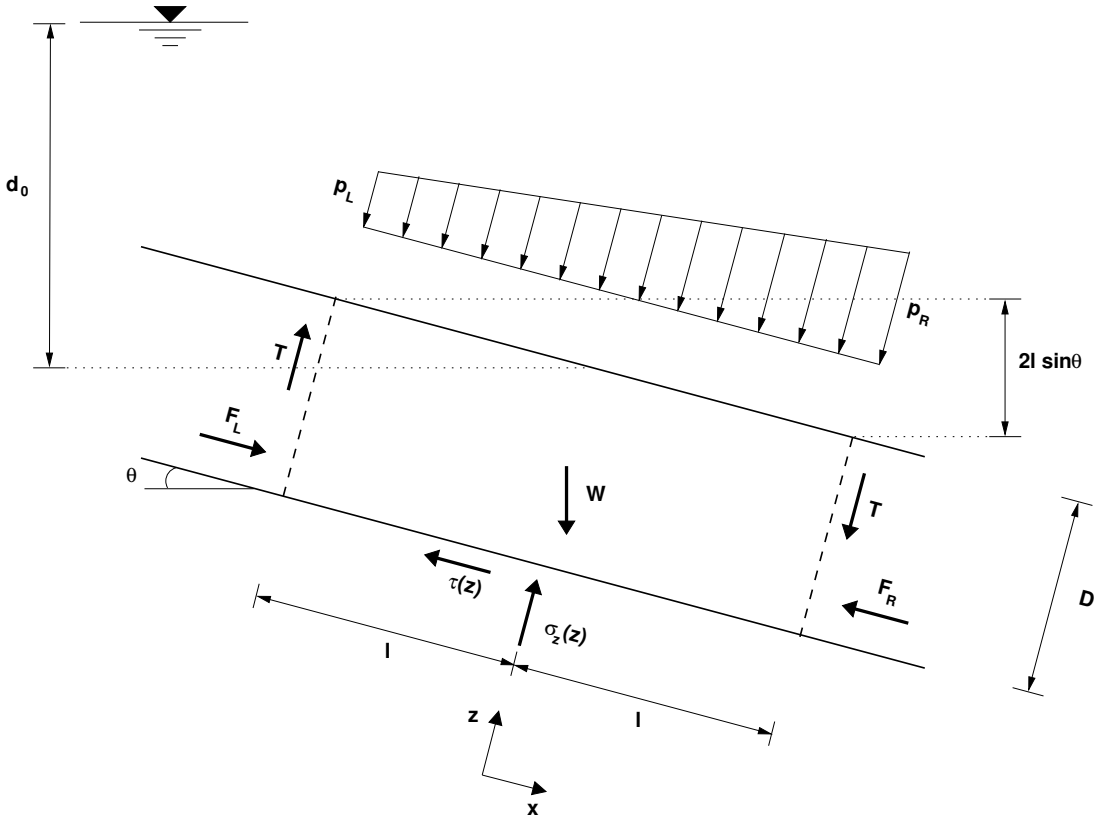

Figure 5.1: **Model setup 1**. A submerged infinite slope. From Zervos (2014).

- Along-the-slope forces F_L and F_R and shear forces T, acting on the left and right ends of the block due to interaction with the soil further upslope and downslope respectively.

The right side of the block is deeper under water than the left side, hence higher pore water pressure will act on the right side than on the left, but that doesn't affect the effective stress conditions (Zervos, 2014). Infinite slope conditions suggest that the effective stress acting on the left and right sides should be equal, i.e that difference in pore pressure between the left and the right side of the block equals the respective difference in total stress. From Figure 5.1;

$$F_R - F_L = (2l(D - z)\sin\theta)\,\gamma_w \tag{5.1}$$

where the additional pore pressure is $2lsin(\theta)\gamma_w$ and multiplication by the surface length $(D-z)$ yields the extra-force on the lateral surface. The total forces acting on the block are shown in Figure 5.2. Equilibrium in the x and z directions

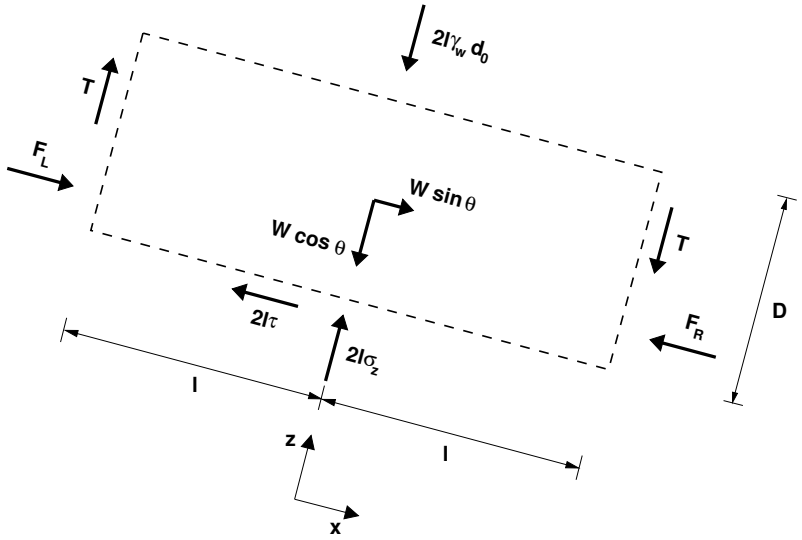

Figure 5.2: **Model setup 2**. Forces acting on a block of a submerged infinite slope. From Zervos (2014).

requires that the sum of the total force components is zero. Taking into account Eq. 5.1:

$$\Sigma F_z = 2l\sigma_z - (2l(D-z)\gamma)\cos\theta - 2l\gamma_w d_0 = 0 \tag{5.2}$$

$$\Sigma F_x = 2l\tau + F_R - F_L - (2l(D-z)\gamma)\sin\theta = 0 \tag{5.3}$$

Rearranging to solve for the normal and shear stress, we obtain:

$$\sigma_z = \gamma(D-z)\cos\theta + \gamma_w d_0 \tag{5.4}$$

$$\tau = (\gamma - \gamma_w)(D-z)\sin\theta \tag{5.5}$$

The average pore pressure and effective stress at the bottom of the block are calculated as:

$$p = \gamma_w(d_0 + (D-z)\cos\theta) \tag{5.6}$$

$$\sigma'_z = \sigma_z - p = (\gamma - \gamma_w)(D-z)\cos\theta \tag{5.7}$$

The mobilised strength at the base of the block is:

$$\tan\phi'_{mob} = \frac{\tau}{\sigma'_z} \tag{5.8}$$

Substituting Eqs. 5.5 and 5.7, we obtain:

$$\tan \phi'_{mob} = \frac{(\gamma - \gamma_w)(D - z)\sin\theta}{(\gamma - \gamma_w)(D - z)\cos\theta} = \tan\theta \tag{5.9}$$

We now consider the problem of Figure 5.3, where continuous deposition and consolidation make the thickness of the sediment column vary with time, in other words $D = D(t)$. Figure 5.4 shows an infinitesimal layer of the consolidating slope, with thickness dz; u_x and u_z are the displacement along the x- and z-axes respectively, and compression is taken positive. The following definitions and relationships will be used in the formulation of the transient problem:

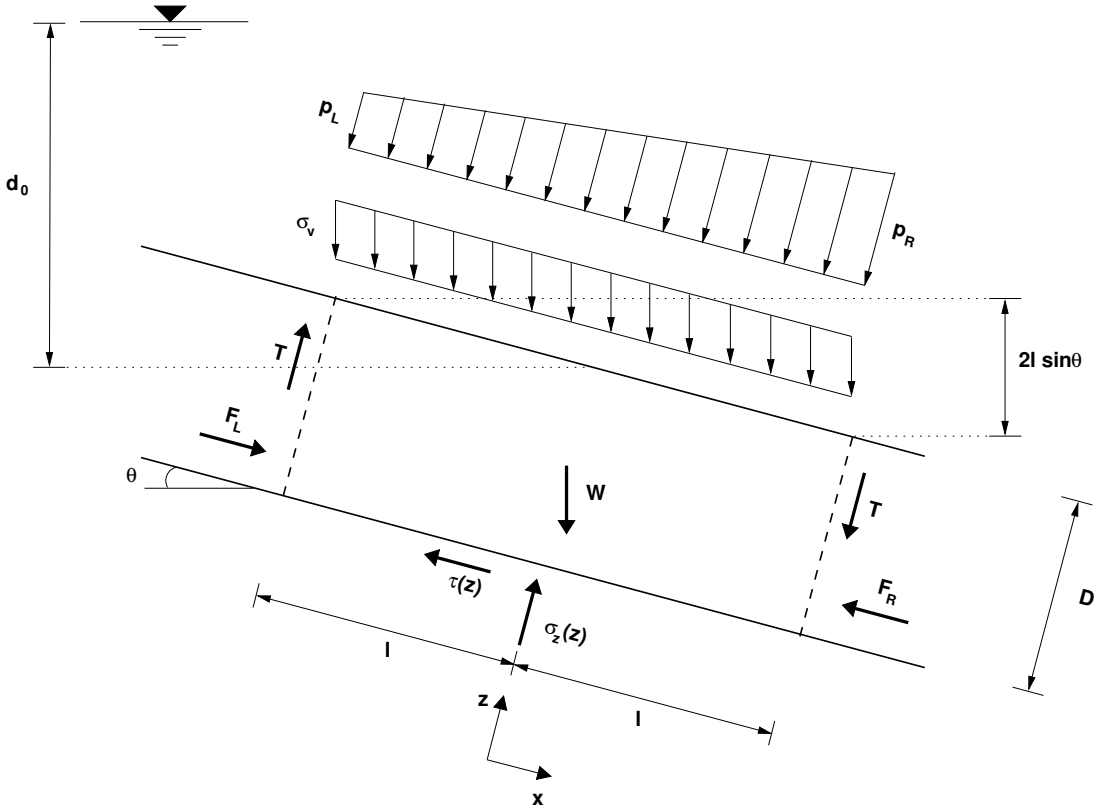

Figure 5.3: **Model setup with load 1**. A submerged infinite slope with vertical load. From Zervos (2014).

- Pore pressure: $p = p_h + p_e$, where p_h the hydrostatic component and p_e the excess pore pressure.
- Excess head: $h = \dfrac{p_e}{\gamma_w}$.

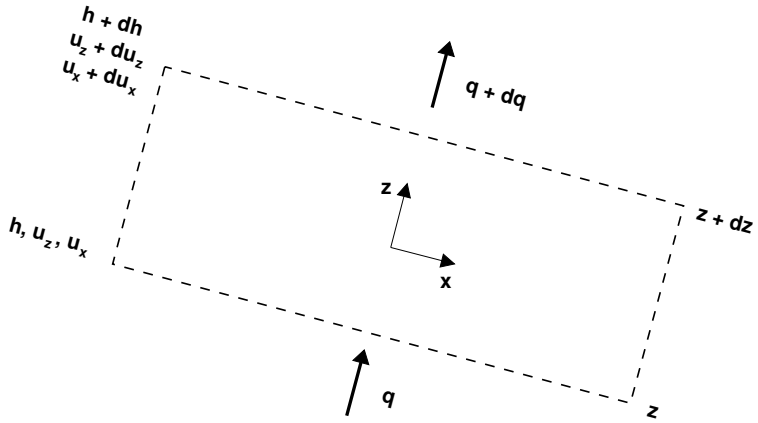

Figure 5.4: **Model setup with load 2**. An element of a consolidating slope. From Zervos (2014).

- Effective stress: $\sigma'_z = \sigma_z - p = (\sigma_z - p_h) - p_e$.
- Overpressure ratio: $\lambda^* = \dfrac{p_e}{\sigma_z - p_h}$. I.e. the ratio between the excess pore pressure and the effective stress under hydrostatic conditions.
- Strain normal to the slope (equal to volumetric strain): $\epsilon_z = \epsilon_{vol} = -\dfrac{\partial u_z}{\partial z}$.
- One-dimensional soil stiffness: $E'_0 = \dfrac{d\sigma'_z}{d\epsilon_z}$, where $\sigma'_z = \sigma'_z(\epsilon_z)$.
- Porosity: $n = V_v/V_{tot}$. Void ratio: $e = V_v/V_s \rightarrow e = \dfrac{n}{1-n} \rightarrow n = \dfrac{e}{e+1}$
- Darcy's law: $q = -kA\dfrac{\partial h}{\partial z}$, where q the volumetric flow-rate through the infinitesimal layer, k the kinematic permeability (Powrie, 2002) and A the area available for flow.

5.2.1.2 Derivation of the governing equations

Assuming that water is incompressible, the net outflow of water from the infinitesimal layer shown in Figure 5.4 must equal the net volume loss due to deformation. If V is the volume of the layer at time t, we can write:

$$q_{out} - q_{in} = -\frac{\partial V}{\partial t} \tag{5.10}$$

By indicating the differential flux as dq and A as the area available for vertical flow:

$$dq = -A\frac{\partial u_z}{\partial t} \tag{5.11}$$

Therefore, since $\epsilon_z = -\dfrac{\partial u_z}{\partial z}$:

$$dq = A\frac{\partial \epsilon_z}{\partial t}dz \tag{5.12}$$

Taking the differential of Darcy's law and combining with the above equation we arrive at the expression of mass balance:

$$\frac{\partial k}{\partial z}\frac{\partial h}{\partial z} + k\frac{\partial^2 h}{\partial z^2} = -\frac{\partial \epsilon_z}{\partial t} \tag{5.13}$$

We assume that the material is linearly elastic with (constant) modulus E_0':

$$\sigma_z' = E_0'\epsilon_z \tag{5.14}$$

The constitutive expression, relating the stress rate to the strain rate, can be derived as:

$$\sigma_z' = \sigma_z'\left(\epsilon_z(z,t)\right) \tag{5.15}$$

$$\frac{\partial \sigma_z'}{\partial t} = \frac{d\sigma_z'}{d\epsilon_z}\frac{\partial \epsilon_z}{\partial t} = E_0'\frac{\partial \epsilon_z}{\partial t} \tag{5.16}$$

$$\frac{\partial \epsilon_z}{\partial t} = \frac{1}{E_0'}\frac{\partial \sigma_z'}{\partial t} \tag{5.17}$$

The rate of change of the effective stress is:

$$\frac{\partial \sigma_z'}{\partial t} = \frac{\partial}{\partial t}\left(\sigma_z - p_h - p_e\right) = \frac{\partial}{\partial t}\left(\sigma_z - p_h - \gamma_w h\right) = \frac{\partial \sigma_z}{\partial t} - \frac{\partial p_h}{\partial t} - \gamma_w\frac{\partial h}{\partial t} \tag{5.18}$$

Taking into account that $\dfrac{\partial p_h}{\partial t} = 0$ and combining with Eq. 5.17, the constitutive expression becomes:

$$\frac{\partial \epsilon_z}{\partial t} = \frac{1}{E_0'}\left(\frac{\partial \sigma_z}{\partial t} - \gamma_w\frac{\partial h}{\partial t}\right) \tag{5.19}$$

Combining Eqs. 5.13 and 5.19 we obtain:

$$\frac{\partial k}{\partial z}\frac{\partial h}{\partial z} + k\frac{\partial^2 h}{\partial z^2} = -\frac{1}{E_0'}\left(\frac{\partial \sigma_z}{\partial t} - \gamma_w\frac{\partial h}{\partial t}\right) \tag{5.20}$$

Rearranging the terms we finally arrive at:

$$\frac{E_0'}{\gamma_w}\left(\frac{\partial k}{\partial z}\frac{\partial h}{\partial z}+k\frac{\partial^2 h}{\partial z^2}\right)+\frac{1}{\gamma_w}\frac{\partial \sigma_z}{\partial t}=\frac{\partial h}{\partial t} \tag{5.21}$$

Assuming that the depth of submersion (d_0) remains constant, i.e. that sea level does not rise, the increase in total vertical stress σ_v over time at any given location z can only be due to deposition of new material. Deposition causes a uniform increase of σ_v through the depth of the layer, which in turn implies a uniform increase of the total stress normal to the slope (σ_z):

$$\frac{\partial \sigma_z}{\partial t}=\cos^2\theta\frac{d\sigma_v}{dt} \tag{5.22}$$

where the normal force increment is obtained as $dF_z = 2l\cos\theta d\sigma_v$ and then $d\sigma_z = dF_z\cos\theta/(2l)$.

Substituting the above into Eq. 5.21 yields the governing equation of the problem:

$$\frac{E_0'}{\gamma_w}\left(\frac{\partial k}{\partial z}\frac{\partial h}{\partial z}+k\frac{\partial^2 h}{\partial z^2}\right)+\frac{\cos^2\theta}{\gamma_w}\frac{d\sigma_v}{dt}=\frac{\partial h}{\partial t} \tag{5.23}$$

Eq. 5.23 is a non-linear diffusion-generation equation for the excess head $h(z,t)$, which is the only unknown. For given values of the constant parameters γ, γ_w, θ, k and E_0', and for a known loading rate $\sigma_v(t)$, it can in principle be solved (with appropriate boundary conditions) for $h(z,t)$.

One complication is that, due to deposition, the thickness of the layer and therefore the location D of the top boundary, changes over time, i.e. $D = D(t)$. An additional equation to describe the velocity of this moving boundary is needed. The net upward movement of the boundary will be equal to the rate of deposition minus the rate of settlement due to consolidation:

$$\frac{dD}{dt}=\frac{1}{\gamma_s}\frac{d\sigma_v}{dt}+\left.\frac{\partial u_z}{\partial t}\right|_D \tag{5.24}$$

where u_z is considered positive along the positive z-axis, i.e. for swelling rather than settlement. Swelling requires (downwards) flow into the soil of a fluid volume equal to that swept by the moving boundary. Considering an arbitrary area A on the slope surface, and using Eq. 5.12:

$$\left.\frac{\partial u_z}{\partial t}\right|_D Adt=-dqdt=k\left.\frac{\partial h}{\partial z}\right|_D Adt \tag{5.25}$$

$$\left.\frac{\partial u_z}{\partial t}\right|_D=k\left.\frac{\partial h}{\partial z}\right|_D \tag{5.26}$$

Combining Eqs. 5.24 and 5.26 we finally arrive at the governing equation for the moving boundary:

$$\frac{dD}{dt} = \frac{1}{\gamma_s}\frac{d\sigma_v}{dt} + k\left.\frac{\partial h}{\partial z}\right|_D \tag{5.27}$$

If drainage is not allowed through the surface, the second term of the right hand side of Eq. 5.27 becomes zero and the surface moves upwards at the same rate that sediment is deposited. If, on the other hand, the rate of deposition is taken zero, Eq. 5.27 expresses the fact that the upwards (downwards) velocity of the moving boundary equals the downwards (upwards) superficial velocity of fluid flow through the surface.

To summarise, the problem at hand is an initial/boundary value problem expressed by Eqs. 5.23 and 5.27. The necessary initial and boundary conditions are:

- Initial thickness of soil layer: $D(t=0) = D_0$
- Initial excess pore pressure: $h(z, t=0) = 0$
- Impermeable bottom boundary: $\left.\frac{\partial h}{\partial z}\right|_{z=0,t} = 0$
- Free-draining top boundary (surface): $h(D(t), t) = 0$

5.2.1.3 Deformation-induced permeability variations

In our formulation, we assume that the kinematic permeability (k) is a function of the pore space volume, according to an exponential empirical relationship (Binh et al., 2009; Urlaub, 2012)

$$k = \frac{\gamma_w}{\mu_w} A e^{Bn} \tag{5.28}$$

where μ_w is the dynamic viscosity of water and A and B are a function of the sediment type. The starting permeability layering is attained by changing A and B over the sediment column, whereas transient changes in permeability are induced by variations in the pore space volume determined by the one-dimensional deformation, as a function of the effective stress and the linear elastic modulus (Eq. 5.18). For a one-dimensional problem, where the deformation is accommodated for by a change in pore-space, we can easily relate volumetric strain to the

increment in void ratio:

$$\dot{e} = \frac{1}{V_s}\frac{\partial V_v}{\partial t} = A\frac{\partial u_z}{\partial t}\frac{(e+1)}{Adz} = -\dot{\epsilon}_z(1+e) \tag{5.29}$$

Given the relationship between n and e, we have

$$\dot{n} = \frac{\partial n}{\partial e}\dot{e} = \frac{\partial}{\partial e}\frac{e}{(e+1)}\dot{e} = -\frac{\dot{\epsilon}_z}{(1+e)} \tag{5.30}$$

whereby porosity is updated at each iteration, and permeability is changed accordingly using Eq 5.28.

5.2.1.4 Factor of safety

In parts of the sediment column where the transfer of the overburden load from the pore fluid to the solid skeleton is inhibited, pore pressures higher than hydrostatic develop and the effective stress distribution deviates from the normal consolidation profile. As a result of the decreased effective stress, the shear stress necessary to trigger failure is reduced.

For an infinite slope (Morgenstern, 1967), the factor of safety (FOS) compactly expresses this concept. Once Eqs. 5.23 and 5.27 are solved for $h(z,t)$ and $D(t)$, the factor of safety $F(z,t)$ of the slope can be calculated over time and at different depths, as:

$$F(z,t) = \frac{\tan\phi'_{crit}}{\tan\phi'_{mob}(z,t)} \tag{5.31}$$

where ϕ'_{crit} the friction angle of the soil at critical state and $\phi'_{mob}(z,t)$ the mobilised friction angle at time t and depth z. Using Eqs. 5.2, 5.3 and the definition of effective stress from Eq. 5.7, we obtain:

$$\tan\phi'_{mob}(z) = \frac{\tau}{\sigma'_z} = \frac{\tau}{\sigma_z - p_h - \gamma_w h} \tag{5.32}$$

which, for a heterogeneous density model, can be expressed as:

$$\tan\phi'_{mob}(z_i) = \frac{-\int_D^{z_i}(\gamma(z)-\gamma_w)dz\sin\theta}{-\int_D^{z_i}(\gamma(z)-\gamma_w)dz\cos\theta - \gamma_w h} \tag{5.33}$$

After some algebraic manipulation, the previous equation becomes:

$$\frac{1}{\tan\phi'_{mob}(z_i)} = \frac{1}{\tan\theta}\left[1 - \frac{\gamma_w h}{-\int_D^{z_i}(\gamma_z - \gamma_w)dz\cos\theta}\right] \tag{5.34}$$

Finally, the factor of safety is expressed as:

$$F(z_i, t) = \frac{\tan\phi'_{crit}}{\tan\phi'_{mob}(z_i)} = F_0\left[1 - \frac{\gamma_w h}{-\int_D^{z_i}(\gamma_z - \gamma_w)dz\cos\theta}\right] \tag{5.35}$$

where

$$F_0 = \frac{\tan\phi'_{crit}}{\tan\theta} \tag{5.36}$$

is the factor of safety of the slope before loading commences. It is assumed $F_0 > 1$. Factors of safety below unity are obtained if the mobilised strength is higher than the available shear strength and correspond to failure of the infinite slope.

Infinite slope conditions, however, assume: (1) length much larger than the thickness of the failing soil mass; (2) slip plane parallel to the surface. In real cases, FOSs higher than one can observed at failure planes and, vice-versa, failure conditions predicted by the factor of safety can occasionally correspond to stable slopes (Viesca and Rice, 2012).

Therefore, in the following section, we will also focus on the development of overpressure and consequent effective stress reduction, as a more general physical parameter preconditioning a slope for failure, irrespective of whether failure conditions are predicted by the FOS.

5.2.2 Numerical treatment

The governing Eqs. 5.23 and 5.27 can be solved using a finite difference method (Bethke, 1985). Equations are discretised using a backward in time and centred in space finite difference scheme; i and j are used as indexes for the spatial and temporal grids, with steps ΔT and ΔZ (Fig. 5.5). We use an implicit scheme in time, which is unconditionally stable, and a central finite-difference approximation in space. The accuracy of this implementation is of second order, i.e. the error increases with ΔZ^2, as long as the grid spacing is uniform (Ferziger and Perić, 2002).

However, in our model, the latter condition can be violated and irregular grid spacings can play a role. Each grid point within the model undergoes vertical

displacement as a consequence of loading, and the accumulated vertical displacement is, in general, not negligible. Therefore, we replace the constant ΔZ, with a time and space varying spatial step:

$$\Delta Z_{i,j} = Z_i^{j-1} - Z_{i-1}^{j-1} + u_i^{j-1} - u_{i-1}^{j-1} \tag{5.37}$$

The latter is equivalent to deforming the spatial grid progressively over time. The assumption $u_i << \Delta Z_i$ would normally be sensible for stiffness modulus' values typical of rocks ($10^4 - 10^6 kPa$) (Mavko et al., 2009). However, this is not the case in soft sediments, where the Young's modulus is in the order of $E \simeq 10^3 kPa$ (L'Heureux et al., 2012; Vanneste et al., 2013) and significant deformations correspond to the reduction of the pore space.

One more complication is that the location of the top boundary changes over time, as prescribed by Eq. 5.27. At any given time T_j, the top boundary will, in the general case, be located between grid points Z_k and Z_{k+1} as shown in Figure 5.5, at a distance $\kappa\Delta Z$ from Z_k. With reference to Figure 5.5 we define the position of this temporary grid point through κ as:

$$\Delta^j = Z_k + \kappa\Delta Z \longrightarrow \kappa = \frac{1}{\Delta Z}\left(\Delta^j - Z_k\right) \tag{5.38}$$

The finite difference approximation of a n_{th} order derivative at grid point i can be derived using Taylor expansions of the excess head function at two grid points adjacent to i. Hereafter, we refer to the discretised parameters and unknown using the capitalised letters:

$$H_{i+1}^j = H_i^j + H_i'\Delta Z_{i+1;i} + \frac{1}{2}H_i''\Delta Z_{i+1;i}^2 + \frac{1}{3!}H_i'''\Delta Z_{i+1;i}^3 + O(\Delta Z^4) \tag{5.39}$$

$$H_{i-1}^j = H_i^j - H_i'\Delta Z_{i-1;i} + \frac{1}{2}H_i''\Delta Z_{i-1;i}^2 - \frac{1}{3!}H_i'''\Delta Z_{i-1;i}^3 + O(\Delta Z^4) \tag{5.40}$$

Subtracting Eq. 5.40 from 5.39, and taking $|\Delta Z_{i+1,i} - \Delta Z_{i-1,i}|$ to be negligible, we obtain the expression for the centred finite difference approximation of the first spatial derivative with an error of order ΔZ^2.

$$\left.\frac{\partial H}{\partial Z}\right|_{Z_i,T_j} = \frac{H_{i+1}^j - H_{i-1}^j}{\Delta Z_{i+1;i} + \Delta Z_{i-1;i}} \tag{5.41}$$

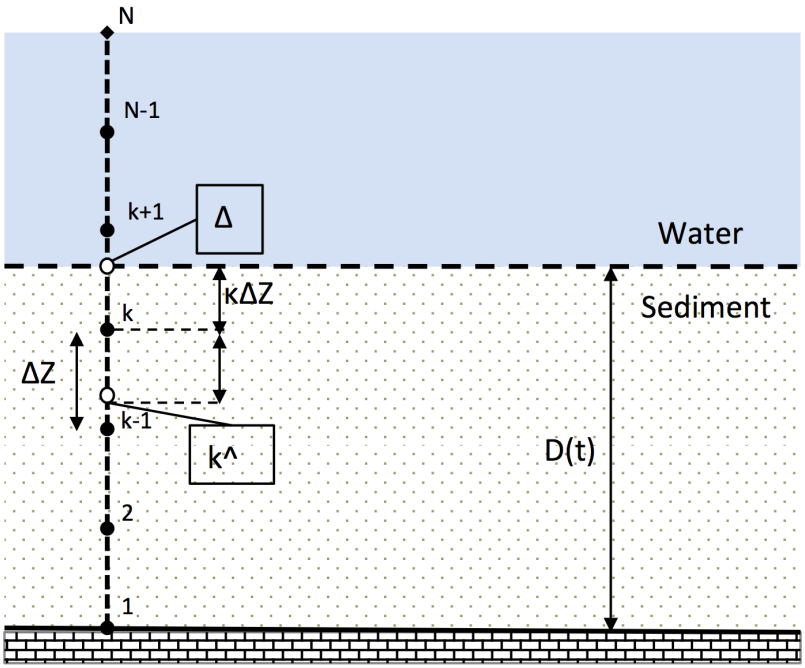

Figure 5.5: **Model discretisation**. Representation of the spatial finite difference grid with in-between grid points.

Adding Eq. 5.39 to 5.40 we obtain the expression for the second order derivative:

$$\left.\frac{\partial^2 H}{\partial Z^2}\right|_{Z_i,T_j} = 2\frac{H^j_{i+1} - 2H^j_i + H^j_{i-1}}{\Delta Z^2_{i+1;i} + \Delta Z^2_{i-1;i}} \tag{5.42}$$

If $|\Delta Z_{i+1,i} - \Delta Z_{i-1,i}|$ is significant, the approximation leading error would increase to first order.

At the moving sediment-water interface, $i = k$, the forward grid spacing is $\Delta Z_{\Delta,k} = \kappa \Delta Z_{k+1,k}$, whereas the backward distance is equal to $\Delta Z_{k-1,k}$. Such difference is a function of time and deposition rate and is in general not negligible (Fig. 5.5). To minimise losses of accuracy at the model top boundary, we consider two equidistant points centred around Z_k, with spacing $\kappa \Delta Z_{k-1,k}$: the node Δ, i.e. the interface, and the fictitious point $\hat{k}$. Using Eq. 5.38 we obtain the value at $Z_{\hat{k}}$ by linear interpolation (Fig. 5.5) :

$$H_{\hat{k}} = (1 - \kappa) H_k + \kappa H_{k-1} \tag{5.43}$$

$$H_{\Delta}^{j} = H_{k}^{j} + H_{k}'\kappa\Delta Z_{k-1;k} + \frac{1}{2}H_{k}''(\kappa\Delta Z_{k-1;k})^{2} + \frac{1}{3!}H_{k}'''(\kappa\Delta Z_{k-1;k})^{3} + O(\kappa^{4}\Delta Z_{k-1;k}^{4}) \tag{5.44}$$

$$H_{\hat{k}}^{j} = H_{k}^{j} - H_{k}'\kappa\Delta Z_{k-1;k} + \frac{1}{2}H_{k}''(\kappa\Delta Z_{k-1;k})^{2} - \frac{1}{3!}H_{k}'''(\kappa\Delta Z_{k-1;k})^{3} + O(\kappa^{4}\Delta Z_{k-1;k}^{4}) \tag{5.45}$$

Consistently, we can derive the first and second order finite difference approximations. Because, according to the free drainage boundary condition at the top $H_{\Delta} = 0$, we have:

$$\left.\frac{\partial H}{\partial Z}\right|_{k,T_j} = \frac{-H_{\hat{k}}^{j}}{\kappa\Delta Z_{k-1;k}} \tag{5.46}$$

$$\left.\frac{\partial^{2} H}{\partial Z^{2}}\right|_{k,T_j} = \frac{-2H_{k}^{j} + H_{\hat{k}}^{j}}{\kappa^{2}\Delta Z_{k-1;k}^{2}} \tag{5.47}$$

Finally, the backward finite differences time derivative reads:

$$\left.\frac{\partial H}{\partial T}\right|_{Z_i,T_j} = \frac{H_{i}^{j} - H_{i}^{j-1}}{\Delta T} \tag{5.48}$$

The final set of equations is obtained by discretising the diffusion and the moving boundary equations (Eqs. 5.23 and 5.24). Defining α_j as the current rate of change of vertical stress, for each time step T_j we solve:

- For gridpoint $i = 1$, using $H_{0}^{j} = H_{2}^{j}$ due to the boundary condition at $Z = 0$, the diffusion equation as:

$$\frac{E_{0}'}{\gamma_{w}}\left(+4K_{i}^{j}\frac{H_{2}^{j} - H_{1}^{j}}{\Delta Z_{2;1}^{2} + \Delta Z_{1;0}^{2}}\right) + \frac{\cos^{2}\theta}{\gamma_{w}}\alpha_{j} = \frac{H_{1}^{j} - H_{1}^{j-1}}{\Delta T} \tag{5.49}$$

- For gridpoints $2 \leq i \leq k-1$, the diffusion equation:

$$\frac{E'_0}{\gamma_w}\left(\frac{K^j_{i+1}-K^j_{i-1}}{\Delta Z_{i+1;i}+\Delta Z_{i;i-1}}\frac{H^j_{i+1}-H^j_{i-1}}{\Delta Z_{i+1;i}+\Delta Z_{i;i-1}}+2K^j_i\frac{H^j_{i+1}-2H^j_i+H^j_{i-1}}{\Delta Z^2_{i+1;i}+\Delta Z^2_{i;i-1}}\right)+ \tag{5.50}$$

$$\frac{\cos^2\theta}{\gamma_w}\alpha_j=\frac{H^j_i-H^{j-1}_i}{\Delta T}$$

- For gridpoint $i=k$ we account for the sediment-water interface boundary conditions; the first term of the space derivative of the Darcy's equation is dropped and the diffusion equation is modified using Eqs.. 5.46 and 5.47:

$$\frac{E'_0}{\gamma_w}\left(K^j_k\frac{-2H^j_k+H^j_{\hat{k}}}{\kappa^2\Delta Z^2_{k-1;k}}\right)+\frac{\cos^2\theta}{\gamma_w}\alpha_j=\frac{H^j_k-H^{j-1}_k}{\Delta T} \tag{5.51}$$

- For all time-steps, we work out the position of the sediment-water interface:

$$\frac{\Delta^j-\Delta^{j-1}}{\Delta T}=\frac{-H^j_{\hat{k}}}{2\kappa\Delta Z_{k-1;k}}+\frac{1}{\gamma_s}\alpha_j \tag{5.52}$$

- For all gridpoints with $Z_i>\Delta^j$, $H^j_i=0$.

At time T_j, we assume that Δ^{j-1} and all H^{j-1}_i are known from the solution of the previous time step $j-1$, or from the initial conditions if $j=1$. For all gridpoints K^j_i is updated accounting for the change in porosity at time T_{j-1} (Eq. 5.28).

5.3 Slope models

Here we simulate the deposition of soft, high-porosity sediment on synthetic infinite marine slopes, and model the transient excess pore pressure over time at shallow depths (≤ 50 m).

Each of the models considered represents a sedimentary structure similar to one of those commonly observed in areas prone to shallow landsliding. Lithological layering is represented by changes in the porosity-permeability relationship (as from section 5.2.1.3) within the model; these can be interpreted as variations in the sediment texture and pore-space connectivity, that are functions of

grain size, sorting and packing (Philips, 1991; Pape et al., 1999). For each layer, porosity at deposition is $\simeq 0.6 - 0.7$, and varies because of compaction over time. One dimensional stiffness is homogeneous and constant, representing soft, non-consolidated sediments ($E \simeq 10.0^3 kPa$; e.g.(Vanneste et al., 2013; Madhusudhan et al., 2017)).

Initial conditions are zero excess pore pressure within the sediment body, which, at a friction angle equal to 12° and slope angle of 3°, correspond to a factor of safety $FOS \simeq 4$. Therefore, the slopes are largely within stability conditions before sedimentation starts, and evolve closer to failure ($FOS \simeq 1$) through sedimentary loading.

Rather than an accurate representation of the natural processes occurring at specific geological settings, this work aims at generating reasonably complex overpressure profiles during deposition, within sedimentary structure that can be observed in nature, to test the sensitivity of seismic reflection data to effective stress reduction potentially conducive to slope failure. In some cases, in order to attain significant effective stress reduction via loading only, permeability values have been chosen to be close to the lower end of the realistic permeability spectrum (Neuzil, 1994; Binh et al., 2009) for marine sediments; in real cases, higher permeability values and milder permeability contrasts can in fact be observed at slope failure locations, where three-dimensional effects such as lateral fluid flow play a fundamental role in reducing the local effective stress (Dugan and Flemings, 2000). Likewise, failures observed in very low sedimentation rate environments ($< mm/year$; Urlaub et al., 2012; Urlaub, 2012), are not reproducible within our modelling assumptions.

In the next sections, the following display conventions are adopted:

- The geotechnical data are displayed as a function of depth below seafloor, whose position, in reality, changes due to deposition and settlement over time; however, to maintain consistency among the plots, hereafter changes in the sediment thickness are shown as changes in the position of the impermeable bedrock relative to a fixed seafloor.

- The curves of total stress are reduced to the value at the seafloor, where $u_h = \sigma_v$ and effective stress is zero; thereby in the plots the total, hydrostatic and effective stress will all be zero-valued at the sea-sediment interface.

- In the schematic lithological logs, permeable materials in the sedimentary columns are represented with light dotted patterns, whereas impermeable are indicated by a laminated design. The location of the likely glide plane is marked by a dotted red line.

- In the tables, background sedimentation will be indicated as B (*background sedimentation*); permeability anomalies potentially favouring the occurrence of localised stress reduction as A (referred to *event beds* in the text).

- The seismic data are displayed in two-way-traveltime (TWT) vs offset (i.e., distance between source and receiver). The colormap used is a conventional polar colour scheme, such that positive polarity reflections are red, zero-amplitude is white and negative reflections are blue.

5.3.1 Model-1. Delta-type

Table 5.1: **Model-1 layer properties at the moment of deposition**. A=event bed, potentially generating overpressure. B=background sediments.

Layer-type	Rate (mm/yr)	Perm.(m/s)	$\rho_g(g/cm^3)$	E (kPa)	Porosity
B	3	10^{-6}	2.65	10^3	0.7
A	30	10^{-9}	2.65	10^3	0.7
B	3	10^{-6}	2.65	10^3	0.7

The first scenario models the fast deposition of a hydraulically impervious layer within a high-permeability sedimentary column (Fig. 5.6, Tab. 5.1). The high permeability contrast, replicating a sand-clay transition, and the high sedimentation rate, have been observed in delta environments, such as the Ursa Basin in the Gulf of Mexico (Flemings et al., 2008; Long et al., 2008, 2011), associated with shallow seabed failure.

When deposition starts, a 1-m thick layer of permeable sediment ($k \simeq 10^{-6} m/s$) sits in equilibrium above the impermeable bedrock. A sediment of the same type is deposited at a rate of $3mm/yr$, until after about 800 years of deposition, whereupon a 1-m-thick low-permeability ($k \simeq 10^{-9} m/s$) layer is deposited at a fast rate ($30mm/yr$).

In Fig. 5.7, we show the permeability, overpressure ratio, porosity and FOS profiles at four instants during deposition. At the bottom of the impermeable bed, pore pressure dissipation is inhibited and overpressure builds up quickly, producing a locally almost-lithostatic pore pressure ($\lambda^* = 0.7$, Fig. 5.6), to which corresponds failure for the slope angle and friction angle of the simulation (Eq. 5.35). Failure occurs after 1.62 ka, when sediment thickness is 17 m. The localised disequilibrium compaction has a definite signature on the porosity profile, which markedly deviates from a normal consolidation curve (Fig. 5.7).

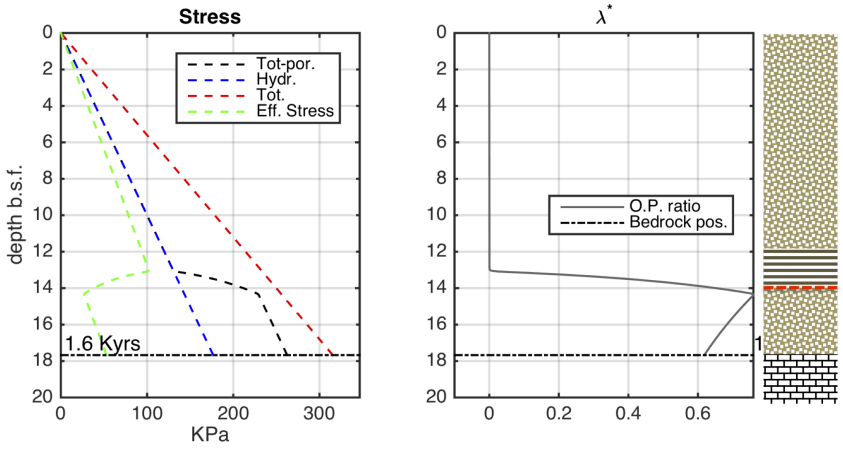

Figure 5.6: **Simulated stress conditions at failure for model-1**. On the left, total stress (red), hydrostatic pressure (blue), total pore pressure (black) and effective stress (green). On the right, sedimentary column: permeable sediments are represented by a light dotted pattern, low-permeability layer is indicated by a dark laminated interval; bedrock is represented by white blocks; the glide plane is marked by a dashed red line.

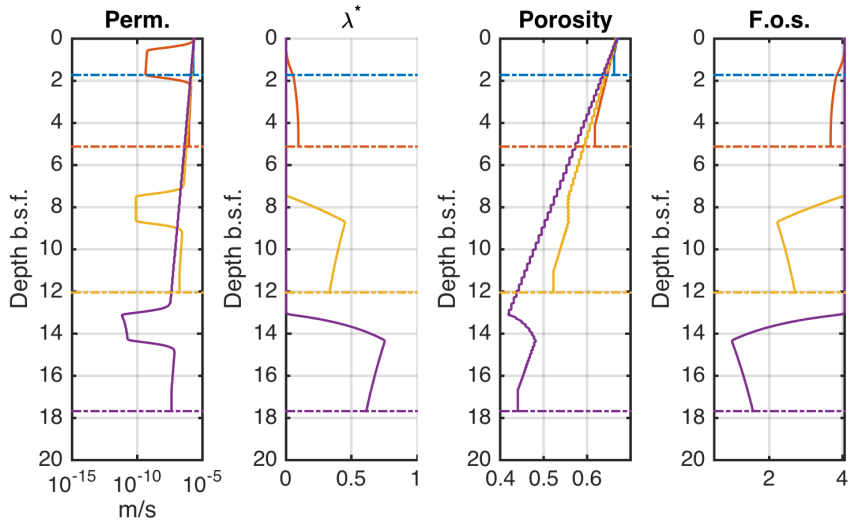

Figure 5.7: **Evolution of geotechnical properties for model-1**: 4 timesteps during deposition as a function of depth below the seafloor. In years, from the oldest to the most recent: blue-380, red-780, yellow-1180, purple-1620, after deposition starts; the relative bedrock position is shown as an horizontal dotted line with the same colour.

5.3.2 Model-2. Peri-glacial basin-type

Table 5.2: **Model-2 layer properties at the moment of deposition**. A=event bed, potentially generating overpressure (1 clay, 2 sand, 1 clay, for the A-bed has internal layering). B=background sediments.

Layer-type	Rate (mm/yr)	Perm.(m/s)	$\rho_g(g/cm^3)$	E (kPa)	Porosity
B	4	7.0^{-8}	2.65	10^3	0.7
$A1$	10	10^{-10}	2.65	10^3	0.7
$A2$	10	1.5^{-7}	2.65	10^3	0.7
$A1$	10	10^{-10}	2.65	10^3	0.7
B	4	7.0^{-8}	2.65	10^3	0.7

The second scenario simulates the deposition of a composite sub-metre thickness layer, with a thin sand seam within a clay bed, which interrupts a silty-clayey background sedimentation. This is based upon the stratigraphy observed in the peri-glacial environment of Finneidfjord, in northern Norway (Vardy et al., 2012;

Vanneste et al., 2013, 2015), and has also been seen in various other high latitude, previously glaciated settings (Hansen et al., 2011). Such structures are observed to produce overpressure, and to act as glide planes of shallow landslides (L'Heureux et al., 2012).

At the start of deposition, a 2-m-thick silty-clayey layer ($k \simeq 10^{-7} m/s$), is in place in equilibrium on the impermeable bedrock. A sediment of the same type is deposited for 400 years, followed by the quick ($\simeq 1 cm/yr$) emplacement of a 60-cm-thick composite layer. Its characteristics, described in Table 5.2, simulate a thinly layered sequence of the type clay-sand-clay (Fig. 5.8). The low permeability at the bottom of the first impermeable layer favours the localised increase of pore pressure, with λ^* quickly approaching 0.5 (Fig. 5.9). Failure occurs at $\simeq$ 1.0 ka after deposition starts, when λ^* exceeds 0.8, at a depth comparable to the one observed in the field in Finneidfjord (e.g. L'Heureux et al., 2012).

Note how the porosity profile, in Fig. 5.9, shows the effect of the property layering within the event bed: a sharp porosity increase at the bottom of the deepest impermeable unit, a decrease below the permeable sandy layer, and again a high-porosity anomaly determined by the impervious top clay bed.

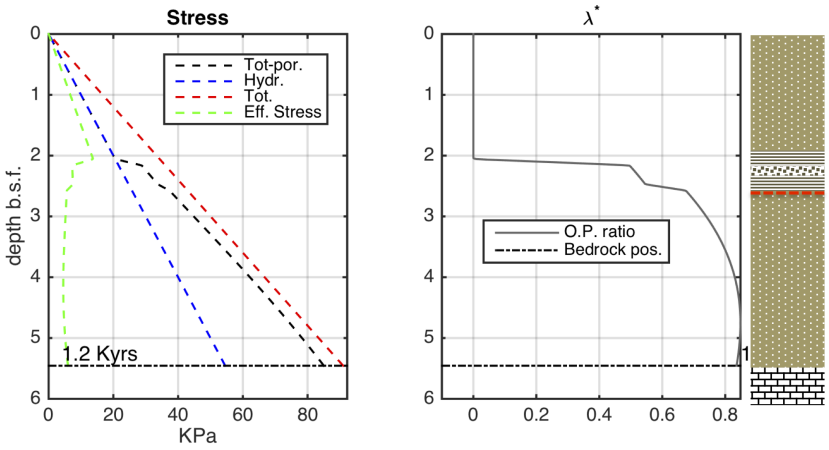

Figure 5.8: **Simulated stress conditions at failure for model-2**. On the left, total stress (red), hydrostatic pressure (blue), total pore pressure (black) and effective stress (green). On the right, sedimentary column: permeable sediment is represented with a light dotted pattern; low-permeability composite bed is indicated by a dark laminated interval with an interbedded clastic layer; bedrock is represented by white blocks; the glide plane is marked by a dashed red line.

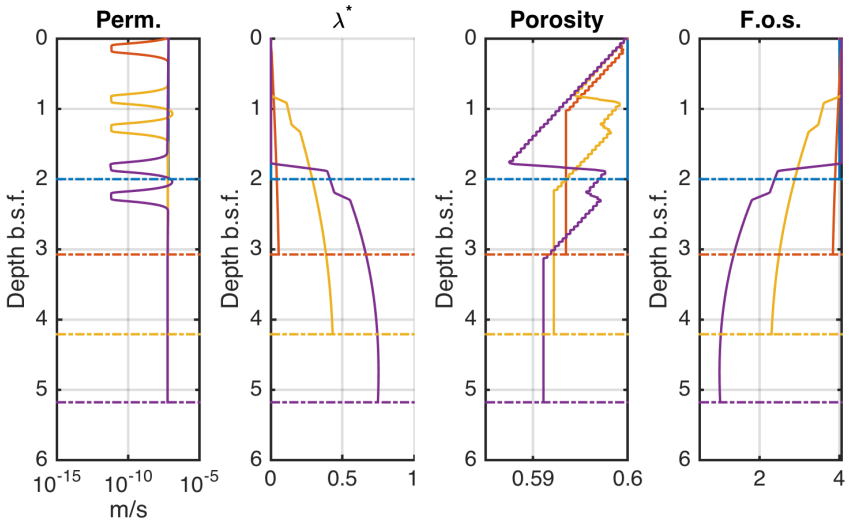

Figure 5.9: **Evolution of geotechnical properties for model-2**: 4 timesteps during deposition as a function of depth below the seafloor. In years, from the oldest to the most recent: blue-200, red-400, yellow-800, purple-1140, after deposition starts; the relative bedrock position is shown as an horizontal dotted line with the same colour.

5.3.3 Model-3. Continental shelf-type

Table 5.3: **Model-3 layer properties at at the moment of deposition**. A=event bed, potentially generating overpressure. B=background sediments.

Layer-type	Rate (mm/yr)	Perm.(m/s)	$\rho_g(g/cm^3)$	E (kPa)	Porosity
B	3	1.6^{-11} to 7.0^{-10}	2.65	10^3	0.6
A	3	1.6^{-11}	2.65	10^3	0.6
B	3	1.6^{-11} to 7.0^{-10}	2.65	10^3	0.6
A	3	1.6^{-11}	2.65	10^3	0.6
B	3	1.6^{-11} to 7.0^{-10}	2.65	10^3	0.6

The third and last scenario consists of the deposition of three coarsening upward, clayey-silty sedimentary sequence; compared to the two previous models, lower porosity and low overall permeability, associated with low sedimentation rates, simulate the deposition of more distal, fine-grained sediments. The changes in permeability at constant porosity as grain size varies, ought to be interpreted as

changes in the pore space structure, from a more interconnected one, to a more tortuous and impervious fluid path among the grains (Pape et al., 1999; Philips, 1991). The structure is loosely based upon core-logs from the continental-shelf AFEN complex (Madhusudhan et al., 2017). Each sequence's top boundary is marked by a sharp decrease in permeability, which produces a complex overpressure ratio profile.

Model characteristics are summarised in Table 5.3. Sediment thickness at t_0 is equal to 1 m, in equilibrium; the model simulates the cyclical deposition of a 10-m-thick coarsening upward sediment sequence, marked at the top by a minimum in permeability (Fig. 5.10). Due to the low sedimentation rate and the milder permeability contrast impeding upward fluid flow, overpressure builds up slowly, with maxima below the bottom of the most impermeable beds (Fig. 5.11); λ^* exceeds 0.5 after about 8.0 ka of deposition, and failure is attained at the bottom of the deepest impermeable layer (Fig. 5.10), after 1.2 ka.

Compared to the previous two examples, the porosity profile shows milder deviations from a normal consolidation profile, which are expected to produce less pronounced changes in the seismic response.

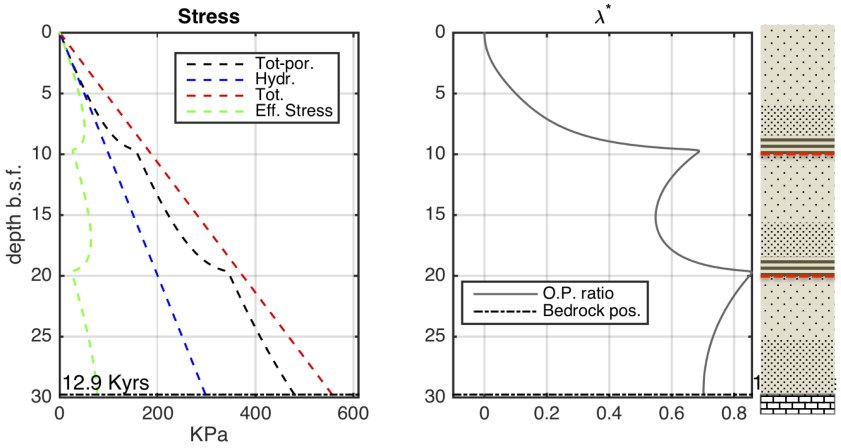

Figure 5.10: **Simulated stress conditions at failure for model-3**. On the left, total stress (red), hydrostatic pressure (blue), total pore pressure (black) and effective stress (green). On the right, sedimentary column: more permeable coarsening upward sequence is represented with a light dotted pattern, where the density of the dots is inversely proportional to the permeability; low-permeability bed is indicated by a dark laminated interval; bedrock is represented by white blocks; the glide plane is marked by a dashed red line.

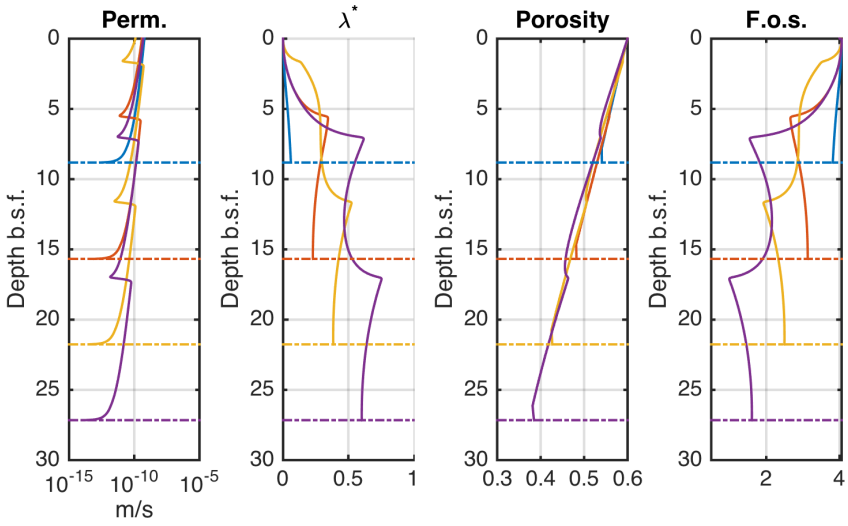

Figure 5.11: **Evolution of geotechnical properties for model-3**.:4 timesteps during deposition as a function of depth below the seafloor. In years, from the oldest to the most recent: blue-2880, red-5760, yellow-8640, purple-11520, after deposition starts; the relative bedrock position is shown as an horizontal dotted line with the same colour.

5.4 Synthetic time-lapse UHF seismic data

Multi-channel UHF seismic reflection data are simulated for each model, at time instants corresponding to relevant changes in overpressure. In order to propagate the wavefield in the slope, a new elastic parametrisation must be derived from the geotechnical properties.

In principle, rock-physics models relating the effective stress conditions to P-wave velocity (Mavko et al., 2009; Marin-Moreno et al., 2012, 2013), or site-specific relationships (Dugan and Sheahan, 2012), can be used to derive the parametrisation of the equivalent propagation medium (Mavko et al., 2009). However, the problem of an appropriate rock-physics model for the shallow sediments is beyond the scope of this work. Here we use a robust empirical relationship between P-wave impedance (Z) and porosity (n), as derived from extant in situ measurements of shallow sediment properties (e.g. Hamilton, 1970; Richardson

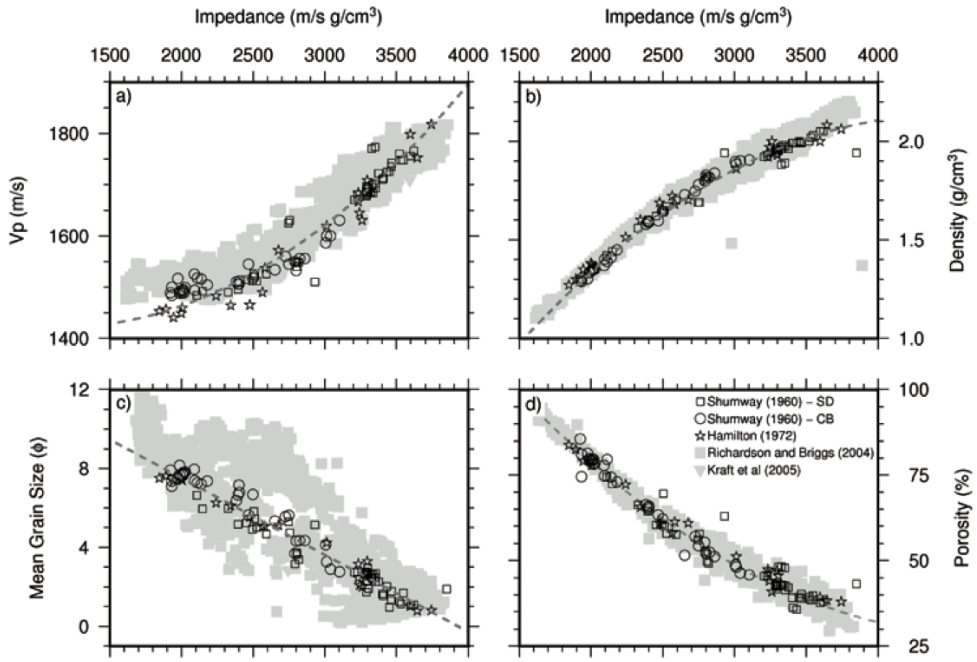

Figure 5.12: **Impedance-sediment properties relationships from Vardy (2015)**: the relationship plotted in panel d) between acoustic impedance and porosity is inverted and used to derive the acoustic model from the output of the slope modelling.

and Briggs, 1993) by Vardy (2015) (Fig. 5.12).

$$Z = \frac{6.307 \cdot 10^{-2} - [6.30710^2 \cdot 10^{-4} - 4 \cdot 6.604 \cdot 10^{-6} \cdot (178 + n \cdot 100)]^{0.5}}{(2 \cdot 6.60410^{-6})} \quad (5.53)$$

In water-saturated sediments, porosity is the parameter with the strongest footprint on P-wave propagation, because relative volumetric changes of pore-space and grain-skeleton modify the mechanical behaviour of the multi-phase body to a greater extent than variations in the nature of the solid grains (Mavko et al., 2009; Vardy et al., 2017).
Bulk density is directly derived from the slope model output parameters, as:

$$\rho = \frac{(\gamma_g * (1 - n) + \gamma_w \cdot n)}{g} \quad (5.54)$$

The model is assumed to be acoustic and isotropic. In the absence of pore-fluid substitutions and partial gas saturation (Ostrander, 1984; Provenzano et al.,

2016), this is a sensible first order approximation for limited-offset marine seismic data acquired on shallow sediments; in these settings, the observed Vp/Vs ratios are typically low, hence low sensitivities to possible overpressure-induced Poisson's ratio variations (Mallick and Dutta, 2002; Provenzano et al., 2017).

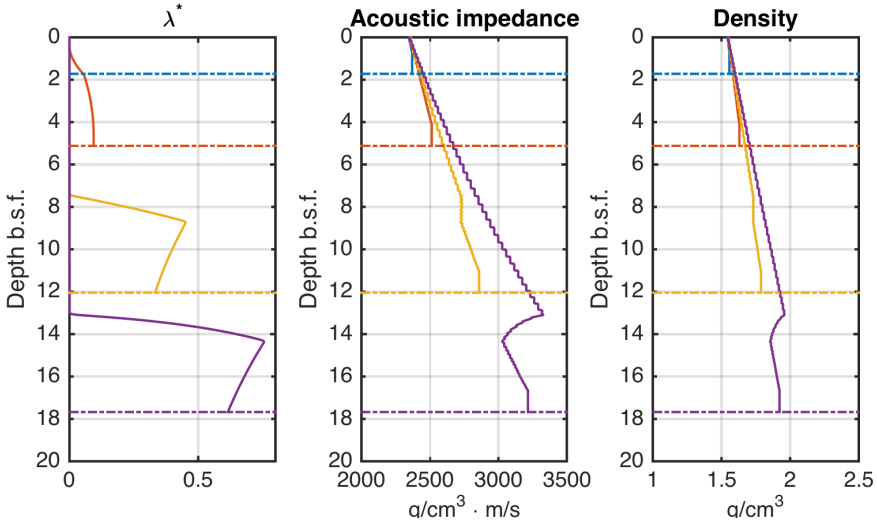

Figure 5.13: **Evolution of seismo-acoustic properties for model-1**: 4 timesteps during deposition as a function of depth below the seafloor. In years, from the oldest to the most recent: blue-380, red-780, yellow-1180, purple-1620, after deposition starts.

For each scenario and for each of the time instants represented in Figs. 5.7, 5.9 and 5.11, an acoustic subsurface model is derived and a multi-channel (MCS) synthetic seismic gather is computed using the method outlined in **Chapter 2**. Note in Figs 5.13 to 5.15 that the consolidation trend produces a positive acoustic impedance trend, and that localised excess pore pressure anomalies correspond to deviations of the acoustic impedance and density profiles.

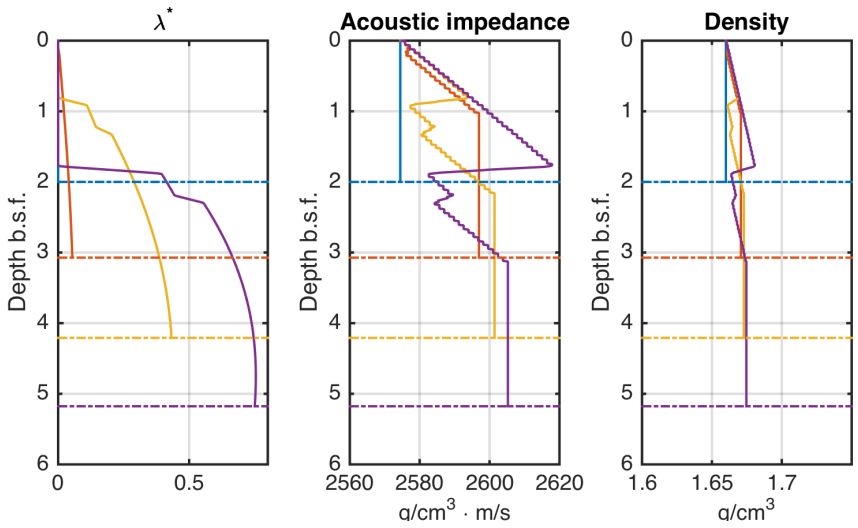

Figure 5.14: **Evolution of seismo-acoustic properties for model-2**: 4 timesteps during deposition as a function of depth below the seafloor. In years, from the oldest to the most recent: blue-200, red-400, yellow-800, purple-1140, after deposition starts.

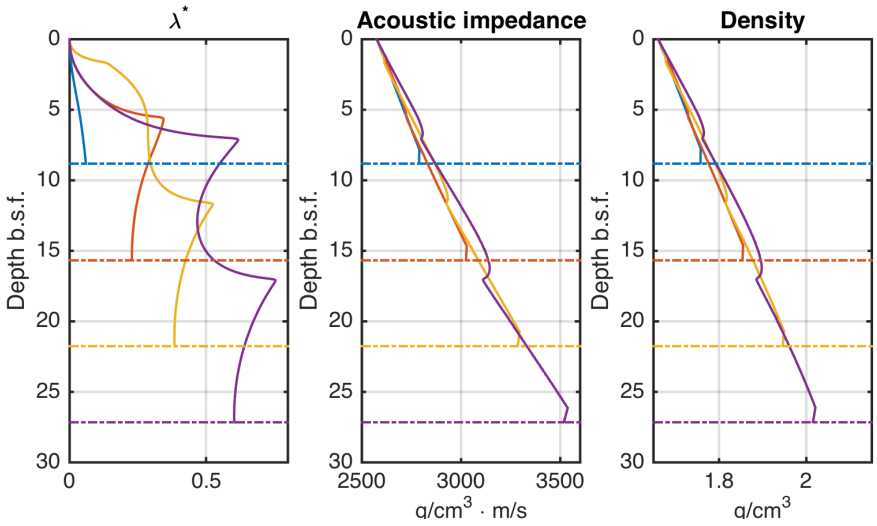

Figure 5.15: **Evolution of seismo-acoustic properties for model-3**: 4 timesteps during deposition as a function of depth below the seafloor. In years, from the oldest to the most recent: blue-2880, red-5760, yellow-8640, purple-11520, after deposition starts.

The simulation parameters and source signatures are comparable to the one used in **Chapter 3**, and replicate the characteristics of a 60-m long acquisition streamer (Pinson, 2009) combined with a Boomer source (Verbeek and McGee, 1995). The gentle slope angles and the parallel stratification, allow for the homogeneous layer method to be applied within a sensible one-dimensional approximation.

The seismic data from model-1 (Fig. 5.16), show the development of a strong negative polarity reflection as a consequence of disequilibrium compaction; pore pressure dissipation from below the impermeable layer is inhibited, porosity do not decrease, and a negative acoustic impedance anomaly is generated (Fig. 5.13). In Fig. 5.16, panels c and d correspond to λ^* respectively close-to and higher-than 0.5, before and at the moment of slope failure. Thus, in this case, a definite seismic signature is associated to the destabilisation of the slope.

In model-2 (Fig. 5.14), because of the lower sedimentation rate and the composite nature of the thin event bed, the localised shallow overpressure anomaly has lower magnitude and produces a weaker negative reflection (Fig. 5.17). The strongest porosity heterogeneity in the model, at the bottom of the shallowest sub-unit of the event bed, creates an acoustic interface with reflection coefficient close to 10^{-2}, with a clear signature in the seismic data developing in between 1.0 and 1.37 ka, when the slope fails.

In model-3, the less pronounced heterogeneities in the overpressure ratio and porosity profiles (Figs. 5.10 and 5.11), correspond to a less reflective time-evolving acoustic model (Fig. 5.15). Coincident with the deepest low-permeability bed, a dim negative reflection starts to be weakly visible at 40 ms TWT, after about 9 ka (Fig. 5.18). At failure, with $\lambda^* \simeq 0.8$, the reflected energy correlated to the event bed is higher, and stands out as a more coherent arrival, and a shallower (25 ms TWT), lower amplitude reflection is correlated to the top low permeability layer.

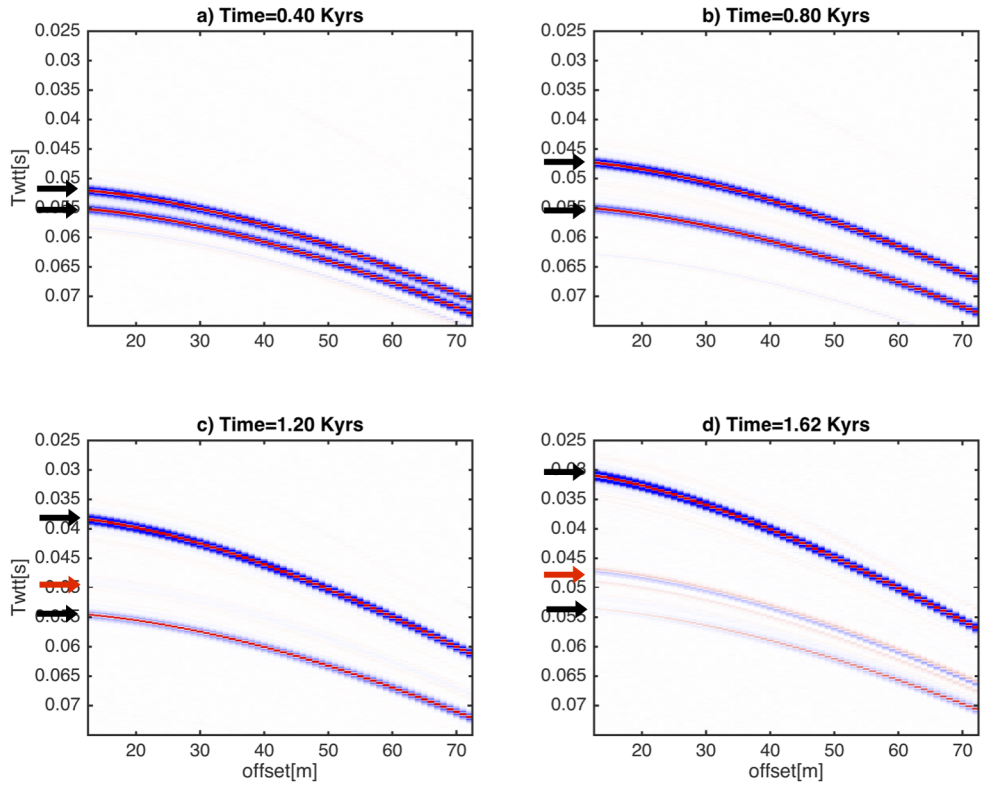

Figure 5.16: **Model-1 MCS seismic data**: Synthetic seismograms computed for the time-evolving acoustic models extracted from the consolidating slope. A blue-white-red colour scale is used so that negative reflections are blue and positive are red. The top and bottom black arrow indicate respectively the seafloor and the bedrock reflection; the red arrow points at the reflection generated by the overpressure development during deposition.

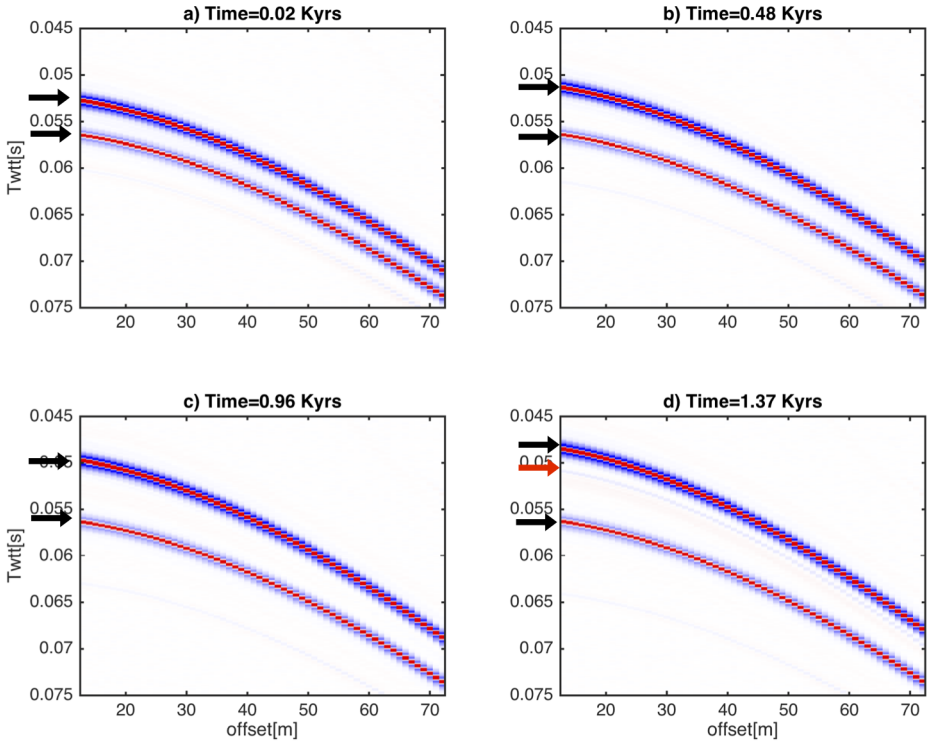

Figure 5.17: **Model-2 MCS seismic data**: Synthetic seismograms computed for the time-evolving acoustic models extracted from the consolidating slope. A blue-white-red colour scale is used so that negative reflections are blue and positive are red. The top and bottom black arrow indicate respectively the seafloor and the bedrock reflection; the red arrow points at the reflection generated by the overpressure development during deposition.

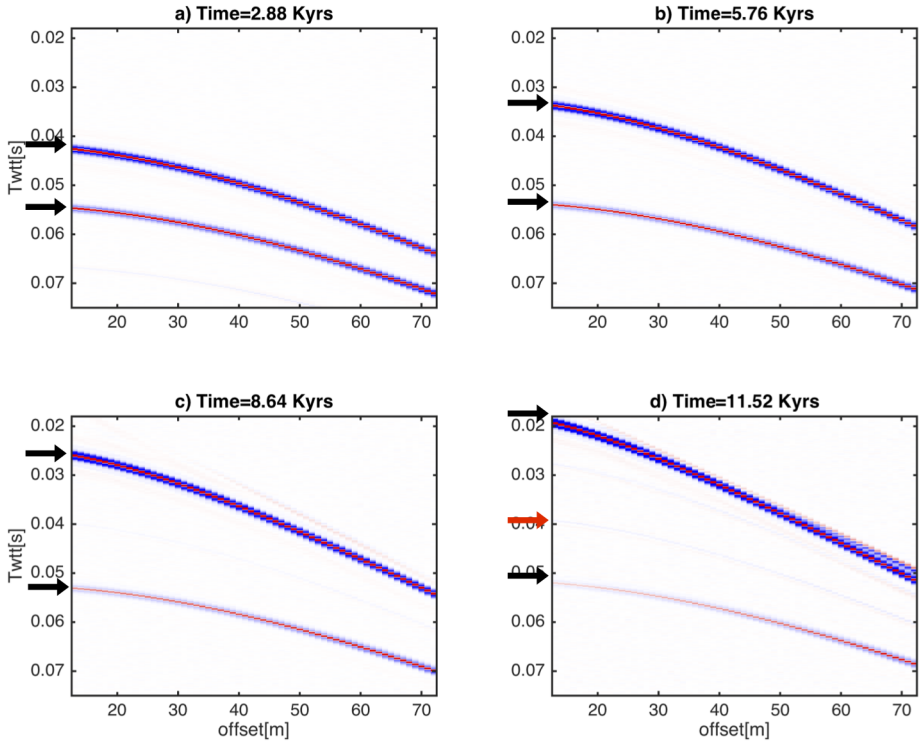

Figure 5.18: **Model-3 MCS seismic data**: Synthetic seismograms computed for the time-evolving acoustic models extracted from the consolidating slope. A blue-white-red colour scale is used so that negative reflections are blue and positive are red. The top and bottom black arrow indicate respectively the seafloor and the bedrock reflection; the red arrow points at the reflection generated by the overpressure development during deposition.

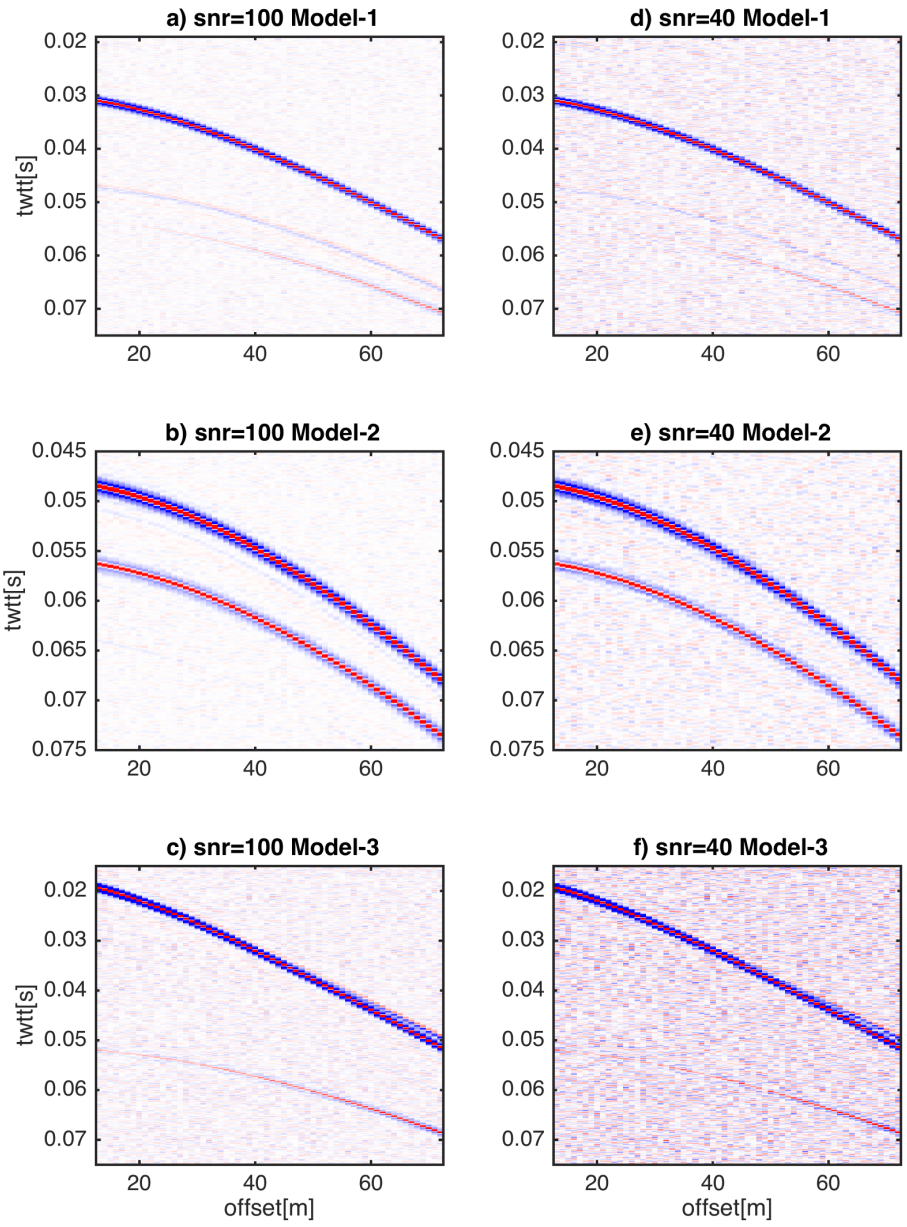

Figure 5.19: **Noise contamination**: Synthetic multi-channel data at failure, contaminated with random noise at different energy levels. In panels from a to c, signal-to-noise amplitude ratio (SNR) is equal to 100; in panels d to f, SNR is equal to 40.

5.4.1 Comments on the seismic data

The noise-free synthetic data have shown that negative polarity reflections are associated with the development of metric and sub-metric thickness pore pressure anomalies in the shallow subsurface. In order to asses the detectability of destabilising overpressure anomalies under more realistic noise conditions, we add random noise to the seismic data computed at failure, with the same frequency content of the signal (Fig. 5.19). For each model, signal-to-noise-ratios (SNR) equal to 100 and 40 are generated, where SNR has been computed as the ratio between the seafloor reflection and the root mean square noise amplitudes.

In model-1, a definite acoustic layering develops during deposition as a consequence of disequilibrium compaction (Figs. 5.7). A strong signature of this is present in the multi-channel seismic data, which remains clearly detectable in the SNR=40 dataset (panel d). Seismic inversion, as cast in the previous chapters, should therefore be capable of retrieving the acoustic anomaly from the data, under realistic noise-energy conditions (panels a and d in Fig. 5.19).

In model-2 (Fig. 5.9), the lower permeability contrast and the lower thickness of the event bed produce a weaker reflection. In Fig. 5.19, note that, though the event bed reflection has higher amplitude than the background noise in the SNR=100 dataset (panel b), it loses coherency at SNR=40 (panel e). The amplitude and depth of the reflection from the base of the event-bed are comparable to the ones observed in Finneidfjord, where both acoustic impedance (Vardy, 2015), and full waveform inversion have been successfully applied, in the latter case, despite strong coherent noise components in the data (see **Chapter 4** and Provenzano et al., 2016).

Model-3 (Fig. 5.11), shows the development of mild, cuspid-shaped acoustic anomalies corresponding to localised overpressure build-ups (Fig. 5.15). Although coincident with destabilising localised effective stress reductions, they produce reflection coefficients one order of magnitude lower than in model-2, arguably because the excess pore pressure profile contains smoother transitions (Fig. 5.15). The resulting seismic reflections have very low amplitude (Fig. 5.18), and are buried in noise in both cases (Fig. 5.19, panels c and f).

In order to answer the question whether, in these synthetic examples, time-lapse seismic data can be used for the early identification of excess pore pressure development, we extract the time evolution of the reflection coefficient (R_0) at the

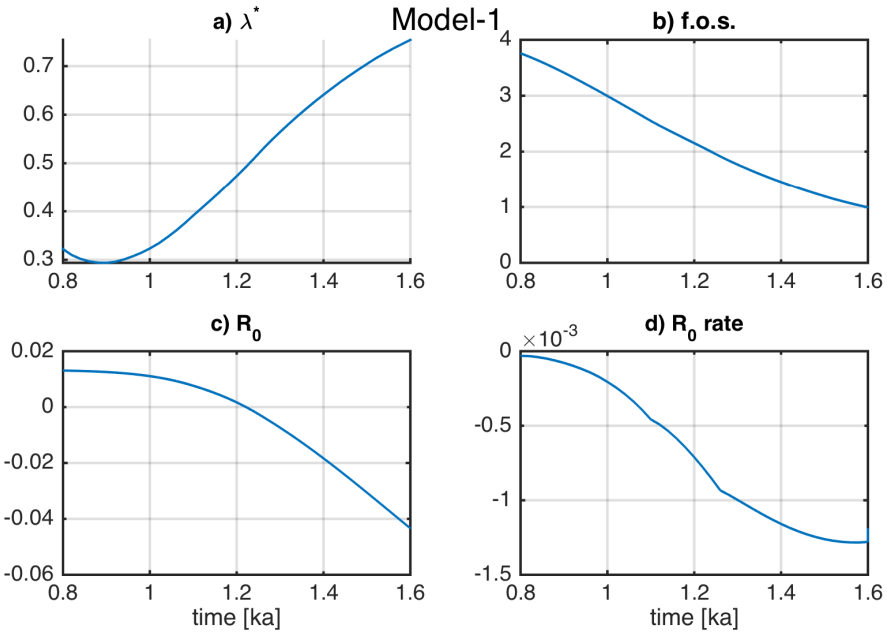

Figure 5.20: **Model-1 acoustic reflectivity evolution at the event bed**. Panel a: overpressure ratio. Panel b: factor of safety. Panel c: reflection coefficient. Panel d: reflection coefficient rate of change in 10 years.

strongest heterogeneity for each model (Fig. 5.20 to 5.22). The rate of change of R_0 in 10 years is also shown, and compared to the evolution of overpressure ratio (λ^*) and factor of safety. The destabilisation of the slope (decrease in factor of safety) does not show abrupt changes of gradient despite the non-stationary sedimentation rate; this correlates with a smooth evolution of the seismic response, which could potentially be detected by a time-lapse survey, provided that data with adequate signal-to-noise ratio are available.

These results indicate that the availability of data with low noise energy is crucial for detecting temporal changes in the shallow stress regime. When this is not the case, but multi-offset data is available, several methods, such as partial-angle stacking (Sheriff and Geldart, 1995) or waveform-preserving focusing techniques (Dagnino et al., 2017), can be applied to boost the signal-to-noise ratio before pre-stack inversion is applied. Should that not be sufficient, post-stack inversion, thanks the inherently lower noise energy (Sheriff and Geldart, 1995), could be a more appropriate means to identify small changes in acoustic impedance corresponding to slope destabilisation.

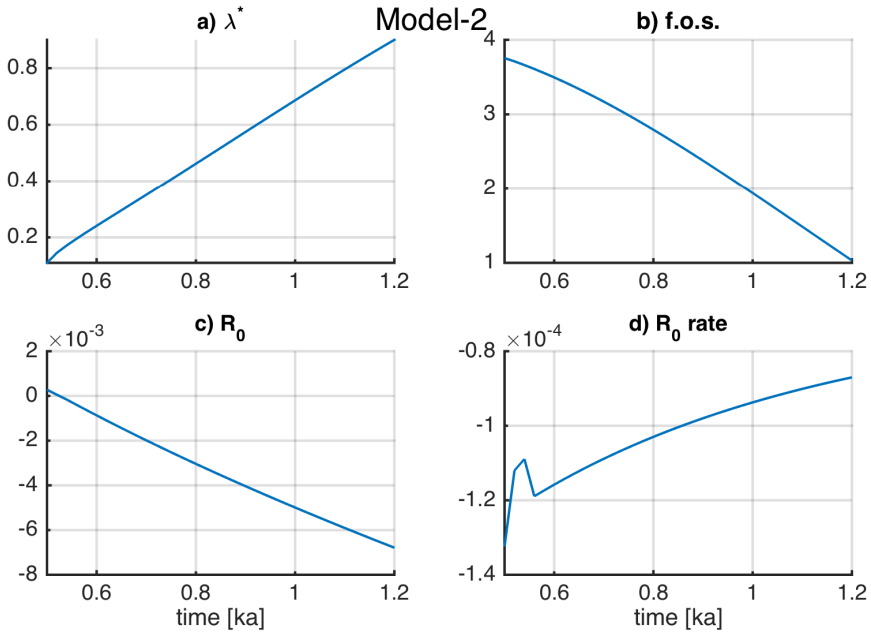

Figure 5.21: **Model-2 acoustic reflectivity evolution at the event bed**. Panel a: overpressure ratio. Panel b: factor of safety. Panel c: reflection coefficient. Panel d: reflection coefficient rate of change in 10 years.

When considering the suitability of seismic inversion for resolving potentially destabilising λ^* anomalies, it has to be recognised that seismic inversion provides a band-limited representation of the propagation medium: sub-decimetric scale variations of the effective stress conditions lie outside the bandwidth of most UHF data and are likely to produce no signature on the seismic data (Widess, 1973; Virieux and Operto, 2009); on the other hand, changes in the consolidation trend, can go undetected by limited offset data alone, where the moveout information is not enough to constrain the velocity macro-model (Jannane, 1989), and no a-priori information is available. Although inherent bandwidth and geometry limitations cannot be overcome, stochastic inversion methods and specific misfit functionals (e.g. **Chapter 4**), can be beneficial in these cases, for they are less liable to cycle-skipping than linearised inversions.

In this work, we have assumed that the reflectivity is only dependent upon disequilibrium compaction, and that model is acoustically transparent before consolidation starts. In fact, similar acoustic impedance contrasts can be observed at lithological or textural interfaces that have no relationship to changes

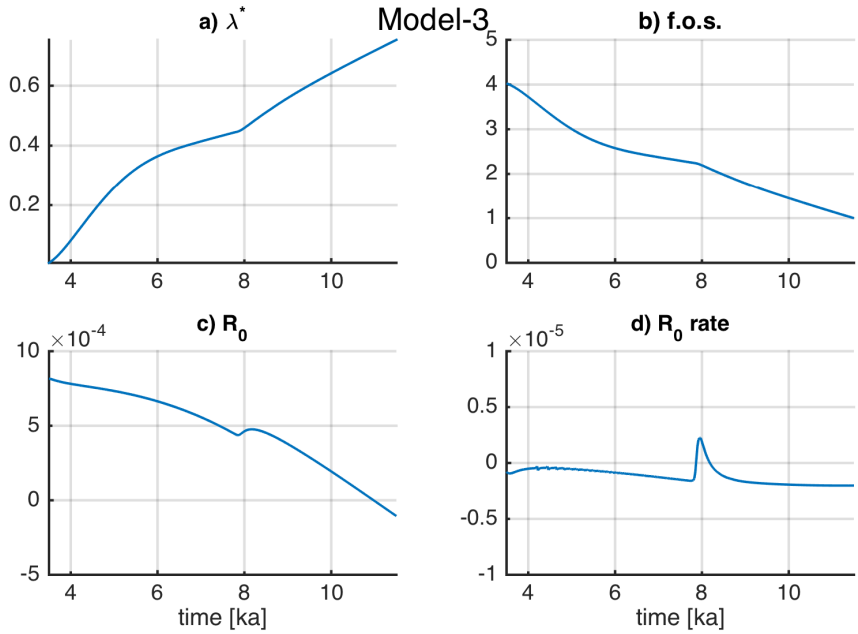

Figure 5.22: **Model-3 acoustic reflectivity evolution at the event bed**. Panel a: overpressure ratio. Panel b: factor of safety. Panel c: reflection coefficient. Panel d: reflection coefficient rate of change in 10 years.

in the effective stress conditions. However, specific techniques can be applied to multi-channel data, to distinguish overpressure-related seismic signatures from heterogeneities produced by other geological processes. For example: a time-lapse approach that looks for time-dependent changes in the acoustic properties, which can be attributed to fluid pore pressure variations from an initial state, in analogy with seismic exploration for reservoir monitoring (e.g., Asnaashari et al., 2015) of fluid injection studies (Zhang et al., 2014; Cevatoglu et al., 2015); integration of the inverted acoustic properties with burial modelling to assess the likely subsurface conditions (e.g. Marin-Moreno et al., 2012, 2013), supported by a-priori information about the underground geology from available sediment cores; a fully-elastic parametrisation of the seismic inverse problem can provide the additional information necessary (Igel et al., 1996; Provenzano et al., 2017) to distinguish the nature of the subsurface heterogeneities. Namely, as shown in **Chapter 3** and **Chapter 4** , independent estimates of Vp, density and Poisson's ratio enable to distinguish between lithological layerings, changes in partial gas saturation, and excess pore pressure.

5.5 Conclusions

In this chapter, I have modelled the deposition and consolidation of shallow submarine slopes with permeability heterogeneities and sedimentation rates realistic for a set of depositional environments where submarine landslides are observed. Localised disequilibrium compaction at specific low-permeability layers induces sub-metric thickness porosity anomalies, which relate to a time-evolving seismic response of the slope. A series of ultra-high-frequency multi-channel seismic datasets has been computed on the slope at different timesteps, with bandwidth and acquisition geometries comparable to realistic shallow marine surveys.

It has been shown that:

1. UHF multi-channel seismic reflection data are sensitive to the development of pore pressures higher than hydrostatic, as a consequence of compaction anomalies at low-permeability stratigraphic horizons.

2. The possibility to detect the development of overpressure is strongly dependent on the noise content of the data and on the nature of the under-compaction anomaly. This is, in turn, a function of sedimentation rate and permeability structure.

3. A time-lapse seismic reflection survey is potentially capable of identifying de-stabilising overpressure levels, but in some cases it would require appropriate pre-processing in order to obtain an adequate signal-to-noise ratio.

The characteristics of the seismic data are such that, within these limitations, pre-stack full waveform inversion, as cast in **Chapter 3** and **Chapter 4**, should be capable of capturing temporal evolutions in the acoustic model caused by evolving stress conditions. If accurate rock-physics relationships are available, the estimated seismic model can be used to quantify overpressure-related porosity anomalies. Overpressure ratio can then be inferred from porosity (Dugan and Flemings, 2000; Colombo et al., 2016), or equivalently from the model bulk density profile (Powrie, 2002), as shown in Vardy et al. (2015) and Vardy et al. (2017). Alternatively, a rock-physics constitutive model can be used to relate the estimated elastic moduli to the effective stress distribution (e.g. Marin-Moreno et al., 2012, 2013). Characterising temporal changes in the overpressure ratio of submarine slopes from seismic reflection data would have significant implications

on geohazard assessment. Potentially unstable (or evolving towards becoming unstable) areas could be identified before failure occurs, which would permit more focused detailed site investigation and the implementation of more effective hazard mitigation measures.

6

Conclusions and future work

Compared to hydrocarbon reservoir analysis, where seismic inversion and rock-physics modelling have a long history of being effectively combined to describe complex reservoirs, marine geohazard assessment and ground-model building for offshore engineering largely under-use seismic reflection data as a quantitative remote characterisation tool of the shallow geology. Recent advances in academia (e.g., Pinson et al., 2008; Vardy, 2015; Cevatoglu et al., 2015; Clare et al., 2017; Duarte et al., 2017; Monrigal et al., 2017) have shown that sediment properties can be remotely inferred from ultra-high-frequency seismic data, with decimetric to centimetric resolution, improving the knowledge of the near-seafloor in areas liable to shallow geohazards (e.g., submarine landslides, carbon capture and storage sites). Nevertheless, to date, seismic waveform inversion had not been applied to UHF seismic reflection data, at least in part because existing reservoir-scale pre-stack inversion procedures do not simply downscale to the sub-metric resolution required for geohazard applications.

6.1 Conclusions

In this thesis I have developed and applied custom-built methodologies for the inversion of shallow marine seismic data, in order to obtain a sub-metric resolution elastic model of the top 50 meters below the seafloor. In **Chapter 2**, I have shown that dedicated signal processing techniques in the plane-wave domain must integrate the one-dimensional solver in order to model efficiently UHF data. Specific conclusions from this chapter include:

1. Both the UHF sources and hydrophone receiver arrays are highly directional. This can be accounted for through the application of a frequency-wavenumber filter, in order to accurately represent the offset-dependent amplitude of the reflected waveform for each plane-wave component.

2. The streamer geometry in shallow marine seismic reflection surveys cannot be controlled, particularly in terms of depth, with the precision required for a generic pre-stack wavefield modelling approach. However, the receiver depths can be estimated from the frequency-offset receiver ghost notches, and the sea surface reflection coefficient variation inferred from the relative amplitude of receiver ghost and seafloor primary reflection for each channel. The retrieved parameters can then be used to model accurately the total wavefield: for each plane-wave component, the upgoing wavefield at constant depth obtained from the one-dimensional solver is down/up-propagated to the correct receiver depth; the downgoing part of the seismogram (receiver ghost) predicted in the frequency-wavenumber domain for each channel. Thereby a synthetic total seismogram is obtained that can be compared to the observed data.

In **Chapter 3** I have detailed the development of a deterministic waveform inversion methodology, custom-built for shallow marine UHF data, and demonstrated its efficiency on a complex synthetic example and a real case study. The main findings of this chapter are:

1. A multi-channel UHF marine seismic reflection dataset can be inverted to estimate the subsurface elastic model using a sequential deterministic approach, in which the parameters are inverted for from the strongest to

the weakest contributor to the reflectivity of the medium, namely: P-impedance; Poisson's ratio; and density. The results obtained from the inversion of a real UHF dataset can be compared with in-situ geotechnical measurements, within the seismic resolution.

2. The relative contribution of density and P-wave velocity to P-impedance can be decomposed, provided that reflection angles > 40 degrees are available, otherwise only P-impedance and Poisson's ratio can be independently resolved.

3. P-impedance is the most robust parameter to noise and can be effectively obtained from narrow reflection angle data even if P-wave velocity and density cannot be separated, as long as a reliable low-wavenumber velocity model is available.

4. The Poisson's ratio inversion does not require wide reflection angle data, but it suffers from an important loss of sensitivity in very high Vp/Vs ratio media, which can be partially compensated for using a structure-oriented gradient preconditioning.

In **Chapter 4**, I have addressed the problem of the robustness to inaccurate a-priori information, and demonstrated that:

1. A genetic algorithm as a stochastic optimiser is not inherently robust to inaccurate starting P-wave velocity trends.

2. A spectrally decoupled exploration of the model space, combined with a complex trace-based objective function, increases the robustness against inaccurate a-priori information derived from inaccurate reflection moveout analysis.

3. The obtained robust P-wave velocity model can be used to precondition the stochastic multi-parameter elastic inversion to reduce the size of the model space in high-dimensionality parametrisations. An accurate elastic model is obtained starting from poorly constrained a-priori information.

4. Stochastic seismic inversion can be used a remote characterisation tool for subsurface features preconditioning shallow geohazard. In a real case study, a weak layer that correlates to multiple landslides in the study area has been identified, and the inverted model shows an excellent agreement with the geotechnical ground-truth.

5. It is possible to identify changes in the pore-fluid saturation of a sub-metric thickness layer, including the signature of shallow partial gas saturation.

In **Chapter 5**, I have simulated the deposition and consolidation of heterogeneous sedimentary bodies on low-angle submarine slopes, in order to generate realistic complex overpressure profiles within the top 50 meters below the seafloor. Time-lapse synthetic seismic gathers are generated with frequency content and acquisition geometry comparable to the ones used in the previous chapters. The conclusions from this chapter can be summarised as follows:

1. UHF multi-channel seismic reflection data are sensitive to the development of pore pressures higher than hydrostatic, as a consequence of compaction anomalies at low-permeability stratigraphic horizons.

2. The possibility to detect the development of overpressure is dependent on the noise content of the data and on the nature of the under-compaction anomaly, which is in turn a function of sedimentation rate and permeability structure.

3. Within the sensitivity limitations of UHF data, a time-lapse seismic reflection survey is potentially capable of identifying de-stabilising overpressure levels. However, in order to detect transient changes of excess pore pressure, this requires high signal-to-noise ratios.

6.2 Future work

This work demonstrates that near-surface marine seismic reflection data can be quantitatively interpreted to retrieve the shallow sediments' elastic properties with a decimetric resolution. The set of information derived using the proposed methodologies is useful for a range of offshore engineering and geohazard applications. However, there is significant room for improvement in bridging the gap

between seismic inversion and marine geotechnics, and further work can be done to underpin the use of seismic data for offshore geohazard assessment. Possible future research includes, but is not limited to, the following:

1. Testing whether seismic inversion of multi-channel UHF reflection data can be effectively used to monitor changes in the subsurface pore-pressure conditions in the field, with a sensitivity useful to detect and recognise potentially destabilising overpressure levels.

2. Exploring the capabilities of rock-physics inversion methodology, whereby the seismic data are inverted directly for soil properties. This poses important problems from the point of view of numerical optimisation, because of the high number of unknowns and the strong coupling among different parameters. However, appropriate weighting and a-priori distributions can in principle be used to constrain the problem within the realm of realistic soil properties. If this were combined with a stochastic approach, we would be able to infer effective stress conditions from the seismic data, together with solutions error bounds, providing the engineering geologists with invaluable information for a fully-integrated framework.

A broader applicability of the proposed methodologies, would also benefit from future work aimed at optimising the extraction of useful information from the seismic data. Specifically, the following limitations of the inversion strategy have been identified, and should be addressed in future research:

1. Currently, the methodology lacks a general approach to the estimation of the source wavelet: source-independent approaches can be unstable and require accurate fine-tuning of spectral damping parameters; far field measurements of the source signature, on the other hand, are not always available. It is therefore worth to explore the performance of different source estimation techniques, as well as the possibility to include the source parameters among the unknowns of the inverse problem.

2. Seabed roughness at the wavelength or sub-wavelength scale, can produce a frequency- and angle- dependent scattering, modifying the signal as a function of the seafloor shape. For example, seafloor gravel waves (e.g., Pinson, 2009), can have wavelengths in the order of m, which would definitely have a footprint in the frequency band of UHF data.

3. Sea-surface multiple reflections are currently not modelled, thereby limiting the maximum penetration depth of the methodology. As recognised in hydrocarbon-scale seismic imaging (e.g., Berkhout and Verschur, 2006), appropriately accounting for sea-surface multiples in the inversion can be beneficial, provided that the sea-surface shape and reflection coefficient are known. Specifically, a dataset including surface-related multiple reflections could: (1) improve the reflection angle coverage at narrow angles, thereby improving the sensitivity to the AVO response in shallow water environments; (2) pose additional constraint on the long wavelength P-wave velocity model, thanks to the transmission-regime multiple seismic arrivals; (3) improve the depth-resolution in thinly layered subsurfaces (in two-way traveltimes, the multiple reflectivity series is stretched, therefore seismic reflections are better separated).

With the the aim to improve the applicability of the methodology to engineering design and geohazard assessment, further efforts should be made in order to contain its computing cost. In the current CPU parallel implementation, a single run of genetic algorithm-based multi-parameter inversion can use up to 24 hours computing time on a single node 16-core machine, depending on the bandwidth and the spatial parametrisation. Thanks to the highly parallel architecture, a GPU (*graphics processing unit*) implementation would allow for a significant reduction of the computing cost (up to one order of magnitude, e.g., P.Yang et al., 2015), significantly enhancing the possibility of application to large data volumes. GPUs are becoming an increasingly popular device for scientific computing, hence this could be a viable practical option to make the computing cost of FWI affordable for the offshore engineering community.

Bibliography

K. Aki and P.G. Richards. *Quantitative Seismology, 2nd edition*. University Science Books, 2002.

M. Aleardi and A. Mazzotti. 1D elastic full-waveform inversion and uncertainty estimation by means of a hybrid genetic algorithm-Gibbs sampler approach. *Geophysical Prospecting*, 65:64–85, 2017.

M. Aleardi, A. Tognarelli, and A. Mazzotti. Characterisation of shallow marine sediments using high-resolution velocity analysis and genetic-algorithm-driven 1d elastic full-waveform inversion. *Near Surface Geophysics*, 14:449–460, 2016.

A.L. Anderson and L.D. Hampton. Acoustics of gas-bearing sediments i. Background. *Journal of the Acoustical Society of America*, 67:1865–1889, 1980a.

A.L Anderson and L.D. Hampton. Acoustics of gas-bearing sediments ii. Measurements and models. *The journal of the acoustical society of America*, 67: 1890–1903, 1980b.

A. Asnaashari, R. Brossier, S. Garambois, F. Audebert, P. Thore, and J. Virieux. Regularized seismic full waveform inversion with prior model information. *Geophysics*, 78(2):25–36, March-April 2012.

A. Asnaashari, R. Brossier, S. Garambois, F. Audebert, P. Thore, and J. Virieux. Time-lapse seismic imaging using regularized full-waveform inversion with a prior model: which strategy? *Geophysical Prospecting*, 63:78–98, 2015.

C. Aster, B. Borchers, and C.H. Thurber. *Parameter estimation and inverse problems*. Elsevier Academic Press, 2005.

Katibe Aytun. The footsteps of the receiver ghost in the FK domain. *Geophysics*, 64(5):1618–1626, September-October 1999.

A.J. Berkhout and D.J. Verschur. Imaging of multiple reflections. *Geophysics*, 71:SI209–SI220, 2006.

C.M Bethke. A numerical model of compaction driven groundwater flow and heat transfer and its application to the paleohydrology of intracratonic sedimentary basins. *Journal of Geophysical Research*, 90:6817–6828, 1985.

N.T.T. Binh, T. Nakamura, K. Kozumi, M. Nakajima, M. Kubota, H. Kameya, and M. Taniue. Physical properties of the shallow sediments in late Pleistocene formations, Ursa Basin, Gulf of Mexico, and their implications for generation and preservation of shallow overpressures. *Marine and Petroleum Geology*, 26: 474–486, 2009.

Ebru Bozdag, J. Trampert, and J. Tromp. Misfit functions for full waveform inversion based on instantaneous phase and envelope measurements. *Geophysical journal international*, 185:845–870, 2011.

J.M Bull, R. Quinn, and J. Dix. Reflection coefficient calculation from marine high-resolution seismic reflection (chirp) data and application to an archelogical case study. *Marine Geophysical Researches*, 20:1–11, 1998.

C. Bunks, F. M. Saleck, S. Saleski, and G. Chavent. Multiscale seismic waveform inversion. *Geophysics*, 60:1457–1473, 1995a.

C. Bunks, F.M. Saleck, S. Zaleski, and G. Chavent. Multiscale seismic waveform inversion. *Geophysics*, 60:1457–1473, 1995b.

Richard L. Burden and J. Douglas Faires. *Numerical Analysis, 2.1 The Bisection Algorithm*. PWS Publishers, 1985.

K.J Campbell. Predicting offshore soil conditions. In *Offshore Technology Conference, Houston, TX OTC Paper 4692*, pages 391–398, 1984.

B.D. Carlton, K. Price, M. Vanneste, and C.F. Forsberg. Development and application of a regional slope stability assessment screening tool. In *IWLSC*, 2017.

M. Cevatoglu, J. Bull, M. Vardy, T.M Gernon, I.C Wright, and D. Long. Gas migration pathways, controlling mechanisms and changes in sediment acoustic properties observed in a controlled sub-seabed CO2 release experiment. *International Journal of Greenhouse Gas Control*, 38:26–43, 2015.

M. A. Clare, M. E. Vardy, M.J.B. Cartigny, P.J. Talling, M.D. Himsworth, J.K. Dix, J.M. Harris, and R.J.S. Whitehouse. Direct monitoring of active geohazards: emerging geophysical tools for deep-water assessments. *Near Surface Geophysics*, 15:427–444, 2017.

I. Colombo, G.M. Porta, P. Ruffo, and A. Guadagnini. Uncertainty quantification of overpressure buildup through inverse modeling of compaction processes in sedimentary basins. *Hydrogeol. J.*, 2016.

A. Contreras, C. Torres-Verdin, T. Fasnacht, W. Chesters, and K. Kvien. Joint stochastic inversion of 3d prestack seismic-amplitude data and well logs for high-resolution reservoir characterization and deepwater hydrocarbon reservoirs. *The Leading Edge*, 33(5):520–525, May 2014.

K.W. Conway, J.V. Barrie, and R. E. Thomson. Submarine slope failures and tsunami hazard in coastal British Columbia: Douglas Channel and Kiti Mat arm. Technical report, Geological Survey of Canada, October 2012.

D. Dagnino, V. Salláres, and C. R. Ranero. Scale and parameter-adaptive model-based gradient pre-conditioner for elastic full-waveform inversion. *Geophyscal journal international*, 198:1130–1142, 2014.

D. Dagnino, V. Salláres, and C. R. Ranero. Waveform-preserving processing flow of multichannel seismic reflection data for adjoint-state full-waveform inversion of ocean thermohaline structure. *IEEE Transactions on Geoscience and Remote Sensing*, 99:1–11, 2017.

W. Debski and A. Tarantola. Information on elastic parameters obtained from the amplitudes of reflected waves. *Geophysics*, 60:1426–1436, 1995.

A. Dey and L. R. Lines. Seismic source wavelet estimation and the random reflectivity assumption. Research report 10, 21-1–21-28., CREWES, 1998.

C.H. Dix. Seismic velocities from surface measurements. *Geophysics*, 20:68–86, 1955.

H. Duarte, N. Wardell, and O. Monrigal. Advanced processing for UHR3D shallow marine seismic surveys. *Near Surface Geophysics*, 15:347–358, 2017.

B. Dugan and P. Flemings. Overpressure and fluid flow in the new jersey continental slope: Implications for slope failure and cold seeps. *Science*, 289:288–290, 2000.

B. Dugan and T.C. Sheahan. Offshore sediment overpressure of passive margins: mechanism, measurements, and models. *Reviews of Geophysics*, 50, 2012.

J.L. Fatti, G.C. Smith, P.J. Vail, P.J. Strauss, and P.R. Levitt. Detection of gas sandstone reservoirs using AVO analysis: A 3D seismic case history using the Geostack techcnique. *Geophysics*, 59(9):1362–1376, 1994.

J.H. Ferziger and M. Perić. *Computational methods for fluid dynamics. 3rd edition.* Springer, 2002.

A. Fichtner, B. L. N. Kennet, H. Igel, and H. Bunge. Theoretical background for continental- and global-scale full-waveform inversion in the time-frequency domain. *Geophyscal journal international*, 175:665–685, 2008.

Andreas Fichtner. *Full Seismic Waveform Modelling and Inversion.* Springer, 2011.

P.B. Flemings, H. Long, B. Dugan, B. Germaine, J. John, C.M Behrmann, J.H. Sawyer, and IODP expedition 308 scientists. Pore pressure penetrometers document high overpressure near the seafloor where multiple submarine landslides have occurred on the continental slope, offshore Louisiana, Gulf of Mexico. *Earth and Planetary Science Letters*, 269:309–325, 2008.

C.F. Forsberg, T. Lunne, M. Vanneste, L. James, T. Tjelta, A. Barwise, and C. Duffy. Synthetic cpts from intelligent ground models based on the integration of geology, geotechnics and geophysics as a tool for conceptual foundation design and soil investigation planning. In *Offshore Site Investigation and Geotechnics Committee 8th International Conference*, September 2017.

K. Fuchs and G. Müller. Computation of synthetic seismograms with the reflectivity method and comparison with observations. *Geophysical Journal Research Astronomical Society*, 23:417–433, 1971.

S. Garzaglia, S. Migeon, E. Ducassou, L. Loncke, and J. Mascle. Mass transport deposits on the Rosetta Province (NW nile deep sea turbidite system, Egyptian margin): characteristics, distribution, and potentiall causal processes. *Marine Geology*, 250:180–198, 2005.

Y. Gholami, R. Brossier, S. Operto, V. Prieux, A. Ribodetti, and J. Virieux. Which parameterization is suitable for acoustic vertical transverse isotropic full waveform inversion? Part 2: Synthetic and real data case studies from Valhall. *Geophysics*, 78:107–124, 2013a.

Y. Gholami, R. Brossier, S. Operto, A. Ribodetti, and J. Virieux. Which parameterization is suitable for acoustic vertical transverse isotropic full waveform inversion? part 1: Sensitivity and trade-off analysis. *Geophysics*, 78:81–105, 2013b.

R.E. Gibson. The progress of consolidation in a clay layer increasing in thickness with time. *Journal of Geophysical Research*, pages 171–182, 1958.

D. Goldberg. *Genetic Algorithms in Search, Optimization, and Machine Learning.* Addison Wesley Publishing Company, Reading, MA., 1989.

D.S. Gordon and P.B. Flemings. Generation of overpressure and compaction driven fluid flow in a Plio-pleistocene growth-faulted basin, Eugene Island 330, offshore Lousiana. *Basin Research*, 10:177–196, 1998.

S.P.S. Gulick, G.L. Christeson, P.J. Barton, R.A.F. Grieve, J.V. Morgan, and J. Urrutia-Fucugauchi. Geophysical characterization of the Chicxulub impact crater. *Reviews of Geophysics*, 51:31–52, 2013.

H. Halflidason, R. Lien, H.P. Sejrup, H.P Forsberg, and P. Bryn. The dating and morphometry of the Storegga Slide. *Marine and Petroleum Geology*, 22: 123–136, 2005.

E.L. Hamilton. Sound velocity and related properties of marine sediments, North Pacific. *Journal of Geophysical Research*, 75:4423–446, 1970.

L. Hansen, J-S. L'Heureux, and O. Longva. Turbiditic, clay-rich event beds in fjord-marine deposits caused by landslides in emerging clay deposits – palaeoenvironmental interpretation and role for submarine mass-wasting. *Sedimentology*, 58:890–915, 2011.

C.W. Holland and J. Dettmer. In situ sediment dispersion estimates in the presence of discrete layers and gradient. *The journal of the acoustical society of America*, 133(1), January 2013.

J. Huang and V. Griffiths. One-dimensional consolidation theories for layered soil and coupled and uncoupled solutions by the finite-element method. *Geotechnique*, 60:709–713, 2010.

H. Igel, H. Djikpesse, and A. Tarantola. Waveform inversion of marine reflection seismograms for P-impedance and Poisson's ratio. *Geophyscal journal international*, 124:363–371, 1996.

M. Jannane. Short note. Wavelength of earth structures that can be resolved from seismic reflection data. *Geophysics*, 54(7):906–910, 1989.

C.E. Jimenez-Tejero, D. Dagnino, V. Salláres, and C.R. Ranero. Comparative study of objective functions to overcome noise and bandwidth limitations in full waveform inversion. *Geophyscal journal international*, 203:632–645, 2015.

S. Jin, R. Madariaga, J. Virieux, and G. Lambaré. Two-dimensional asymptotic iterative elastic inversion. *Geophysical journal international*, 108:575–588, 1992.

Y. Joo, S.J. Seol, and J. Byun. Acoustic full-waveform inversion of surface seismic data using the gauss-newton method with active constraint balancing. *Geophysical prospecting*, 61:166–182, 2012.

R. Kamei and R.G. Pratt. Inversion strategy for viscoacoustic waveform inversion. *Geophysical journal international*, 194:859–884, 2013.

J. Kennedy and R. Eberhart. Particle swarm optimization. *Proceedings of IEEE International Conference on Neural Networks*, 4:1942–1948, 1995.

O. Koefoed. On the effect of Poisson's ratio of rock strata on the reflection coefficient of plane waves. *Geophysical prospecting*, 3(4):381–387, 1955.

F. Kormendi and M. Dietrich. Nonlinear waveform inversion of plane-wave seismograms in stratified elastic media. *Geophysics*, 56(5):664–674, 1991.

T. Kwon, S.J. Seol, and J. Byun. Efficient full-waveform inversion with normalized plane-wave data. *Geophysical journal international*, 201:53–60, 2015.

P. Lailly. The seismic inverse problem as a sequence of before stack migrations. In J.B. Bednar, R. Redner, E. Robinson, and A. Weglein, editors, *Conference on Inverse Scattering: Theory and Application*, pages 206–220. Soc. Ind. Apl. Math., Philadelphia., 1983.

Gwang H. Lee, Bo Y. Yib, Dong G. Yoob, Byong J. Ryub, and Han J. Kimc. Estimation of the gas-hydrate resource volume in a small area of the Ulleung Basin, East Sea using seismic inversion and multi-attribute transform techniques. *Marine and Petroleum Geology*, 47:291–302, 2013.

K. H. Lee and H. J. Kim. Source-independent full waveform inversion of seismic data. *Geophysics*, 68:2010–2015, 2003.

D. Leynaud, N. Sultan, and J. Mienert. The role of sedimentation rate and permeability in the slope stability of the formerly glaciated Norwegian continental margin: the Storegga slide model. *Landslides*, 4:297–309, 2007.

Jean-Sebastien L'Heureux, Oddvar Longva, Alois Steiner, Louise Hansen, Mark E. Vardy, Maarten Vanneste, Haflidi Haflidason, Jo Brendryen, Tore J. Kvalstad, Carl Fredrik Forsberg, Shyam Chand, and Achim Kopf. Identification of weak layers and their role for the stability of slopes at Finneidfjord, northern Norway. *Submarine Mass Movements and Their Consequences. Advances in Natural and Technological Hazards Research*, 31:321–330, 2012.

R.O. Lindset. Synthetic sonic logs-a process for stratigraphic interpretation. *Geophysics*, 44(1):3–26, 1979.

H. Long, P. B. Flemings, J. T. Germaine, D. M. Saffer, and B. Dugan. Data report: Consolidation characteristics of sediments from IODP Expedition 308, Ursa Basin, Gulf of Mexico, in Gulf of Mexico Hydrogeology. *Proc. Integr. Ocean Drill. Program*, 308, 2008.

H. Long, P. B. Flemings, J. T. Germaine, and D. M. Saffer. Consolidation and overpressure near the seafloor in the Ursa basin, deepwater Gulf of Mexico. *Earth and Planetary Science Letters*, 305:11–20, 2011.

B.N. Madhusudhan, M.A. Clare, R.I. Clayton, and J.E. Hunt. Geotechnical profiling of deep-ocean sediments at the AFEN submarine slide complex. *Quarterly Journal of Engineering Geology and Hydrogeology*, 2017.

M. Malinkowski, S. Operto, and A. Ribodetti. High-resolution seismic attenuation imaging from wide-aperture onshore data by visco-acoustic frequency-domain full-waveform inversion. *Geophyscal journal international*, 186:1179–1204, 2011.

S. Mallick and S. Adhikari. Amplitude variation with offset and pre-stack waveform inversion: a direct comparison using a real data example from the Rock Springs Uplift, Wyoming, USA. *Geophysics*, 80(2):B45–B59, 2015.

S. Mallick and N.C. Dutta. Shallow water flow prediction using prestack waveform inversion of conventional 3D seismic data and rock modeling. *The Leading Edge*, 21:675–680, July 2002.

S. Mallick and L.N. Frazer. Practical aspects of reflectivity modeling. *Geophysics*, 52:1355–1364, 1987.

S. Mallick, X. Huang, J. Lauve, and R. Ahmad. Hybrid seismic inversion: A reconnaissance tool for deepwater exploration. *The Leading Edge*, pages 1230–1237, November 2000.

H. Marin-Moreno, T.A. Minshull, and R.A. Edwards. A disequilibrium compaction model constrained by seismic data and application to overpressure generation in the Eastern Black Sea Basin. *Basin Research*, 24(1-17), 2012.

H. Marin-Moreno, T.A. Minshull, and R.A. Edwards. Inverse modelling and seismic data constraints on overpressure generation by disequilibrium compaction and aquathermal pressuring: application to the Eastern Black Sea Basin. *Geophysical Journal International*, 2013.

D. G. Masson, C. B. Harbitz, R. B. Wynn, G. Pedersen, and F. Løvholt. Submarine landslides: processes, triggers and hazard prediction. *Phil. Trans. R. Soc. A*, 364:2009–2039, June 2006.

Gary Mavko, Tapan Mukerji, and Jack Dvorkin. *The rock physics handbook*. Cambridge U.P., 2009.

J. Mei, S. Ahmed, A. Searle, and C. Ting. Application of full waveform inversion on an Alaska land 3d survey. *SEG Denver 2014 Annual Meeting*, 2014.

William Menke. *Geophysical data analysis and inverse problems*. Academic Press INC., 1989.

O. Monrigal, I. De Jong, and H. Duarte. An ultra-high-resolution 3D marine seismic system for detailed site investigation. *Near Surface Geophysics*, 15: 335–345, 2017.

Peter Mora. Inversion = migration + tomography. *Geophysics*, 54(12):1575–1586, December 1980.

E. Morgan, M. Vanneste, and M. Vardy. Characterization of the slope-destabilizing effects of gas-charged sediment via seismic surveys. *Offshore Technology Conference-Houston*, 2014.

Jane Morgan, M. Warner, R. Bell, J. Ashley, D. Barnes, R. Little, K. Roele, and C. Jones. Next-generation seismic experiments: wide-angle, multi-azimuth, three-dimensional, full-waveform inversion. *Geophyscal journal international*, 195(3):1657–1678, 2013.

N.R. Morgenstern. *Submarine Slumping and the Initiation of Turbidity Currents*. University of Illinois press, 1967.

J.F. Nauroy, J.C. Dubois, J.L. Colliat, J.P. Kervadec, and J. Meunier. The GEOSIS Method for Integrating VHR Seismic and Geotechnical Data in Offshore Site Investigations. In *Offshore Site Investigation and Foundation Behaviour - New Frontiers: Proceedings of an International Conference*, pages 175–198, 1998.

C. Neuzil. How permeable are clays and shales. *Water Resources Research*, 30: 145–150, 1994.

J. Nocedal and S. J. Wright. *Numerical optimization*. Springer, 2006.

S. Operto, Y. Prieux, A. Ribodetti, R. Brossier, L. Metivier, and J.Virieux. A guided tour of multiparameter full waveform inversion with multicomponent data. *The Leading Edge*, pages 936–947, September 2013.

W.J. Ostrander. Plane-wave reflection coefficients for gas sands at non-normal angles of incidence. *Geophysics*, 49(10), 1984.

S. Panda, L. LeBlanc, and S. Schock. Sediment classification based on impedance and attenuation estimation. *The journal of the acoustical society of America*, 96:3022–3035, 1994.

H. Pape, C. Clauser, and J. Iffland. Permeability prediction based on fractal pore-space. *Geophysics*, 64:1447–1460, 1999.

O.M. Philips. *Flow and Reactions in Permeable Rocks*. Cambridge University Press, 1991.

L. Pinson. *Derivation of Acoustic and Physical Properties from High-Resolution Seismic Reflection Data*. Thesis for the degree of doctor of philosophy, School of Ocean and Earth Sciences, University of Southampton, November 2009.

L. Pinson, T. Henstock, J. Dix, and J. Bull. Estimating quality factor and mean grain size of sediment from high-resolution seismic data. *Geophysics*, 73:G19–G28, 2008.

W. Powrie. *Soil mechanics*. Spon, London, 2002.

R.G. Pratt, E. Plessix, and W.A. Mulder. Gauss-newton and full newton methods in frequency-space seismic waveform inversion. *Geophysical journal international*, 133:341–362, 1998.

J. Proakis and D. Manolakis. *Digital signal processing. Principles, algorithms and applications*. Pearson-Prentice Hall, 2006.

G. Provenzano, M. E. Vardy, and T.J. Henstock. Pre-stack waveform inversion of VHF marine seismic reflection data – A case study in Norway. In *Near Surface Geoscience 2016 – Second Applied Shallow Marine Geophysics Conference.*, 2016.

G. Provenzano, M.E. Vardy, and T. J. Henstock. Pre-stack full waveform inversion of ultra-high-frequency marine seismic reflection data. *Geophysical journal international*, 209:1593–1611, 2017.

P.Yang, J. Gao, and B. Wang. A graphics processing unit implementation of time-domain full-waveform inversion. *Geophysics*, 80:F31–F39, 2015.

M. Richardson and K. Briggs. On the use of acoustic impedance values to determine sediment properties. In *Acoustic classification and mapping of the seabed*, volume 15, 1993.

M. Riedel and F. Theilen. AVO investigations of shallow marine sediments. *Geophysical prospecting*, 49:198–212, 2001.

W. L. Rodi. A technique for improving the accuracy of finite element solutions for magnetotelluric data. *Geophysical Journal Research Astronomical Society*, 44:483–506, 1976.

D.H. Rothman. Nonlinear inversion, statistical mechanics, and residual statics esiimation. *Geophysics*, 50:2784–2796, 1985.

S.R. Ruthenford and R.H. Williams. Amplitude-versus-offset variations in gas sands. *Geophysics*, 54(6):680–688, 1989.

A. Sajeva, M. Aleardi, E. Stucchi, and A. Mazzotti. Estimation of acoustic macro models using a genetic full-waveform inversion: Applications to the Marmousi model. *Geophysics*, 81:173–184, 2016.

A. Sajeva, M. Aleardi, B. Galluzzi, E. Stucchi, E. Spadavecchia, and A. Mazzotti. Comparing the performances of four stochastic optimisation methods using analytic objective functions, 1D elastic full-waveform inversion, and residual static computation. *Geophysical Prospecting*, 65:322–346, 2017.

M. Sambridge. Geophysical inversion with a neighbourhood algorithm –ii. appraising the ensemble. *Geophyscal journal international*, 138:727–746, 1999.

M. Sambridge and K. Mosegaard. Monte carlo methods in geophysical inverse problems. *Reviews of Geophysics*, 40(3):1–29, 2002.

H. Schmidt and F.B. Jensen. A full wave solution for propagation in multilayered viscoelastic media with application to gaussian beam reflection at fluid-solid interfaces. *Journal of the Acoustic Society America*, 1985.

H. Schmidt and G. Tango. Efficient global matrix approach to the computation of synthetic seismograms. *Geophysical Journal Research Astronomical Society*, 1986.

S. Schock, L. LeBlanc, and L. Mayer. Chirp subbottom profiler for quantitative sediment analysis. *Geophysics*, 54:445–450, 1989.

M. Sen and P. Stoffa. Rapid sampling of model space using genetic algorithms. examples from seismic waveform inversion. *Geophyscal journal international*, 108:281–292, 1992.

M. Sen and P. Stoffa. Bayesian inference, Gibbs' sampler and uncertainty estimation in geophysical inversion. *Geophysical Prospecting*, 44:313–350, 1996.

M. Sen and P.L. Stoffa. *Global Optimization Methods in Geophysical Inversion*. Cambridge U.P., 2013.

G. Shanmugam. The landslide problem. *Journal of Palaeogeography*, 4:109–166, 2015.

P.M. Shearer. *Introduction to Seismology*. Cambridge U.P., 2009.

D. Sheen, K. Tuncay, C. Baag, and P. J. Ortoleva. Time domain Gauss-Newton seismic waveform inversion in elastic media. *Geophyscal journal international*, 167:1373–1384, 2006.

R. Sheriff and L. Geldart. *Exploration seismology*. Cambridge U.P., doi:10.1017/CBO9781139168359, 1995.

C. Shin, K. Yoon, K. J. Marfurt, K. Park, D. Yang, H. Y. Lim, S. Chung, and S. Shin. Efficient calculation of a partial-derivative wavefield using reciprocity for seismic imaging and inversion. *Geophysics*, 66:1856–1863, 2001.

A. Silverton, M. Warner, J. Morgan, and A. Umpleby. Offset-variable density improves acoustic full-waveform inversion: a shallow marine case study. *Geophysical prospecting*, pages 1–14, October 2015.

A. Skvortsov and B. Bornhold. Numerical simulation of the landslide-generated tsunami in Kitimat Arm, British Columbia, Canada, 27 April 1975. *Journal of Geophysical Research*, 112, 2007.

A. Steiner, J-S. L'Heureux, A. Kopf, M. Vanneste, O. Longva, and M. Lange. *Submarine Mass Movements and Their Consequences*, chapter An In-Situ Free-Fall Piezocone Penetrometer for Characterizing Soft and Sensitive Clays at Finneidfjord (Northern Norway). Springer, Dordrecht, 2012.

J. Stigall and B. Dugan. Overpressure and earthquake initiated slope failure in the Ursa region, northern Gulf of Mexico. *Journal of Geophysical Research*, 115, 2010.

P. Stoffa and M. Sen. Nonlinear multiparameter optimization using genetic algorithms: inversion of plane wave seismograms. *Geophysics*, 56:1794–1810, 1991.

M. Stoker, T. Bradwell, J. Howe, I. Wilkinson, and K. McIntyre. Lateglacial ice-cap dynamics in NW Scotland: evidence from the fjords of the Summer Isles region. *Quaternary Science Reviews*, 28:3161–3184, 2009.

D. Sun, K. Jiao, J. Cheng, and D. Vigh. Compensating for source and receiver ghost effects in full waveform inversion and reverse time migration for marine streamer data. *Geophyscal journal international*, 201:1507–1521, 2015.

M.T. Taner, F. Koehler, and R.E. Sheriff. Complex seismic trace analysis. *Geophysics*, 44:1041–1063, 1979.

A. Tarantola. Inversion of seismic reflection data in the acoustic approximation. *Geophysics*, 49(8):1259–1266, 1984.

A. Tarantola. A strategy for nonlinear inversion of seismic reflection data. *Geophysics*, 51(10):1893–1903, 1986.

A. Tarantola. *Inverse Problem Theory and Methods for Model Parameter Estimation*. Society for Industrial and Applied Mathematics, 2005.

Z. Tóth, V. Spiess, J. M. Mogollón, and J.B. Jensen. Estimanting the free gas content in Baltic Sea sediments using compressional wave velocity from marine seismic data. *Journal of Geophysical Research*, 119:1–17, 2014.

Z. Tóth, V. Spiess, and H. Keil. Frequency dependence in seismoacoustic imaging of shallow free gas due to gas bubble resonance. *Journal of Geophysical Research*, 120:8056–8072, 2015.

T.J. Ulrych. Application of homomorphic deconvolution to seismology. *Geophysics*, 36(4):650–660, August 1971.

M. Urlaub. *The role of sedimentation rate on the stability of low gradient submarine continental slopes*. PhD thesis, Ocean and Earth Sciences, Faculty of Natural and Enviromental Sciences, November 2012.

M. Urlaub, A. Zervos, P.J. Talling, D.G. Masson, and C.I. Clayton. *Submarine mass movements and their consequences-How Do 2° Slopes Fail in Areas of Slow Sedimentation? A Sensitivity Study on the Influence of Accumulation Rate and Permeability on Submarine Slope Stability*, volume 31 of *Advances in Natural and Technological Hazard Research*. Springer Netherlands, 2012.

M. Vanneste, J. L'Heureux, J. Brendryen, N. Baeten, J. Larberg, M. Vardy, A. Steiner, E. Morgan, E. Forsberg, C.F. Kvalstad, T.J. Chand, et al. Assessing offshore geohazards: a multidisciplinary reasearch intiative to understand shallow landslides and their dynamics in coastal and deepwater environments, Norway. *Advances in Natural and Technological Hazard Reseach*, 31:29–41, 2012.

M. Vanneste, O. Longva, J-S. L'Heureux, M. E. Vardy, E. Morgan, C.F. Forsber, T.J. Kvalstad, J.M. Strout, J. Brendryen, H. Haflidason, I. Lecomte, A. Steiner, Achim Kopf, T. Morz, and S. Kreiter. Finneidfjord, a field laboratory for integrated submarine slope stability assessments and characterization of landslide-prone sediments: A review. In *Offshore Technology Conference held in Houston, Texas, USA - OTC 13OTC-P-686-OTC*, 2013.

M. Vanneste, C.F. Forsberg, S. Knudsen, T.J. Kvalstad, J.S. L'Heureux, T. Lunne, M. E. Vardy, S. Chand, O. Longva, E. Morgan, A. Kopf, T. Morz, A. Steiner, J. Brendryen, and H. Haflidason. Integration of very-high-resolution seismic and CPTU data from a coastal area affected by shallow landsliding - the Finneidfjord natural laboratory. *International Symposium on Frontiers in Offshore Geotechnics*, 3, 2015.

M.E. Vardy. Deriving shallow-water sediment properties using post-stack acoustic impedance inversion. *Near Surface Geophysics*, 13:143–154, 2015.

M.E. Vardy, J-S. L'Heureux, M. Vanneste, O. Longva, A. Steiner, C.F. Forsber, and j. Brendryen. Multidisciplinary investigation of a shallow near-shore landslide, Finneidfjord, Norway. *Near Surface Geophysics*, 10:267–277, 2012.

M.E. Vardy, M. Vanneste, T. J. Henstock, E. Morgan, and L. Pinson. Can high-resolution marine geophysical data be inverted for soil properties? *Proceedings of the Institute of Acoustics*, 2015.

M.E. Vardy, M. Vanneste, T. J. Henstock, M. A. Clare, C.F. Forsberg, and G. Provenzano. State-of-the-art remote characterization of shallow marine sediments: the road to a fully integrated solution. *Near Surface Geophysics*, 15: 387–402, 2017.

N.H. Verbeek and T. M. McGee. Characteristics of high-resolution marine reflection profiling sources. *Journal of Applied Geophysics*, 33:251–269, 1995.

D.J. Verschur, A.J. Berkhout, and C.P. Wapenaar. Adaptive surface-related multiple elimination. *Geophysics*, 57:1166–1177, 1992.

R.C. Viesca and J.R. Rice. Nucleation of slip-weakening rupture instability in landslides by localized increase of pore pressure. *Journal of Geophysical Research*, 117, 2012.

J. Virieux and S. Operto. An overview of full-waveform inversion in exploration geophysics. *Geophysics*, 74(6), December 2009.

M. Warner and L. Guasch. Adaptive waveform inversion: theory. *SEG Denver 2014 Annual Meeting*, 2014.

M. B. Widess. How thin is a thin bed? *Geophysics*, 38:1176–1180, December 1973.

R.H. Wilkens and M.D. Richardson. The influence of gas bubbles on sediment acoustic properties: In situ, laboratory, and theoretical results from Eckernförde Bay, Baltic Sea. *Continental Shelf Research*, 18:1859–1892, 1998.

W.T. Wood, W.S. Holbrook, M.K. Sen, and P.L. Stoffa. Full waveform inversion of reflection seismic data for ocean temperature profile. *Geophysical Research letters*, 35, 2008.

Yu Xu, G. H. F. Gardner, and J. A. McDonald. Some effects of velocity variation on AVO and its interpretation. *Geophysics*, 58(9):1297–1300, 1993.

A. Zervos. One-dimensional consolidation of sediment continuously deposited on an infinite slope. Unpub., May 2014.

R. Zhang, M.K. Sen, and S. Srinivasan. Time-lapse pre-stack seismic inversion with thin bed resolution for CO2 sequestration from Cranfield, Mississipi. *International Journal of GreenHouse Gas control*, 20:223–229, 2014.